universität wien

MASTERARBEIT / MASTER'S THESIS

Titel der Masterarbeit / Title of the Master's Thesis

Dark portals at direct detection

verfasst von / submitted by

Leonie Einfalt BSc

angestrebter akademischer Grad / in partial fulfilment of the requirements for the degree of

Master of Science (MSc)

Wien, 2021 / Vienna, 2021

Studienkennzahl lt. Studienblatt / degree programme code as it appears on the student record sheet:	UA 066 876
Studienrichtung lt. Studienblatt / degree programme as it appears on the student record sheet:	Masterstudium Physik UG2002
Betreut von / Supervisor:	Ass.-Prof. Dr. Massimiliano Procura, Privatdoz.

Abstract

Despite intense effort in the experimental frontier, determining the nature of dark matter remains to be one of the unsolved problems in the 21st century. Among the ways to search for dark matter, an important avenue is given by direct detection experiments, where dark matter particles scatter off Standard Model particles in the targets of earth-bound detectors. The absence of a dark matter signal at current direct detection experiments, together with constraints from indirect detection and collider searches, has already excluded a non-trivial portion of the dark matter particle parameter space. Amongst other things, this calls for a reconsideration of the currently assumed dark matter-Standard Model particle interaction processes. In the context of direct detection, we explore scenarios where a dark matter particle interacts with Standard Model particles via two mediators. Both vector and scalar mediators, as well as mixtures thereof, are considered with one mediator being heavier than the other one in all cases. Adding a second mediator to the dark matter - Standard Model interaction leads to interference terms in the squared scattering amplitude. We show that this interference term leads to a rich phenomenology of the bi-portal model with mediator mass hierarchy and novel signatures in differential recoil spectra. Taking detector specific parameters like the energy resolution into the calculations, we argue, that detecting these signatures is at reach for current and proposed direct detection experiments. Using a profile likelihood ratio approach, we show a possible range of dark matter and mediator masses, as well as mediator couplings, where exclusion limits from bi-portal models differ significantly from single mediator models.

Zusammenfassung

Trotz intensivem experimentellem Aufwand bleibt die Identifizierung der Natur von Dunkler Materie eines der großen ungelösten Probleme des 21. Jahrhunderts. Eine der vielen Methoden zur Suche nach dunkler Materie stellen direkte Detektionsexperimente dar, in denen dunklen Materie Teilchen direkt mit Standardmodellteilchen im Detektormaterial interagieren. Das bisherige Ausbleiben eines Nachweises dunkler Materie in direkten Detektionsexperimenten, zusammen mit Einschränkungen aus indirekter Detektion und Teilchenbeschleunigern, schränkt den verfügbaren Parameterraum der dunklen Materie um einen nicht trivialen Teil ein. Diese Tatsache erfordert, unter anderem, ein Überdenken derzeit angenommener Wechselwirkungsprozesse zwischen Dunkler Materie und Teilchen des Standardmodells. In dieser Arbeit werden im Vordergrund der direkten Detektion Szenarien untersucht, in denen ein Dunklen Materie Teilchen über zwei Mediatoren mit Teilchen des Standardmodells interagiert. Die Interaktion via Vektor- und Skalar-teilchen, sowie Kombinationen dieser, werden analysiert, wobei in allen Modellen einem Mediator eine größere Masse zugewiesen wird als dem anderen. Wird der Wechselwirkung zwischen Dunkler Materie und ein zweiter Mediator hinzugefügt, so enthält die quadratischen Streuamplitude einen Interferenzterm. Es wird gezeigt, dass dieser Interferenzterm zu einer reichen Phänomenologie des „bi-portal“ Modells und neuartigen Signaturen in den Verteilungsspektren der Rückstoßenergie führt. Detektorspezifischer Parameter, wie die Energieauflösung, werden in den Berechnungen berücksichtigt und es wird so gezeigt, dass diese Signaturen für aktuelle und zukünftige direkte Detektionsexperimente nachweisbar sein sollten. Unter Verwendung eines Likelihood-Quotienten-Tests zeigen wir einen möglichen Bereich von Massen für Dunkle Materie und Mediatoren, sowie Kopplungskonstanten, für welche sich die Ausschlussgrenzen von „bi-portal“-Modellen erheblich von Modellen mit Interaktion über einen einzelnen Mediator unterscheiden.

Contents

Introduction **1**

1 A short introduction to dark matter **3**
1.1 Evidence for dark matter 4
1.2 Dark matter candidates 8
1.3 Detection of dark matter 10

2 DM-SM interaction **15**
2.1 Single portal models 16
2.1.1 From quarks to nucleons 19
2.1.2 From nucleons to nuclei 22
2.1.3 Non-relativistic kinematics and cross sections 24
2.1.4 Recoil spectra 26
2.2 Bi-portal models 31
2.2.1 Vector-Vector 31
2.2.2 Scalar-Vector 35

3 Analysis of the bi-portal model **39**
3.1 Constructive interference case 39
3.2 Destructive interference case 42
3.3 Total number of events 47
3.4 Impact of detector resolution 50

4 Statistics theory **53**
4.1 Statistical tests 53
4.1.1 Hypothesis testing 54
4.1.2 Test of significance 55
4.2 The method of maximum likelihood 57
4.2.1 Extended likelihood function 58

4.2.2 Binned likelihood . . . 59
4.3 Likelihood ratio as test statistics . . . 60
4.3.1 Discovery . . . 61
4.3.2 Exclusion . . . 62

5 Exclusion limits in the bi-portal model 65
5.1 Likelihood function . . . 66
5.2 Test statistic . . . 67
5.3 Exclusion limit planes . . . 68
5.3.1 m_χ-g_l exclusion limits . . . 68
5.3.2 $m_{Z_l'}$-g_l exclusion limits . . . 70
5.4 Results . . . 71

Conclusion and outlook 85

A Particle Physics 89
A.1 Recoil energy and minimum velocity . . . 89
A.2 NR Dirac spinors . . . 91
A.3 Conversion factor for the nuclear recoil rate . . . 93
A.4 Estimates for the couplings g from DM direct detection limits . . . 95

B Computational remarks 97
B.1 Generating mock data . . . 97
B.2 Detector resolution and low DM masses . . . 98
B.3 Minimization process . . . 99
B.4 Finding limits with bisection . . . 100

Bibliography 113

Acknowledgements 114

Introduction

The idea of dark matter (DM) has been around for almost a hundred years, and yet it represents one of the greatest unsolved puzzles in modern physics [1, 2]. Although various evidence for an additional matter component has been found in cosmology and astrophysics over the past few decades, there is still no direct proof of a possible particle nature [3–6]. In fact, the physical community does not even agree on what the missing mass consists of and there are numerous suggestion ranging from black holes to beyond Standard Model particles of mass as low as $1 \times 10^{-5}\,\mathrm{eV}$ [7, 8]. A widespread assumption is that a new particle constitutes the bulk of the missing matter, the so called WIMP (Weakly Interacting Massive Particle), and there is thus a large number of experiments having dedicated themselves to proving the existence of such a particle [9]. In the first chapter of this thesis an overview of evidence, candidates and searches for DM is given.

When considering a DM particle candidate, it is important to investigate the possible interactions between this new particle and the components of the well-established Standard Model (SM) of particle physics. The comprehension of such an interaction mechanism is especially important in the foreground of DM direct detection experiments, which aim at detecting the interaction of DM particles with target nuclei and electrons [9, 10]. The second chapter of this work is thus dedicated to the investigation of the DM-nucleus interaction. This is done by means of evaluating the relevant cross sections, as well as an expression for the differential recoil spectrum which is an important tool to relate interaction models to results from direct detection experiments. While in the first half of chapter 2 already established interactions via a single mediating particle are revisited, in the second half a new model is investigated where DM interacts with quarks in a nucleus via two mediators. DM models with two mediators have been previously considered, refer for example to [11–13], however, the novel feature of the model in this work is the hierarchy in the involved mediator masses. In chapter three the *bi-portal model* is then thoroughly analysed and compared to single mediator models, especially by means

of comparison between recoil spectra. Moreover, the impact of a detector's resolution is investigated, in order to determine if differences between single and bi-portal model are detectable in current and proposed DM direct detection experiments.

So far DM direct detection experiments have not yet published uncontroversial signal claims. Instead, exclusion limits on DM particle specific quantities are published in order to compare the results of different experiments [14, 15]. There are various approaches to generating such exclusion limits from measured and simulated data. Recently the method of profile likelihood ratios has gained in popularity and is now an integral part in the analysis procedure of various DM direct detection experiments, see for example [16–18]. The necessary statistical concepts needed in order to calculate limits with the profile likelihood approach are reviewed in the fourth chapter of this thesis. In chapter five exclusion limits in the bi-portal model generated with the profile likelihood ratio method from mock background samples are shown and discussed. The mock samples used in the analysis are based on the specifications of two different high resolution and low threshold experiments: the established CRESST-III experiment [16] and the COSINUS experiment [19], which is currently under construction.

To conclude we review the consequences that the introduction of an additional mediator may have on differential recoil spectra and exclusion limits from direct detection. Moreover, we give an outlook of possible continuation and extension of this work to related fields.

Chapter 1

A short introduction to dark matter

The notion dark matter ("dunkle Materie") first gained attention in the 1930s, primarily through the work of Swiss astronomer Fritz Zwicky[1] on the redshift and rotational velocity of the Coma cluster [2]. At first his idea of non-visible matter was met with a lot of scepticism, but the multitude of supporting works published in the following decades led to general acceptance of his theory in the scientific community. To this day, there is evidence for dark matter stemming from small astrophysical scales, like the rotational velocities of stars in galaxies, up to evidence on much larger cosmic scales like the cosmic microwave background. Non-baryonic dark matter, together with dark energy, is now also an integral part of the standard cosmological model and its contribution to the total matter density of the Universe is known to be about 83.9% [20]. There is thus five times more dark matter than baryonic matter, which makes up for the rest of the matter density in the Universe.

The following chapter gives a brief overview of the evidence and proposed candidates for DM, which are both as numerous as they are versatile. In the last section the three main approaches used in the search for a direct proof of the dominant mass component in the Universe are reviewed, with a focus on DM direct detection.

[1] Contrary to popular belief, Zwicky was not the first to explicitly use the term dark matter, but Henri Poincaré as early as 1906 [1].

1.1 Evidence for dark matter

As mentioned above, evidence for DM has been found both on astrophysical and cosmological scales [3]. This overview starts with the smallest scale evidence, namely the rotation curves of galaxies. An important advance to the field brought Vera Rubin and Kent Ford's work on the rotation of spiral galaxies, especially the Andromeda galaxy [4]. If a galaxy consists only of the visible dark matter which is concentrated in its center, one would assume that, with increasing distance to the center R, the circular velocities of stars in the galaxy fall off proportional to $\sim 1/\sqrt{R}$. However, the measurements of Rubin and her successors showed, that the rotational velocities stay almost constant at large distances. The measured circular velocities as a function of the distance to the galactic center for the spiral galaxy Messier 33 (M33) are displayed in Figure 1.1 [21]. The behaviour of the rotational curve can be explained by embedding the spiral galaxy in a DM halo of approximately spherical shape, which extends several orders beyond the radius of the visible galaxy [21]. Various models for the density profile of this halo have been established in order to explain the measured rotational curves. In particular, the density of DM at Earth's position in the Milky Way has been approximated, and

$$\rho_\chi = 0.3 \, \frac{\text{GeV}}{\text{cm}^3} \tag{1.1}$$

is a well-established value in DM searches [22, 23].

On a slightly larger scale, evidence for DM can also be found in the behaviour of galaxy clusters as observed by Zwicky for the Coma cluster [2]. There are two main methods to estimate the total gravitational mass in a cluster. The first is the Virial theorem, which allows to relate the kinetic energy of the cluster to the total potential energy of the gravitational field and thus the total mass. The kinetic energy can be determined from the velocities of the individual galaxies in the cluster. Another approach is to determine the mass of a cluster with gravitational lensing of background objects [24]. The achieved bound on the total mass of a cluster can then be compared to the estimated luminous mass from the total measured luminosity of the cluster. In general one finds a large discrepancy between luminous and total mass estimates which cannot be explained without a DM contribution.

Especially persuasive evidence for the existence of DM was found in the two galaxy clusters which together form the so-called *Bullet Cluster* [5]. The two clusters are known to have traversed each other at some point in the past. At the point of encounter the hot gas in the two cluster was caused to be left behind due to it

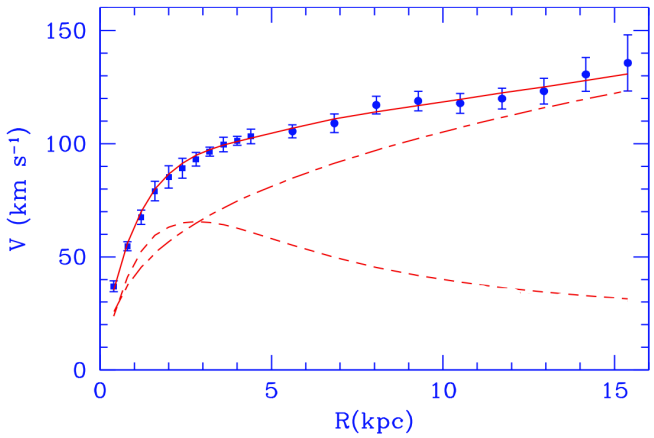

Figure 1.1: M33 rotation curve (blue points) together with the best fit model (continuous red line). The contribution from visible matter (stellar disk), which follows approximately $1/\sqrt{r}$, is shown as a short dashed line. The contribution from a possible DM halo is shown as a dashed dotted line. Plot taken from [21].

being affected by friction. The distribution of this hot gas, which is more massive than the visible matter, as seen through the emission of X-rays is displayed in the right image in Figure 1.2. However, an analysis of gravitational lensing effects in the optical picture showed, that the gravitational centers of the total mass of the clusters are displaced compared to the hot gas (green contour lines in Figure 1.2). This observation implies that there must be another dominant but invisible mass component present in the galaxy clusters. Moreover, once can infer that this additional mass component interacts only weakly with itself and the visible matter and was thus not as affected by the friction in the traversing process of the two clusters.

On a cosmological scale the Cosmic Microwave Background (CMB) offers evidence for DM and, as mentioned above, also a way to estimate the DM contribution to the total energy in the Universe. In the early Universe hydrogen was in thermal equilibrium and thus constantly produced and disintegrated:

$$p^+ + e^- \quad \longleftrightarrow \quad H + \gamma \tag{1.2}$$

In the relatively young universe ($\approx$ 380,000 years after the Big Bang), the expansion and cooling of the Universe caused the photons to decouple, as the horizon size became larger than the mean free path of the photons. From that point on, photons started to traverse the Universe freely - the Universe became transparent. The CMB, as observed today, is composed of photons produced in the last recombinations taking place at the time of decoupling, redshifted to microwave lengths. This

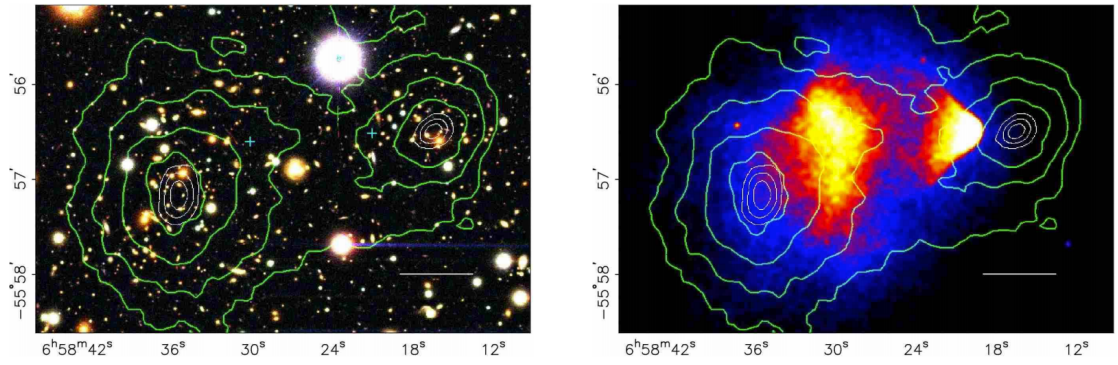

Figure 1.2: Two images of the Bullet Cluster 1E 0657−558. Left: an optical color image from the *Magellan telescope*, right: an image taken by the *Chandra X-ray Observatory* showing the distribution of the hot gas in the two traversing clusters. In both panels the green contour lines show the gravitational potential of the system as inferred from gravitational lensing of background objects. Plots taken from [5].

"echo" of the early Universe was first observed by A. Penzias and R.Wilson in 1964 [25]. The CMB represents one of the most perfect black body spectra with a temperature of $T = (2.7260 \pm 0.0013)\,\mathrm{K}$ [26]. However, the COBE satellite mission and its successors, WMAP and Planck, detected small fluctuations of order 10^{-5} in the temperature. The anisotropies in the CMB as seen in Figure 1.3, are a measure of the distribution of baryonic matter in the Universe at the time of photon decoupling. Baryonic matter was thus not perfectly homogeneous in the early Universe, although it was in equilibrium with radiation at that time. The random fluctuations in the baryonic matter density, despite equilibrium, suggest an additional non-baryonic matter component which was less affected by radiation, while still having a gravitational effect on baryonic matter. As mentioned above, the Planck results showed that non-baryonic matter is about five times as abundant as baryonic matter.

Independent of the CMB measurements, another estimate of the baryon density in the Universe can be obtained from the abundance of light elements in the Universe today. The bulk of light elements up to ^{7}Li were produced in the very early Universe in a process called Big Bang nucleosynthesis, while other heavier elements were later produced in stars. The production process begins with deuterium

$$p + n \quad \longrightarrow \quad d + \gamma \tag{1.3}$$

and trough addition of protons other light elements and their isotopes are created. This production only started to take place at a sufficient rate when the expansion of the Universe led to a suppression of the disruption of deuterium by high-energy

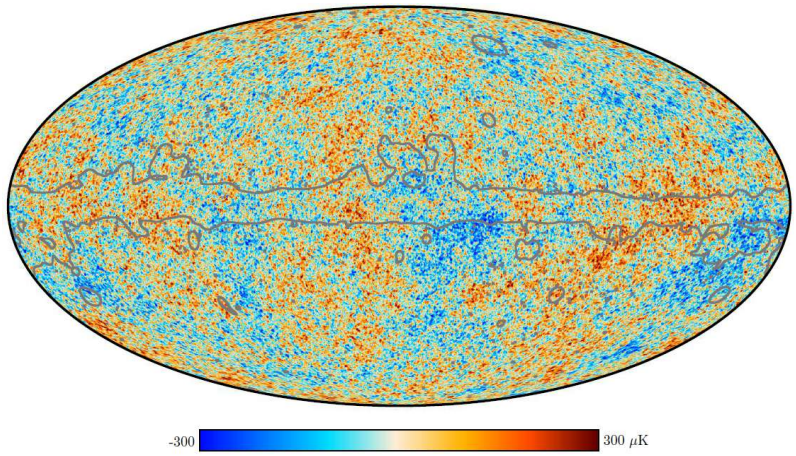

Figure 1.3: A map of the CMB, showing temperature fluctuations as measured by the Planck experiment and published in 2018 [27].

photons. The exact time when the deuterium production started, thus depends on the baryon to photon ratio. Due to the instability of neutrons, one can also determine the time at which deuterium production stopped, and the final abundances of light materials were almost fixed. The abundances of helium, deuterium and lithium nowadays can thus be calculated from the process of Big Bang nucleosynthesis. Comparison between the calculated abundances and measurements thereof, imply that the baryonic mass content in the Universe is indeed of the order predicted by the CMB [28].

To name a last example, evidence for the existence of DM can also be inferred from the large-scale structure of visible matter observed in the Universe today. Large-scale structures, such as superclusters and filaments, evolved out of very small density fluctuations in the Universe. The procedure of this structure evolution has been analysed with extensive computer simulations like the *Millennium Simulation* [29]. Comparison between the results of such simulations and observational data showed that large-scale structures of the Universe can only be achieved by introducing an additional mass component. This additional mass component was not as affected by radiation pressure in the early Universe and thus contributed to the clustering of ordinary matter. Moreover, a property of DM can be deduced from the outcome of such simulations. Only if the majority of matter was non-relativistic at the time of structure formation, smaller scale structures of the Universe could have been formed in the way they are observed today [6]. Due to the assumed low velocities and thus low energy, this paradigm is called cold dark matter (CDM).

1.2 Dark matter candidates

The proposed models to explain the missing mass in the Universe are just as numerous and versatile as the evidence for DM. The masses of candidates proposed range from $10^{-5}\,\mathrm{eV} \approx 9 \times 10^{-72}\,M_\odot$ for axions up to $10^4\,M_\odot$ for black holes. The heaviest candidates are summarized in the class Massive Compact Halo Objects (MACHOs) including brown dwarfs, rogue planets, neutron stars and black holes. These objects are, however, composed of baryonic Standard Model (SM) particles and can thus not explain the abundance of non-baryonic matter arising for example from CMB measurements. Moreover, there is evidence that the Universe does not contain enough MACHOs to account for the missing matter [30].

This section will thus focus on the various proposed ideas for particle DM. From the astrophysical and cosmological evidence described in the section above, some properties a potential particle DM candidate can be derived. First of all, the CMB shows that DM must have been present at the very early Universe and there is evidence that it is still abundant today, implying that the DM particle is rather stable. In addition, CMB measurements suggest that the DM is non-baryonic. While the DM has to interact gravitationally, other interaction with ordinary matter and itself must be very weak in order to explain the behaviour of the Bullet Cluster or why it has not yet been detected directly. The DM particle should thus be neutral under electric charge, as to not emit and/or absorb electromagnetic radiation. Moreover, it should also be neutrally charged under color in order to be unaffected by the strong interaction. As already mentioned above, the structure of the Universe suggests that the DM particle is non-relativistic.

We start the discussion of particle candidates, with the only SM particle which has been considered as DM - the neutrino. It seems rather suitable, as it is both neutral under electric and color charge, as well as non-baryonic. However, the neutrino is a relativistic particle (hot dark matter) and thus not compatible with the CDM thesis. Moreover, it has been shown that neutrinos only account for a small part of the the total energy density in the Universe (order of 1%) [31]. Beyond the SM, right-handed (sterile) neutrinos are being investigated as a viable CDM candidate. A comprehensive overview of keV-scale sterile neutrino DM is given in [32].

Another beyond SM candidate is given by the WIMP, an acronym for Weakly Interacting Massive Particle. As the name suggests, this proposed particle does only interact weakly (small couplings) with other particles. The WIMP is per definition

non-baryonic and non-relativistic. Many extensions of the SM, like the supersymmetry (SUSY), predict particles with properties of the WIMP [33]. One of the main reasons that make the WIMP so popular amidst the other DM particle candidates is the so called *WIMP miracle*, which goes as follows. Assuming that DM was created thermally, in the early Universe thermal equilibrium prevailed and the number density of DM particles was approximately equal to the number density of photons [10]. In equilibrium there is constant creation and annihilation of DM pairs $\chi\overline{\chi}$ from SM fermion pairs $f\overline{f}$ and vice versa, in an inelastic process:

$$\chi\overline{\chi} \quad \longleftrightarrow \quad f\overline{f} \tag{1.4}$$

As the Universe expands, less DM particles find a partner to annihilate and the DM freeze-out occurs (CDM is already non-relativistic at this point). After the freeze-out, the abundance of DM particles stays almost constant to this day. This relic abundance can be calculated by following the evolution of the inelastic process (1.4) with time, using the Boltzmann equation (for a thorough and illustrative description of the required calculation the reader is referred to [10]). The final expression for the DM relic density is related to the cross section of the DM annihilation process. The remarkable "miracle" is, that a weakly interacting DM particle gives a value for the relic density which is compatible with the results from cosmology. In the context of the DM relic density, one often refers to the Lee-Weinberg bound. Benjamin Lee and Steven Weinberg showed in 1977, that in order for a heavy neutral lepton (at that time heavy neutrinos were a popular DM candidate) to explain the measured DM relic density, its mass would have to be greater than 2 GeV [34]. The mass of the classical WIMP is thus usually of order GeV to TeV. However, in more recent studies it was argued, that sub-GeV WIMPs can still produce the respective relic density, if new light bosons are introduced [35, 36]. In this thesis, the DM particle is assumed to be a WIMP (i.e. obeys the WIMP miracle), with mass in the order of a few GeV.

There is also the possibility of non-thermal production of DM, a good example for this is the axion. The idea for the axion arose in order to resolve the strong CP problem, which lies within the fact that Quantum Chromodynamics (QCD) seems to conserve CP-symmetry. The QCD Lagrangian contains the term

$$\mathcal{L}_{\mathrm{QCD}} = \frac{\theta}{32\pi}\varepsilon^{\mu\nu\rho\sigma}G^a_{\mu\nu}G^a_{\rho\sigma} \tag{1.5}$$

where $G^a_{\rho\sigma}$ is the gluon tensor and θ a static coupling. Non-perturbative effects give rise to a neutron-electric dipole moment $|d_n| \approx 5 \times 10^{-16}\theta\, e\,\mathrm{cm}$ [8]. However,

experimental results place a very low upper bound of $d_n \lesssim 10^{-26}\, e\,\mathrm{cm}$ [37] on this quantity, forcing θ to be less than 10^{-10} [38]. Peccei and Quinn proposed a new global symmetry $U(1)_{PQ}$ which is spontaneously broken, to explain the smallness of θ [39]. This symmetry replaces the static CP-violating θ with a dynamical CP-conserving field. The axion is then the Nambu-Goldstone boson of the broken $U(1)_{PQ}$ symmetry [40]. At the minimum of the effective potential of the axion field, θ vanishes and the strong CP problem is thus solved. For a mass of order $m_a \approx 1 \times 10^{-5}\,\mathrm{eV}$ non-thermal produced axions could account for the whole CDM content in the Universe [38]. There are experiments which are aiming for direct detection of cosmological axions, like the Axion Dark Matter Experiment (ADMX) [41], while the CERN Axion Solar Telescope (CAST) is searching for axions originating from the sun [42]. It is important to note, that while the production mechanism could also be thermal, the axion would then be too short lived on the time scale of the Universe to explain DM [8].

1.3 Detection of dark matter

There are three main approaches to the search of particle DM: production at colliders, indirect detection via DM annihilation products and direct detection through DM scattering off target nuclei and electrons. The DM-SM interaction is schematically displayed in Figure 1.4 with arrows illustrating possible dark matter detection channels. It is important to note, that if an experiment of one type is successful in its search, the result has to be compatible with limits from experiments of the other types. As the title presumes, this thesis' focus lies within direct detection of DM. In the following, the other two detection types will be briefly commented on, before turning to the search for WIMP-nucleus scattering.

The goal of collider experiments in accelerators is the production of DM particles in high-energy collision of SM particles. The Large Hadron Collider (LHC) at CERN with its unmatched collision energy of 13 TeV, is the leading apparatus for such searches. The production of a DM particle-antiparticle pair in a collision process at the LHC could be detected as missing transverse momentum. If the DM pair is produced via an s-channel exchange of a new particle[2], this can be studied by a resonance search [43]. General purpose detectors such as ATLAS, BELLE or CMS, which are searching for beyond SM events, have so far not found any evidence for

[2]This new particle would then, as the DM itself, be part of the so called dark sector (hidden sector) which consists of yet-unknown particles beyond the SM.

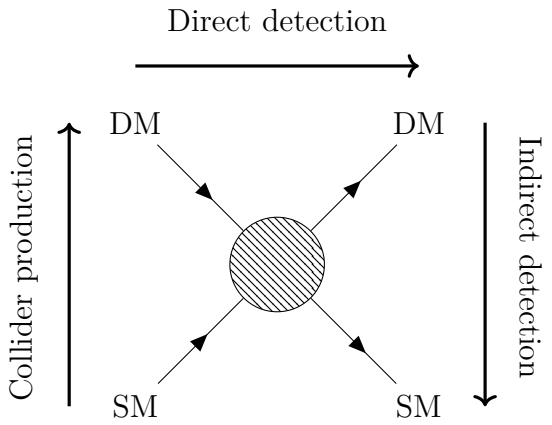

Figure 1.4: Schematic display of how possible channels of the DM-SM interaction are used in different search approaches. As in a Feynman diagram incoming particles are marked by arrows in direction of momentum, while for antiparticles the arrow points in the opposite direction.

DM-pair production, but have published limits on DM specific quantities like mass and couplings [43–45]. Limits from high energy collision are sensitive to the precise model of DM-SM interaction which was assumed. One thus has to be careful when comparing limits from direct detection and collider experiments.

Even after the freeze out, DM pair annihilation might still be present in denser regions of the Universe. Indirect detection experiments aim at detecting the SM particles which could be produced in these annihilation processes of DM pairs. There is a broad range of possible annihilation signatures ranging from charged particles and antiparticles, over photons in the form of gamma or X-rays, to neutrinos. The range of experiments is just as broad, with ground-based telescopes (MAGIC, HESS, etc.) and the Fermi-LAT telescope in orbit, as well as other earthbound detectors like Super-Kamiokande and IceCube.

The third possibility is given by direct detection experiments, which aim to detect interactions of DM particles in the targets of detectors. Although Earth is located rather far away from the Milky Way's center, it is still situated well within the supposed DM halo. Estimates of the local DM density (1.1) thus suggest that a sufficient number of DM particles should pass through an earthbound detector. Nevertheless, the fact that DM particles only couple very weakly to ordinary matter still leads to very low expected scattering rates which poses a challenge for direct detection experiments. In addition, the relatively low mass of a particle DM candidate results in typical recoil energies of only a few keV being deposited in the detector. These two challenges require highly sensitive devices for DM direct detection which are ideally operated in a low-background environment. The quantity

of interest for direct DM searches is the differential event rate (differential recoil spectrum), which gives the spectral shape of the event distribution depending on target material and exposure. The according formula has contributions from astro-, particle and detector physics and goes as follows [10]:

$$\frac{dR}{dE_R}(E_R) = \frac{\rho_\chi}{m_N m_\chi} \int_{v_{\min}(E_R)}^{v_{\text{esc}}} f(\vec{v}) v \frac{d\sigma(\vec{v}, E_R)}{dE_R} \tag{1.6}$$

The first fraction includes the DM density ρ_χ (1.1), the mass of the DM particle m_χ and the molecular mass of the target material m_N[3]. The next part gives the integral over the WIMP velocity distribution $f(\vec{v})$, where the available velocities are bound from below by $v_{\min}$, which gives the minimum speed a WIMP has to have in order to induce a nuclear recoil of energy E_R. Due to the fact, that the detectors are earth bound, the DM particle is bound by the galactic escape velocity, which gives the upper limit of the integral. The last term is a contribution from particle physics, namely the differential DM-nucleus scattering cross section $\frac{d\sigma}{dE_R}$. The procedures on how to calculate the velocity integral, as well as the differential cross section for the interaction models used in this thesis are described in the next chapter.

Direct detection experiments have not yet announced any non-controversial excess which could be interpreted as a DM signal [9]. Experiments thus publish exclusion limits on DM specific parameters, which can be used for comparison between experiments and as a measure to track the progress made in the field. The most popular choice of parameters for these limits is the DM-nucleon reference cross section, which is defined in the next chapter, as a function of the DM mass.

The method used in order to detect DM events and measure the recoil energy deposited in the detector depends strongly on the target material. In solid state materials like silicon, germanium, calcium tungstate or sodium iodide which are operated as cryogenic detectors, a DM recoil induces a phonon signal (i.e. rise in temperature) which can be measured with a calorimeter. In addition to the phonon signal, a particle interaction might also result in either an ionization signal (Ge, Si) or a scintillation signal ($CaWO_4$, NaI). There are also experiments which use liquid noble gases, like Xenon, as a target material which can also emit scintillation light. The first generation of direct DM searches usually used only one of the above methods to detect a signal, for example the CRESST-I [46] or DAMA [47]

[3]For composite targets the rate is given by adding up the spectra for each element in the target molecule scaled to its respective fraction within the whole molecule. For example for sodium iodide: $\left(\frac{dR}{dE_R}\right)_{\text{NaI}} = \frac{m_{\text{Na}}}{m_{\text{I}}+m_{\text{Na}}}\left(\frac{dR}{dE_R}\right)_{\text{Na}} + \frac{m_{\text{I}}}{m_{\text{I}}+m_{\text{Na}}}\left(\frac{dR}{dE_R}\right)_{\text{I}}$.

experiments. Up to date experiments combine two signal-channels in order to better discriminate background events from a possible signal. The CDMS [17] experiment uses a combination of phonon and ionization signal, while the newer generations of the CRESST [16] experiment measure both phonon signal and scintillation light. The COSINUS experiment [19], which is currently under construction, aims to confirm (or falsify) the annual modulation in the DM signal which was observed by the DAMA experiment [47]. The COSINUS experiment combines the target material of its competitor, sodium iodide, with a dual-channel readout (phonon signal and scintillation light)[19].

In the above we have seen, that there is plenty of evidence for the existence of a DM particle and a multitude of different candidates, with the WIMP being one of the most promising. The connection between the theoretical properties of the WIMP and the possible detection in a direct detection experiment is given by the differential recoil spectrum (1.6). The following chapter will focus on determining the particle physics expressions which are necessary in calculating the expected differential recoil spectrum for a given experiment. Different types of interaction between DM and SM will be considered in order to find the respective cross sections. Among them the centerpiece of this thesis: the interaction via two mediator particles.

Chapter 2

DM-SM interaction

In the previous chapter the differential recoil spectrum (1.6) was introduced as an important tool to predict measurable events in direct DM detection experiments. Since the differential recoil rate describes the interaction between a DM particle and a nucleus, it will also be referred to as nuclear recoil rate or nuclear recoil spectrum (NRS). Recoil spectra are described by a complex formula with contributions from many physical disciplines, some of which have already been discussed above. This chapter will focus mainly on the particle physics aspect needed in the calculation of the NRS, namely the DM-nucleus scattering cross section.

In the following the DM particle is assumed to be a WIMP, more precisely a Dirac fermion which has some small coupling to ordinary matter. Moreover, since the structure evolution of the universe implies cold DM, all calculations are performed in the non-relativistic limit. As a further simplification it is assumed, that the scattering between WIMP and the nucleus is an elastic process

$$\chi + N \longrightarrow \chi + N. \tag{2.1}$$

The WIMP-nucleus cross section depends strongly on the interaction strength between the WIMP and SM quarks [1], and these quantities thus need to be found in a first step of the calculation. Then the arrangement of quarks in the nucleons and at last the distribution of the nucleons in the nucleus have to be taken into account. Calculating the cross section thus consists of three steps which will be described over the next sections.

[1] In the most general case the DM interaction with gluons in the nulceons also has to be considered. However, since we assume that the WIMP is neutral under both electromagnetism and color, there is no scattering of gluons at tree level [48].

The fact that DM interacts with the SM implies that, besides specifying the new DM particle, one also has to specify the portal (mediator) over which the communication between dark and ordinary matter takes place. This mediator particle might now either be a SM particle, the Higgs boson is frequently discussed in this matter (for a timely summary see [49]), which through some additional symmetry also couples to the dark sector [50]. However, the portal itself might be part of the dark sector (dark portal) and couple to both DM and the SM. In the first part of this chapter the WIMP quark interaction is assumed to take place via a single dark portal. Within the second part of this chapter the main concept of this thesis will be introduced, namely the SM-DM interaction via two mediator particles.

2.1 Single portal models

The DM-nucleus scattering cross section depends on properties of the DM particle χ as well as on the type of mediator particle ϕ' [51]. The Lagrangian of the theory contains the interaction terms

$$\mathcal{L} \supset \overline{\chi} g_{\chi\phi'} \Gamma_\chi \chi \phi' + \overline{Q} g_{Q\phi'} \Gamma_Q Q \phi' \tag{2.2}$$

where the last term describes the mediator's interaction with quarks (quarks are denoted with a capital Q to avoid confusion with the momentum transfer q). The choice of $\Gamma_{\chi,Q} = \{\mathbb{1}, \gamma^5, \gamma^\mu, \gamma^5\gamma^\mu, \sigma^{\mu\nu}\}$ is given by type of mediator interaction (scalar, pseudo-scalar, vector,pseudo-vector, tensor) and $g_{\chi\phi'}$ and $g_{Q\phi'}$ are couplings. Exemplary Feynman diagrams at tree level for DM-quark scattering are shown in Figure 2.1. The mass terms in the Lagrangian amount to $\frac{1}{2}m_{h'}^2 h'^2$ and $\frac{1}{2}m_{Z'}^2 Z'^\mu Z'_\mu$, in the case of scalar and vector mediator, respectively [48].

In the context of direct detection of relatively heavy DM particles, an effective field theory (EFT) description applies. The low velocities of the DM particles hitting the detector $v \leq v_{\text{esc}}$, imply energies involved in the scattering process with ordinary matter of order 10 keV for a GeV mass DM particle. The DM–quark scattering can thus essentially be described by an NR effective potential with two small expansion parameters: the DM velocity $v/c \approx 10^3$ and $|\vec{q}|/\Lambda$ [52]. Here $q \approx \mathcal{O}(10 - 100\text{MeV})$ describes the momentum transfer, which is related to the recoil energy E_R by $q^2 = 2m_N E_R \propto v^2$. Λ is some large scale parameter such as the DM mass m_χ, the nucleus mass m_N or possibly the mass of a heavy mediator particle $m_{\phi'}$ [51]. The appropriate EFT for DM direct detection experiments then consists of a set of four-

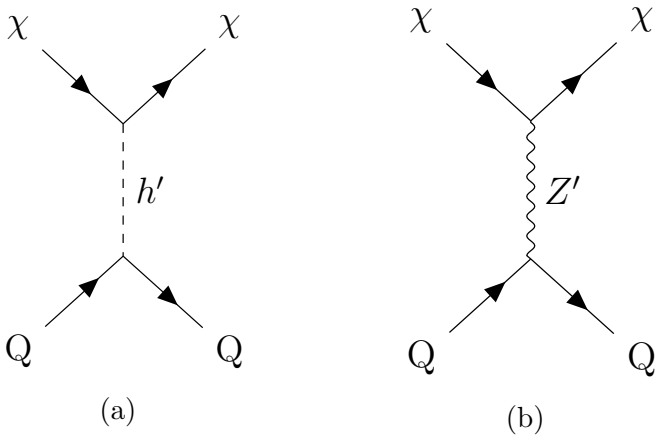

Figure 2.1: Two possible scenarios for DM-quark scattering at tree level. In a) a scalar mediator exchange is displayed and in b) a vector mediator exchange.

fermion operators for the interactions of DM with the quarks in the nucleons in the NR limit. Many DM interaction models which are different on a microscopic scale lead to the same NR EFT - it is thus a good approach for a model-independent description of DM scattering in direct detection experiments. An extensive analysis and an overview of NR EFT operators, together with the respective matched field theory operators, are given in [51] and [52]. For the purpose of the present study, which also involves lighter mediators, we have to consider the less general approach of simplified interaction models.

For this thesis only the subset of operators which are responsible for spin-independent interaction are considered. This is well reasoned by the fact, that spin-dependent interactions are suppressed for the low velocities and energies present at DM direct detection. The subset of nucleus spin-independent NR operators in the centre of mass frame, as classified in [51], are listed in Table 2.1. The reduced DM-nucleus mass is denoted by $\mu_N = \frac{m_N m_\chi}{m_N + m_\chi}$ and the relative DM incoming velocity by $\vec{v} = \vec{v}_{\chi,\text{in}} - \vec{v}_{N,\text{in}}$. One can see in Table 2.1, that the operators which contain a γ^5 matrix (axial scalar, axial vector and axial tensor) depend on the spin of the DM particle $\vec{s}_\chi$. We will thus further restrict our analysis to interaction via a scalar and a vector mediator, as the other operators are again suppressed in $\vec{q}$ and $\vec{v}$. The effective four-fermion interaction for a heavy mediator ϕ' of mass $m_{\phi'}^2 \gg q^2$ is then of the form

$$\mathcal{L}_{4f} = \frac{1}{m_{\phi'}^2} g_{Q\phi'} g_{\chi\phi'} \overline{\chi} \Gamma_\chi \chi \overline{Q} \Gamma_Q Q. \tag{2.3}$$

This expression corresponds to integrating out the heavy mediator in the relevant terms of the full Lagrangian (2.2). In the heavy mediator limit the interaction can

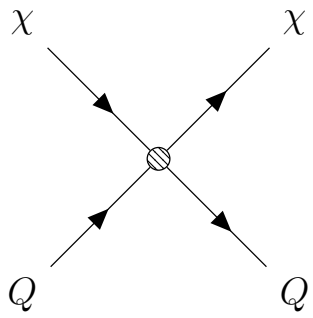

Figure 2.2: Schematic Feynman diagram of χ-Q scattering representing contact interaction in the case of a heavy mediator.

be described as contact-like and is schematically displayed as a Feynman diagram in Figure 2.2. Since only scalar and vector interactions are considered $\Gamma = \{\mathbb{1}, \gamma^\mu\}$.

In the following analysis also the case of mediator with a mass $m_{\phi'} \leq q^2$ will be considered. For such a light mediator, one can not assume anymore that the mediator propagator is shrunk to a point (as in Figure 2.2). Instead the momentum transfer has to be considered to first order in the NR expansion in the calculation of scattering amplitudes in a so called simplified model [53, 54], i.e.

$$\frac{1}{m_{\phi'}^2} \quad \rightarrow \quad \frac{1}{m_{\phi'}^2 + q^2} \tag{2.4}$$

In the following calculation of scattering amplitudes, the factor corresponding to the dark mediator propagator will be denoted by $G(m_{\phi'}, q^2)$, with

$$G(m_{\phi'}, q) = 1/m_{\phi'}^2 \quad \text{and} \quad G(m_{\phi'}, q) = 1/(m_{\phi'}^2 + q^2) \tag{2.5}$$

for a heavy and a light ϕ' respectively. One should note, that this notion is consistent, as in the case of $m_{\phi'} \gg q^2$ the light particle propagator reduces to the heavy particle propagator.

For the low energy regions probed by direct detection experiment, we can now use the above stated interactions in order to calculate the scattering amplitudes at tree level. The calculations in the following chapter are on the same lines as those in the appendix of [48] using methods and notations as in the classic text book by Peskin and Schroeder [55].

Table 2.1: Leading NR operators for spin-independent DM-quark interaction together with their matched field theory operators. Excerpt of the set of operators in [51].

	EFT operator	NR operator in momentum space	NR operator in position space
scalar × scalar	$\overline{\chi}\chi\overline{Q}Q$	1	$\delta^3(\vec{r})$
axial scalar × scalar	$\overline{\chi}\gamma^5\chi\overline{Q}Q$	$i\vec{s}_\chi \cdot \vec{q}$	$-\vec{s}_\chi \cdot \vec{\nabla}\delta^3(\vec{r})$
vector × vector	$\overline{\chi}\gamma^\mu\chi\overline{Q}\gamma_\mu Q$	1	$\delta^3(\vec{r})$
axial vector × vector	$\overline{\chi}\gamma^5\gamma^\mu\chi\overline{Q}\gamma_\mu Q$	$\vec{s}_\chi^{\perp} \cdot \vec{v}$	$(\vec{s}_\chi \cdot \vec{v} + \frac{i}{2\mu_N}\vec{s}_\chi \cdot \vec{\nabla})\delta^3(\vec{r})$

2.1.1 From quarks to nucleons

To begin with, the matrix element of the interaction of a nucleus N with a DM Dirac fermion via a scalar mediator h' is examined. It is important to note, that the scalar interactions considered are different from the widely used Yukawa type. The incoming momenta for DM and the nucleus are denoted by p and k respectively, the outgoing by p' and k'. The momentum transfer of the interaction is thus $q = p - p' = k' - k$. The S-matrix element at tree level is then of the form

$$\mathcal{M}\delta^{(4)}(p+k-p'-k') = \tag{2.6}$$
$$G(m_{h'},q)\sum_Q g_{Qh'}g_{\chi h'}\,\langle\chi_f(p'),N_f(k')|\,T\left(\int d^4x\overline{\chi}(x)\chi(x)\overline{Q}(x)Q(x)\right)|\chi_i(p),N_i(k)\rangle\,,$$

where $T()$ denotes the time-ordered product and the sum is over all quark flavours. With the appropriate contractions according to Wick's theorem this reduces to

$$\mathcal{M}\delta^{(4)}(p+k-p'-k') = G(m_{h'},q)\sum_Q\Bigg(g_{Qh'}g_{\chi h'} \tag{2.7}$$
$$\int d^4x\langle\overbrace{\chi_f(p')|\overline{\chi}(x)}\overbrace{\chi(x)|\chi_i}(p)\rangle\langle\overbrace{N_f(k')|\overline{Q}}(x)\overbrace{Q(x)|N_i}(k)\rangle\Bigg).$$

We start by calculating the first contraction which consists only of DM Dirac fermions and thus gives

$$\langle\overbrace{\chi_f(p')|\overline{\chi}}(x)\overbrace{\chi(x)|\chi_i}(p)\rangle = \overline{u}_{s'}(p')e^{ip'\cdot x}u_s(p)e^{-ip\cdot x}, \tag{2.8}$$

where the $u(p)$ are Dirac spinors and s/s' denote the spin of the initial/final DM

particle. Using the NR spinor identities from section A.2 the above simply reads

$$\langle \overbrace{\chi_f(p')|\overline{\chi}}(x)\overbrace{\chi(x)|\chi_i}(p\rangle = 2m_\chi \xi^\dagger_{s'}\xi_s e^{i(p'-p)\cdot x}. \tag{2.9}$$

Summing (averaging) over final (initial) spin states for the fermionic DM, the two-spinors will just contribute as $\frac{1}{2s_\chi+1}\sum_{s,s'}|\xi^\dagger_{s'}\xi_s|^2 = 1$ for Dirac fermionic DM of spin $s_\chi = \frac{1}{2}$.

Secondly the quarks in the nucleus state are analysed. To start with, the translation operator is used in order to separate the coordinate dependence (for the sake of readability contraction brackets are not shown)

$$\begin{aligned}\langle N_f(k')|\overline{Q}(x)Q(x)|N_i(k)\rangle &= \langle N_f(k')|e^{iPx}\overline{Q}(0)e^{-iPx}e^{iPx}Q(0)e^{-iPx}|N_i(k)\rangle \\ &= \langle N_f(k')|\overline{Q}(0)Q(0)|N_i(k)\rangle e^{i(k-k')\cdot x}.\end{aligned} \tag{2.10}$$

In the limit of small momentum transfer one can thus work with quarks in nuclear states at rest, which will be denoted simply by $\langle N|\overline{Q}Q|N\rangle$. Equation (2.6) can thus be rewritten as

$$\begin{aligned}\mathcal{M}\delta^{(4)}(p+k-p'-k') =& G(m_{h'},q)\sum_Q\Bigg[g_{Qh'}g_{\chi h'} \\ &\int d^4x\left(2m_\chi e^{i(p'-p)\cdot x}\langle N|\overline{Q}Q|N\rangle e^{i(k'-k)\cdot x}\right)\Bigg]\end{aligned} \tag{2.11}$$

and performing the integral over x:

$$\mathcal{M} = 2m_\chi G(m_{h'},q)\sum_Q g_{Qh'}g_{\chi h'}\langle N|\overline{Q}Q|N\rangle \tag{2.12}$$

The calculation of the quark-nucleus term is performed in two steps: first the matrix elements of the quarks in the nucleon states n (proton or neutron) is evaluated and in the next section the substructure of the nucleus is accounted for. For the three light quarks ($Q = u, d, s$) the matrix element at vanishing momentum transfer $\langle n|\overline{Q}Q|n\rangle$ is related to the mass of the nucleons and can be obtained from determinations of the pion-nucleon sigma term [56–59]

$$\langle n|m_{Q=u,d,s}\overline{Q}Q|n\rangle = m_n f^{(n)}_{T_{Q=u,d,s}}. \tag{2.13}$$

The superscript (n) denotes either a proton or a neutron state. The precise determination of the pion-nucleon sigma term is still an open issue, see for example [60]. The parameters $f_{T_{Q=u,d}}$ are of order 10^{-2} [59] and are set equal to zero in several analysis.

This is based on the fact that choosing $f_{T_{Q=u,d}} = 0$ is usually less significant, than the uncertainty in $f_{T_{Q=s}}$ [33]. The heavy quarks ($Q = t, b, c$) contribute to the mass of the nucleon through the triangular [61]. Under the heavy quark expansion the nucleon mass is given by

$$m_n = \langle n|m_u\overline{u}u|n\rangle + \langle n|m_d\overline{d}d|n\rangle + \langle n|m_s\overline{s}s|n\rangle + \langle n|\frac{-9\alpha_s}{8\pi}G^a_{\mu,\nu}G^{a,\mu\nu}|n\rangle, \tag{2.14}$$

where $G^a_{\mu,\nu}$ is the gluon field strength tensor and α_s is the quark-gluon coupling constant. The last term in (2.14) is due to the QCD trace anomaly. Thus each heavy quark contributes to the matrix element in the following way [33]

$$\langle n|m_{Q=b,t,c}\overline{Q}Q|n\rangle = \frac{2}{27}m_n\left[1 - \sum_{Q=u,d,s} f^{(n)}_{T_Q}\right]. \tag{2.15}$$

The quarks in the nucleon state thus contribute to the full matrix element as

$$f_{n,p} \equiv \sum_Q g_{Qh'}g_{\chi h'}\langle n|\overline{Q}Q|n\rangle = \tag{2.16}$$
$$\sum_{Q=u,d,s} g_{Qh'}g_{\chi h'}\frac{m_{n,p}}{m_Q}f^{(n,p)}_{T_Q} + \sum_{Q=b,t,c} g_{Qh'}g_{\chi h'}\frac{m_{n,p}}{m_Q}\frac{2}{27}m_{n,p}\left[1 - \sum_{Q=u,d,s} f^{(n,p)}_{T_Q}\right]$$

for each neutron with terms $f^{(n)}_{T_Q}$ and for each proton with the according $f^{(p)}_{T_Q}$s. Note that the couplings $g_{Qh'}g_{\chi h'}$ are absorbed in the definitions of f_n and f_p.
Before evaluating how the full quark-nucleus matrix element arises from the nucleon matrix elements we will analyze another type of interaction between DM and quarks, namely that via a vector mediator Z'. The appropriate EFT Lagrangian is then

$$\mathcal{L} = g_{QZ'}g_{\chi Z'}G(m_{Z'}, q)\overline{\chi}\gamma^\mu\chi\overline{Q}\gamma_\mu Q. \tag{2.17}$$

Overall the calculation is similar to the scalar case. For the DM correlator the calculation from section A.2 and averaging over initial/summing over final spin states s_χ gives

$$\langle\overline{\chi_f(p')|\overline{\chi}}(x)\gamma^\mu\overline{\chi(x)|\chi_i}(p)\rangle = 2m_\chi\delta^{0\mu}e^{i(p'-p)\cdot x}, \tag{2.18}$$

thus only the temporal component of the vector current survives. For the quark-nucleon matrix element the vector current at zero momentum transfer counts the valence quarks, so sea quarks and gluons do not need to be considered [33, 62]. Thus

for a proton

$$\sum_Q g_{QZ'} g_{\chi Z'} \langle p|\overline{Q}\gamma_m u Q|p\rangle = (2g_{uZ'} g_{\chi Z'} + g_{dZ'} g_{\chi Z'})\delta_{0,\mu} \tag{2.19}$$

and for a neutron

$$\sum_Q g_{QZ'} g_{\chi Z'} \langle n|\overline{Q}\gamma_\mu Q|n\rangle = (2g_{dZ'} g_{\chi Z'} + g_{uZ'} g_{\chi Z'})\delta_{0,\mu}. \tag{2.20}$$

As mentioned earlier, the three interaction types left in Table 2.1 - axial scalar, axial vector and axial tensor - contain a γ^5 matrix which needs to be considered when calculating the NR-limit of Dirac spinor products similar to (2.8) and (2.18). In all three cases this calculation leads to an additional dependence of the matrix element on the momentum transfer $\vec{q}$ (for axial scalar and tensor) or the incoming DM velocity $\vec{v}$ (axial vector) [51], as well as the spin of the DM fermion. As an example the NR limit calculation of $\overline{u}_{s'}(p')\gamma^5 u_s(p)$ is performed in appendix section A.2. The additional $\vec{q}$, $\vec{v}$ and DM spin dependencies may lead to alternatively shaped recoil spectra, however, as pointed out before, these interactions are suppressed at direct detection.

2.1.2 From nucleons to nuclei

In the last step of calculating the nucleus - DM matrix element, one has to evaluate the matrix elements of the nucleon operators $\overline{p}p$ and $\overline{n}n$ in a nuclear state N. For the spin-independent cases of scalar or vector mediators, no spin structure occurs in the nucleon operators at zero momentum transfer and thus the operators simply count the nucleons:

$$\langle N|\overline{Q}\Gamma_Q Q|N\rangle = Z\langle p|\overline{Q}\Gamma_Q Q|p\rangle + (A-Z)\langle n|\overline{Q}\Gamma_Q Q|n\rangle \tag{2.21}$$

However, at non-zero momentum transfer q the interaction becomes sensitive to structure and size of the nucleus which can be described with nuclear form factors [33]. Generally the form factor associated with the nucleon-number operator can be described by the Fourier transform of the according nuclei's density. In DM searches the Helm form factor [63]

$$F(q) = 3\frac{j_1(qR_0)}{qR_0}\exp\left(-\frac{1}{2}q^2 s^2\right) \tag{2.22}$$

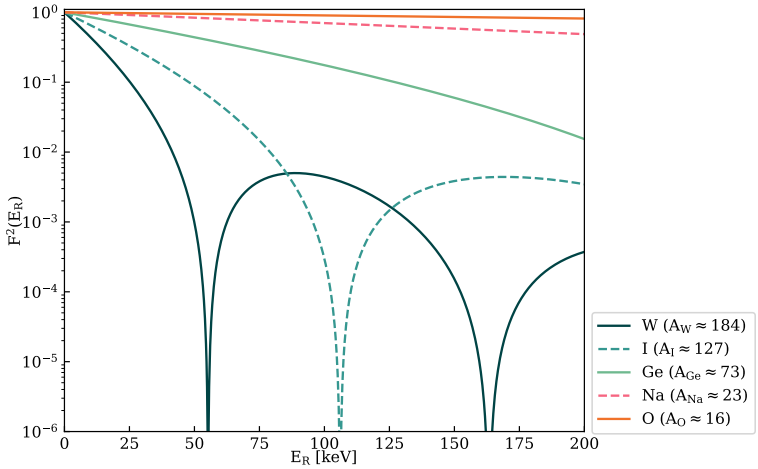

Figure 2.3: The dimensionless squared Helm form factor (2.22) as a function of the recoil energy E_R in keV for various target materials. For lighter elements like oxygen or calcium the form factor stays almost constant while for heavy nuclei it decreases at higher energies.

is commonly used[2], where j_1 is the first spherical Bessel function and R_0 the nuclear radius. It was shown by Lewin and Smith [64], that a suitable way to calculate the nuclear radius is given by

$$R_0 = \sqrt{c^2 + \frac{7}{3}\pi^2 a^2 - 5s^2} \tag{2.23}$$

with parameters

$$a \coloneqq 0.52\,\text{fm}, \quad s \coloneqq 0.9\,\text{fm}, \quad c \coloneqq 1.23 \times A^{1/3} - 0.6\,\text{fm}. \tag{2.24}$$

In Figure 2.3 the quadratic Helm form factor is shown as a direct function of the recoil energy E_R for various targets. While the form factor stays close to its value at zero momentum transfer for light target nuclei, for heavy elements such as tungsten it falls significantly for higher energies. Note also that the form factor is normalized to 1 at zero momentum transfer.

So far the calculation of nucleus-quark matrix element was performed in the relativistic regime, for the application to DM direct detection, however, the NR limit has to be considered. The relativistic matrix element is related to the NR one via [51]:

$$\langle N|\overline{Q}\Gamma_Q Q|N\rangle_{\text{NR}} = \frac{\langle N|\overline{Q}\Gamma_Q Q|N\rangle_{\text{R}}}{2m_N} \tag{2.25}$$

[2]For heavy nuclei, such as tungsten, which are heavily deformed and not spherical, the Helm form factor might not be a suitable and other nuclear models might yield better results.

In the case of a scalar mediator the matrix element thus amounts to

$$\mathcal{M}_{h'} = 4m_\chi m_N G(m_{h'}, q)[Zf_p + (A - Z)f_n]F(q). \tag{2.26}$$

Introducing the new variables $\vartheta \coloneqq \arctan(f_n/f_p)$, as well as $g_{h'} \coloneqq \sqrt{f_n^2 + f_p^2}$ the squared matrix element can be rewritten as

$$|\mathcal{M}_{h'}|^2 = 16m_\chi^2 m_N^2 g_{h'}^2 G^2(m_{h'}, q)[Z\cos\vartheta + (A - Z)\sin\vartheta]^2 F^2(q). \tag{2.27}$$

Similarly for the interaction via a vector mediator the matrix element is given by

$$\begin{aligned}\mathcal{M}_{Z'} &= 4m_\chi m_N G(m_{Z'}, q) g_{\chi Z'}[Z(2g_{uZ'} + g_{dZ'}) + (A - Z)(2g_{dZ'} + g_{uZ'})]F(q) \\ &= 4m_\chi m_N G(m_{Z'}, q) g_{\chi Z'}[Z(g_{uZ'} - g_{dZ'}) + A(2g_{dZ'} + g_{uZ'})]F(q).\end{aligned} \tag{2.28}$$

Under the assumption that Z' couples universally to all quarks we define $g_{\chi Z'} g_{dZ'} = g_{\chi Z'} g_{uZ'} =: g$ and the squared matrix element simplifies to

$$|\mathcal{M}_{Z'}|^2 = 16m_\chi^2 m_N^2 g^2 G^2(m_{Z'}, q)(3A)^2 F^2(q). \tag{2.29}$$

It is important to note, that under the common assumption $f_n = f_p$, implying $\vartheta = \pi/4$, the charge number dependence vanishes in (2.26) ($\cos(\pi/4) = \sin(\pi/4)$) and the matrix elements for the scalar and vector interaction are identical up to some constant factor which can be absorbed in the definition of g.

2.1.3 Non-relativistic kinematics and cross sections

To obtain the NR cross section we start with the expression for the 2-to-2 spin-independent differential scattering cross section in the center of mass (COM) frame from [65]

$$\frac{d\sigma(\chi_i + N_i \to \chi_f + N_f)}{d\cos\theta} = \frac{|\vec{p}_f|}{32\pi s|\vec{p}_i|}|\mathcal{M}(\chi_i + N_i \to \chi_f + N_f)|^2. \tag{2.30}$$

In this formula θ is the scattering angle, $s = E_{\text{COM}}^2 = (p+k)^2$ the COM energy, $|\vec{p}_i| = \frac{1}{2\sqrt{s}}\lambda^{1/2}(s, m_{N_i}, m_{\chi_i})$ and $|\vec{p}_f| = \frac{1}{2\sqrt{s}}\lambda^{1/2}(s, m_{N_f}, m_{\chi_f})$ are the initial and final three momenta defined via the Källén function $\lambda(x, y, z) = x^2+y^2+z^2-2(xy+yz+zx)$. For the elastic scattering process $m_{N_i} = m_{N_f}$ as well as $m_{\chi_i} = m_{\chi_f}$, and thus $|\vec{p}_i| = |\vec{p}_f|$. Moreover, in the NR limit the COM energy is simply given by $E_{\text{COM}} \approx m_\chi + m_N$

and thus (2.30) amounts to

$$\frac{d\sigma}{d\cos\theta} = \frac{|\mathcal{M}|^2}{32\pi(m_\chi + m_N)^2}. \tag{2.31}$$

However, for the differential recoil rate the cross section is needed as a function of the recoil energy and not of the scattering angle. This can be achieved by using $\frac{d\sigma}{dE_R} = \frac{d\sigma}{d\cos\theta}\frac{d\cos\theta}{dE_R}$ and the scattering angle dependent expression (A.7) derived for the recoil energy in appendix A.1. The final expression is thus

$$\frac{d\sigma}{dE_R} = \frac{m_N}{32\pi\mu_N^2 v^2(m_\chi + m_N)^2}|\mathcal{M}|^2 = \frac{1}{32\pi m_N v^2}|\mathcal{M}|^2, \tag{2.32}$$

with the incoming DM velocity v and the reduced DM-nucleus mass μ_N. In literature and results published by DM direct detection experiments the differential cross section is often expressed in terms of a so called zero-momentum transfer nucleon reference cross section σ_n (sometimes also denoted by σ_p). This reference cross section is especially useful if one wants to analyse the DM-SM interaction in an interaction model independent way. Moreover, since it is a nucleon-DM cross section, it is independent of the target material and thus a quantity comparable over various experiment. In order to define σ_n, one starts by defining the quantity

$$\sigma_0 = \int_0^{E_{\max}=\frac{2\mu_N^2 v^2}{m_N}} dE'_R \frac{d\sigma(E'_R = 0)}{dE_R} \tag{2.33}$$

$$= \frac{2\mu_N^2 v^2}{m_N}\frac{d\sigma(E'_R = 0)}{dE_R}, \tag{2.34}$$

where $\frac{d\sigma(E'_R=0)}{dE_R}$ is differential nucleus-DM cross section at zero momentum transfer. Since the cross section at zero momentum transfer is related to the cross section at non-zero momentum transfer by the form factor $F^2(q = \sqrt{2m_N E_R})$ with $F^2(0) = 1$ one can write

$$\begin{aligned}\frac{d\sigma}{dE_R} &= F^2(E_R)\frac{d\sigma(0)}{dE_R} \\ &= \frac{m_N}{2\mu_N^2 v^2}F^2(E_R)\sigma_0 \\ &= \frac{m_N}{2\mu_N^2 v^2}F^2(E_R)\frac{\mu_N^2}{\mu_p^2}A^2\sigma_p \\ &= \frac{m_N}{2\mu_p^2 v^2}F^2(E_R)A^2\sigma_p,\end{aligned} \tag{2.35}$$

where one introduces the nucleon reference cross section via $\sigma_0 = \frac{\mu_N^2}{\mu_p^2} A^2 \sigma_p$ [10, 48]. In the case of a light mediator particle ϕ', the additional momentum transfer dependence from the propagator has to be included, resulting in [54]

$$\frac{d\sigma}{dE_R} = \frac{m_N}{2\mu_n^2 v^2} \frac{m_{\phi'}^4}{(m_{\phi'}^2 + q^2)^2} A^2 \sigma_n F^2(q). \tag{2.36}$$

For a heavy mediator particle the additional factor $\frac{m_{\phi'}^4}{(m_{\phi'}^2+q^2)^2}$ reduces to 1.

2.1.4 Recoil spectra

In this section recoil spectra resulting from the cross sections above are calculated and analysed for different target materials, DM and mediator masses. The analysis is constricted to the vector mediator case, which is compliant as the cross section for the scalar mediator case at $\theta = \pi/4$ only differs from the vector case by some constant factor in the definition of the dimensionless coupling g. Using (2.29) together with (2.32) yields the following expression for the differential recoil rate:

$$\begin{aligned} \frac{dR}{dE_R} &= \frac{\rho_\chi}{m_\chi m_N} \int_{v_{\min}}^{\infty} d^3v f(\vec{v}) v \frac{d\sigma}{dE_R} \\ &= \frac{g_{Z'}^2 \rho_\chi}{2\pi m_\chi} G^2(m_{Z'}, E_R)(3A)^2 F^2(E_R) \underbrace{\int_{v_{\min}}^{\infty} d^3v \frac{f(\vec{v})}{v}}_{=:I(v_{\min})} \end{aligned} \tag{2.37}$$

The only expression left to evaluate is the integral $I(v_{\min})$ over the DM velocity distribution. In a first step, one assumes that the DM velocity is truncated at the finite escape velocity v_{esc} of the Milky Way. The WIMP velocities v_{gal} in the rest frame of the galaxy then follow a Maxwell-Boltzmann distribution of shape [66]

$$f_{\text{gal}}(v_{\text{gal}}) = \mathcal{N} \left(\frac{3}{2\pi w^2} \right)^{3/2} \exp\left(-\frac{3 v_{\text{gal}}^2}{2w^2} \right) \tag{2.38}$$

with the normalisation

$$\mathcal{N} = \left[\operatorname{erf}(z) - \frac{2}{\sqrt{\pi}} z \exp\left(-z^2\right) \right]^{-1}. \tag{2.39}$$

In the previous equations $z^2 = 3v_{\text{esc}}^2/(2w^2)$ and w denotes the root mean square velocity. Assuming that the DM halo of the Milky Way is an isothermal sphere, w is related to the asymptotic value of the rotational velocity v_∞ via $w = \sqrt{\frac{3}{2}} v_\infty$.

For an earthbound detector Earth's velocity $v_\oplus$ with respect to the galactic rest frame has to be taken into account. Adding up Earth's velocity around the Sun (not taking into account annual modulation and using the average velocity) and the Sun's velocity on its way through the galaxy yields [33]

$$v_\oplus = v_\infty \times 1.05. \tag{2.40}$$

Applying a Galilean transformation, the WIMP velocity in the Earth's rest frame is thus $v_{\text{gal}} + v_\oplus$. It is shown in [66], that in the case of a non rotating halo the velocity integral is described by

$$I(v_{\min}, v_{\text{esc}}, v_\infty) = \frac{\mathcal{N}}{\eta}\left(\frac{3}{2\pi w^2}\right)^{1/2} \times \begin{cases} \tau(x_{\min}-\eta, x_{\min}+\eta) - 2\eta\exp(-z^2) & x_{\min} < z-\eta \\ \tau(x_{\min}-\eta, z) - \exp(-z^2)(z+\eta-x_{\min}) & z-\eta \le x_{\min} < z+\eta \\ 0 & x_{\min} \ge z+\eta, \end{cases} \tag{2.41}$$

with the normalization $\mathcal{N}$ from (2.39), z as given above and the following definitions:

$$\tau(x,y) = \frac{\sqrt{\pi}}{2}(\text{erf}(y) - \text{erf}(x)) \tag{2.42}$$

$$\eta^2 = \frac{3v_\oplus^2}{2w^2} \tag{2.43}$$

$$x_{\min} = \frac{3v_{\min}^2}{2w^2} \tag{2.44}$$

An expression for the minimum WIMP velocity $v_{\min}$ as a function of the recoil energy is deduced in section A.1. In this work the standard International Astronomical Union value is used for $v_\infty = 220\,\text{km s}^{-1}$ [67]. The value of the galactic escape velocity is subject to large uncertainties and various values are being used in DM direct detection related work. For this thesis $v_{\text{esc}} = 544\,\text{km s}^{-1}$ is used, which lies within the 90% confidence level range of $450 - 650\text{km s}^{-1}$ deduced in [68] but is also a value agreeable with newer results such as [69]. This explicit value of the escape velocity is nowadays also the most commonly used in the analysis of data from DM direct detection experiments.

The differential recoil rate is usually given in the so called "differential rate unit (drn)", where 1 drn = 1 event/(kg day keV). An alternative description, generally

used by experiments with large detector masses, is events per (tonne detector material × keV recoil energy × years exposure). Since the cross section was calculated in natural units ($c = \hbar = G = k_B = 1$) a precise dimensional analysis of the components in (2.37) is needed in order to find the appropriate conversion factor. This analysis was done in detail in the appendix section A.3.

In order to fix $G^2(m_{Z'}, E_R)$ in (2.37) one must differentiate between a heavy mediator ($m_{\phi'}^2 \gg q^2$) with $G^2(m_{Z'}, E_R) = (m_{Z'}^4)^{-1}$ and a light mediator ($m_{\phi'}^2 \leq q^2$) with $G^2(m_{Z'}, E_R) = (m_{Z'}^2 + 2m_N E_R)^{-2}$. In the following the coupling g will be denoted by g_h for heavy mediators and by g_l for light mediators. The importance of this differentiation becomes apparent when plotting and comparing recoil spectra for heavy and light mediator cases. In Figure 2.4 the nuclear recoil rates on a sodium iodide (NaI) target are shown for both interaction via a heavy vector mediator $m_{Z'} = 100\,\mathrm{MeV}$ (left panel) and interaction via a light vector mediator $m_{Z'} = 10\,\mathrm{MeV}$ (right panel). In both cases the mass of the DM particle is 10 GeV and a coupling $g_h = g_l = 1 \times 10^{-12}$ is used. The values for the couplings are not chosen arbitrarily, but rather estimated from current DM direct detection limits for the reference nucleon cross section (2.36). Full particulars of this estimation process are given in section A.4. Together with the spectrum for NaI the rates for sodium ($A_{\mathrm{Na}} \approx 23$) and iodine ($A_{\mathrm{I}} \approx 127$) only targets are shown as dashed lines scaled by their respective mass fraction in the composite target. The most pronounced difference between the two spectra is the fact, that the rate for the heavy mediator is four orders lower than the rate for the light mediator. This behaviour is explained by the inverse proportionality of the differential cross section to the mediator mass to the fourth for both light and heavy mediator case. Moreover, for both heavy and light mediator case the differential rate for iodine is falling off faster than the rate for sodium. This is due to the form factor which is suppressing the rate for heavy target nuclei at higher recoil energies (compare also with Figure 2.3). In both cases the composite NaI target spectrum is thus dominated by the heavier iodine component within the first 10 keV of recoil energy, while for higher recoil energies the spectrum is governed by the light sodium component.

In addition to the features described above and the overall exponentially falling behaviour, there are a few more differences between the heavy and light mediator case. To start with, the spectrum for interaction via a light mediator is overall more steeply falling than the heavy mediator case. There is a notable difference in the slope of the spectra from interactions via a light and a heavy mediator, especially within the first few keV of recoil energy. The impact of the mediator mass on the

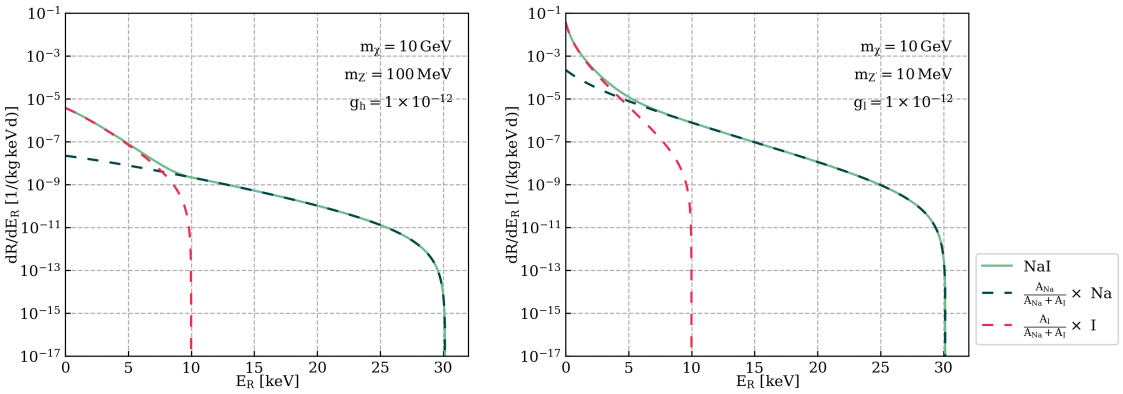

Figure 2.4: The nuclear recoil rate for interaction via a heavy (left panel) and light (right panel) vector mediator on a sodium iodide target. The spectra for sodium and iodine scaled to their respective fraction in NaI are shown as dashed lines. The heavy mediator mass is set to 100 MeV, the light mediator mass to 10 MeV and the DM particle has a mass of 10 GeV. No detector threshold or resolution was set.

spectrum is thus stronger for the part dominated by iodine. This is expected due to the additional dependence on the momentum transfer $q = \sqrt{2m_N E_R}$ in the light mediator case. However, also at higher energies in the sodium dominated part, the spectrum for the heavy mediator is relatively flat (in the log-log scale) up to almost 30 keV, while for the light mediator the slope is much steeper. Another characteristic by which the two spectra can be distinguished is that in the heavy mediator case the transition from iodine to sodium is clearly marked by a kink in the spectrum. For the light mediator case this characteristic is not as pronounced. The above described features also occur in the spectra of other composite and pure targets. However, for some composite targets the transition from one material to the other might not be marked by such a distinctive feature in the spectrum as just seen for sodium iodide. For example for sapphire (Al_3O_2) targets as used as one out of many targets by the CRESST [70] group, there will not be a pronounce transition feature due to the similar molecular masses of aluminium ($A_{\mathrm{Al}} \approx 27$) and oxygen ($A_{\mathrm{O}} \approx 16$).

Besides the dependence on the mediator mass, the shape of the recoil spectra is also governed by the mass of the DM particle. In Figure 2.5 the nuclear recoil rate on a NaI target is shown for various DM masses for both interaction via a heavy (magenta line) and light mediator (green line). The coupling for the heavy mediator is set to 100 times the coupling of the light mediator to achieve comparable rates at low recoil energies. The most apparent feature is that for smaller DM particle masses the differential recoil spectrum goes to zero at lower recoil energies. This behaviour arises from the DM mass dependence in the DM velocity distribution

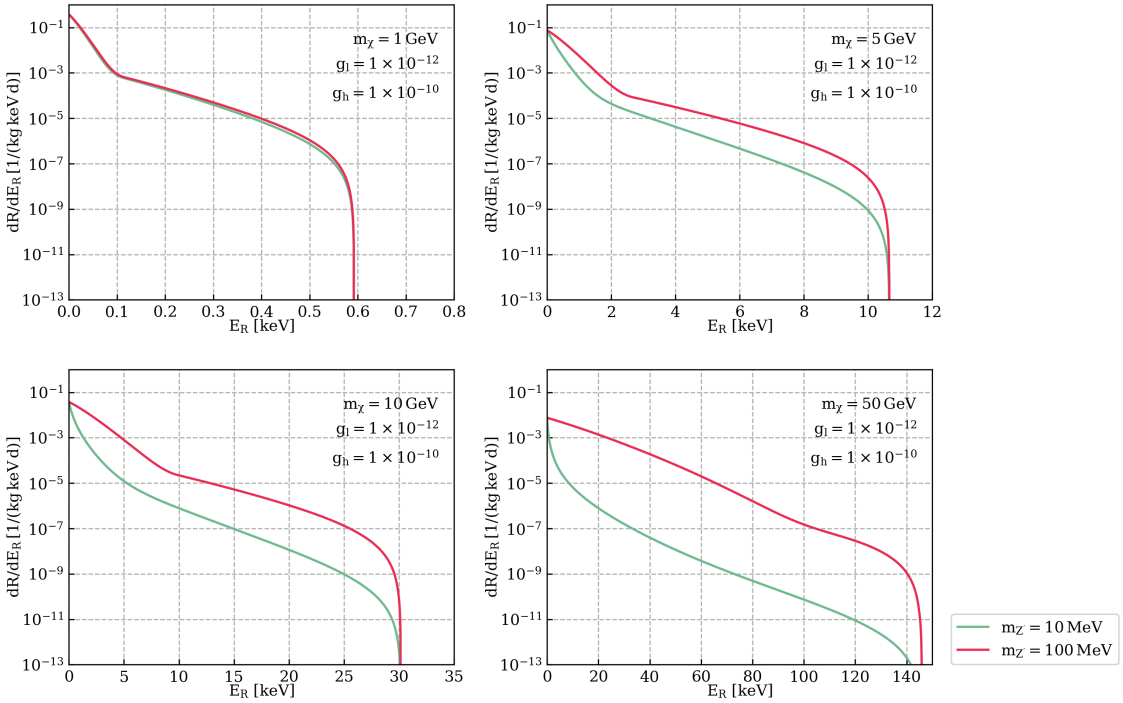

Figure 2.5: The NRS for interaction via a heavy (magenta line) and light (green line) vector mediator on a sodium iodide target for various DM masses. The light mediator mass is set to 10 MeV, the mass of the heavy mediator to 100 MeV. No detector threshold or resolution was set.

which goes to zero faster for smaller masses. In the bottom right panel, the kink in the spectrum for the heavy mediator case is not only affected by the change in target, but also by the dip appearing in the form factor for iodine at around 110 keV (compare with Figure 2.3). For DM masses even higher than 50 GeV, the impact of the shape of the form factor at higher recoil energies has to be taken more and more into account. Since the recoil rate is proportional to the inverse of the DM mass, the overall rate is higher for lower values of m_χ. Another important thing to note is, that for light DM particles (upper left panel) a mediator of mass 10 MeV behaves like a heavy mediator. It is thus important to also take the ratio of DM mass and mediator mass into account when speaking of a light or heavy mediator case. On the contrary, for a heavy DM mass, as in the lower right panel of Figure 2.5, the light mediator case deviates greatly from the heavy mediator case.

In the above we have seen that the type and mass of the mediator do have significant impact on the shape and magnitude of the differential recoil spectrum. For low recoil energies models with light mediator particles can lead to a much higher rate than the according heavy mediator model for the same coupling. Especially for experiments which are sensitive to low recoil energies, it is thus important to also

consider DM-SM scattering models with contact interaction. In the next section we will now discuss models where both light and heavy particles mediate the DM-quark interaction.

2.2 Bi-portal models

In this section a new simplified model for DM-SM scattering is introduced in which the interaction takes place via two t-channel mediators. Two mediator (bi-portal) models have been previously studied, for example for two Higgs-like scalar mediators in [13] and for a scalar together with a vector mediator in [11]. This work treats the combination of scalar and a vector mediator as well as interactions mediated by two vector mediators. It will be shown, however, that for the full analysis it suffices to restrict oneself to the two vector mediator DM model. A model with two spin-1 mediators has also previously been analysed in the recent work by Liu et al. [12], though only in the context of DM annihilation through the s-channel. Investigating a bi-portal model with at least one spin-1 mediator in the context of DM direct detection is thus a somewhat new approach. Since all following calculations are done in the foreground of direct detection experiments, it is again valid to use an EFT approach for heavy mediators and a simplified model for a light mediator with the appropriate low-energy degrees of freedom. In fact many of the concepts established above for the single portal can be reused.

Another feature of the bi-portal model in this work is that one mediator mass is chosen to lie in the contact interaction regime $m_{\phi'}^2 \gg q^2$, while the other mediator has a significantly lower mass $m_{\phi'}^2 \leq q^2$ resulting in long range interaction. Different masses for the two mediators have also been assumed in [11–13], however, never considering such a pronounced mass hierarchy.

2.2.1 Vector-Vector

We start with analyzing a model where the DM particle couples to the SM quarks via two dark sector vector mediators (vv-model): Z'_h with mass $m_{Z'_h}$ and a lighter Z'_l with mass $m_{Z'_l}$. With the interaction taking place via a t-channel exchange the according Feynman diagram is displayed in Figure 2.6. Under the assumption that these two mediators do not couple to each other, the relevant terms in the Lagrangian are:

$$\mathcal{L} \supset g_{Ql}\, Z'_l \bar{Q}\gamma^\mu Q + g_{\chi l}\, Z'_l \bar{\chi}\gamma^\mu \chi + g_{Qh}\, Z'_h \bar{Q}\gamma^\mu Q + g_{\chi h}\, Z'_h \bar{\chi}\gamma^\mu \chi \tag{2.45}$$

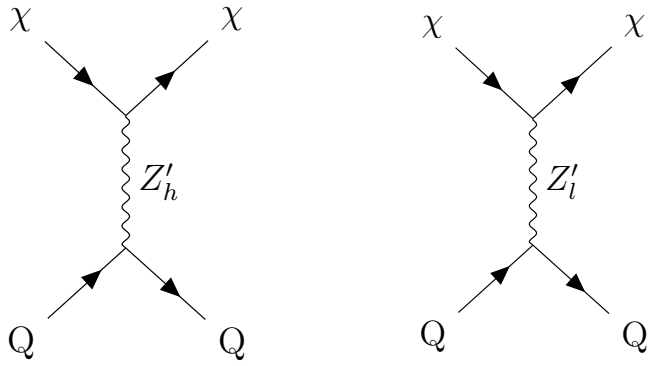

Figure 2.6: Feynman diagram at tree level for the DM-quark scattering in the t-channel via two vector mediators.

Considering this Lagrangian, also the matrix element for the interaction is simply given by the sum of the matrix element for the heavy mediator $\mathcal{M}_{Z'_h}$ and the matrix element for the light mediator $\mathcal{M}_{Z'_l}$. Those matrix elements at tree level are given by (2.28) with the respective choice of the mediator propagator $G(m_{Z'}, q)$. Making the assumption that quarks couple universally to both the light and the heavy Z', one can redefine overall coupling constants $\tilde{g_h} := g_{uh} = g_{dh}$ and $g_l := g_{ul} = g_{dl}$ respectively. The cross section for the vv-model is then

$$\mathcal{M}_{\text{vv}} = 4m_\chi m_N \left[\frac{\tilde{g_h}}{m^2_{Z'_h}} 3A + \frac{g_l}{m^2_{Z'_l} + q^2} 3A \right] F(q). \tag{2.46}$$

An interesting feature of the bi-portal model becomes apparent when squaring the matrix element, since this leads to an interference between the contributions from the heavy and from the light mediator:

$$|\mathcal{M}_{\text{vv}}|^2 = 16 m^2_\chi m^2_N (3A)^2 \left[\frac{\tilde{g_h}^2}{m^4_{Z'_h}} + 2\frac{\tilde{g_h} g_l}{m^2_{Z'_h}(m^2_{Z'_l} + q^2)} + \frac{g_l^2}{(m^2_{Z'_l} + q^2)^2} \right] F^2(q) \tag{2.47}$$

In the above squared matrix elements one can see, that the mass of the heavy mediator and $\tilde{g_h}$ only every appear together. It is thus sensible to define an effective coupling $g_h := \frac{\tilde{g_h}}{m^2_{Z'_h}}$, as we are only sensitive to the ratio of coupling and mass. This effective coupling is then of inverse mass dimension squared (usually given in MeV^{-2}). Depending on the signs of the overall coupling constants g_h and g_l, one has to differentiate between a constructive interference case for $g_h g_l > 0$ and a destructive interference case for $g_h g_l < 0$.

Having calculated the squared matrix element for the bi-portal model with two vector mediators, the framework established in sections 2.1.3 and 2.1.4 can now

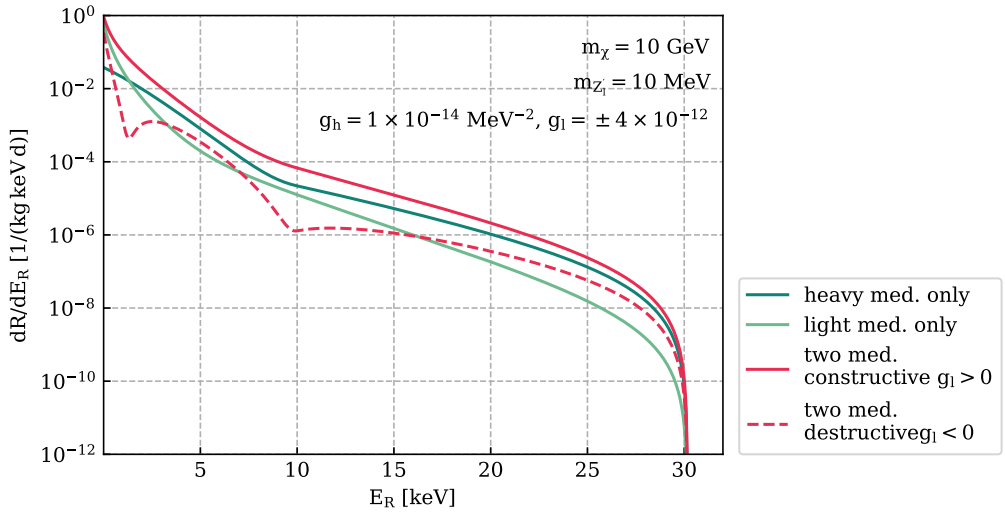

Figure 2.7: The nuclear recoil rate for interaction via a heavy (blue line) and light (green line) vector mediator, as well as for the bi-portal model (magenta line) on a sodium iodide target. The constructive case is shown as a solid magenta line, the destructive case a dashed magenta line. The light mediator mass is set to 10 MeV and the DM particle has a mass of 10 GeV. No detector threshold or resolution was set.

be applied to calculate the cross section and subsequently NRS for this model. In Figure 2.7 the nuclear spectra of a bi-portal mediator model, both in the case of destructive and constructive interference, are shown together with the spectra for a single heavy and a single light mediator. The effective coupling g_h is set to $1 \times 10^{-14}\,\mathrm{MeV}^{-2}$ and $g_l = \pm 4 \times 10^{-12}$ (this specific choice of coupling will become clearer later on). The mass of the DM particle is $m_\chi = 10\,\mathrm{GeV}$ and the mass of the light mediator is again $m_{Z_l'} = 10\,\mathrm{MeV}$. This composition of masses for the DM particle and Z_l', as well as the specific value for the effective coupling of the heavy mediator will be used many times throughout this work and will thus also be referred to as the benchmark model. Already on first glance it is clear that the bi-portal model (in magenta) is distinguishable from the single mediator models, both for the constructive and the destructive interference case. As expected, for the constructive case, the bi-portal model predicts a higher rate than both single portal models. The overall shape of the spectrum is a mixture of the shape of the two single mediator cases, but not in a strictly additive way due to the interference term. The kink characteristic for sodium iodide, where the target dependence shifts from Na to I is visible in the spectrum of the constructive bi-portal model, but not as pronounced as for the single heavy mediator.

Even more distinguishable spectra are achieved for the destructive interference case. Here, close approaches or crossings of the two single portal spectra result in

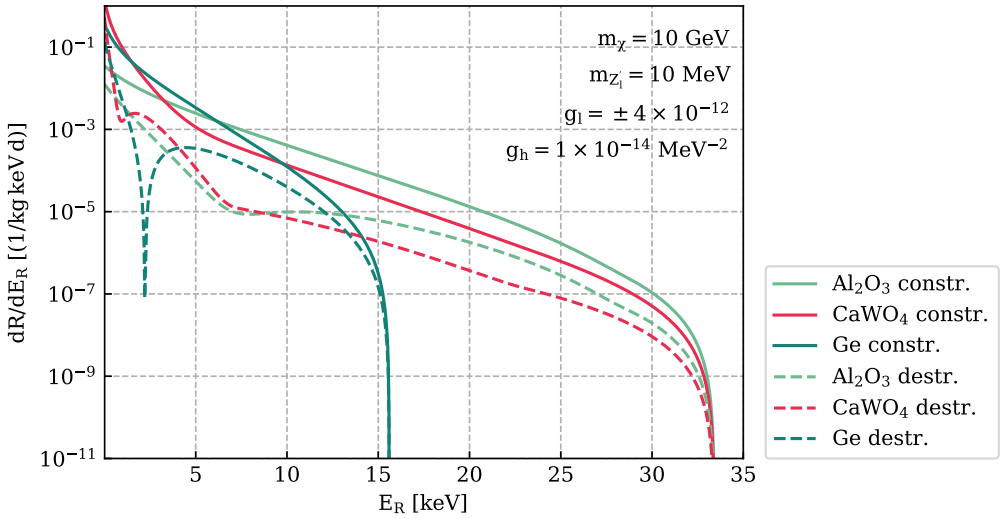

Figure 2.8: The nuclear recoil rate for the bi-portal model on calcium tungstate (magenta lines), sapphire (green lines) and germanium (blue lines) targets. Constructive cases are shown as solid, destructive as dashed lines. The light mediator mass to 10 MeV and the DM particle has a mass of 10 GeV. No detector threshold or resolution was set.

prominent features like dips and kinks. For the chosen combination of g_l and g_h these interference characteristics are clearly visible (in the dashed magenta spectrum) at around 2 and 10 keV. There is thus one destructive characteristic in the iodine dominated and one in the sodium dominate part of the spectrum. As said above, for these destructive interference effects to appear, the rate for single heavy and single light mediator need to be close together and/or overlap. Therefore, striking destructive features will only appear for a narrow range of combinations of g_l and g_h.

The interference effects seen for NaI are also present for other composite and pure target materials. In Figure 2.8 nuclear recoil spectra for the bi-portal model are shown for calcium tungstate (magenta lines), sapphire (green lines) and germanium (blue lines) targets. For all three targets the constructive case (solid lines) shows spectra which resemble the expected mixture between single heavy and light mediator case. For calcium tungstate there is a slight kink in the constructive spectrum, when the target dependence changes from tungsten ($A_\mathrm{W} \approx 184$) to calcium ($A_\mathrm{Ca} \approx 40$). The transition from calcium to oxygen which takes place around 23 keV is not visible due to the similar respective atomic masses of Ca and O_4 in calcium tungstate. This is also the reason why there is not visible kink in the constructive spectrum of Al_2O_3. In the destructive case interference effects are visible for all three targets. For $CaWO_4$ there is one interference dip in the tungsten dominated

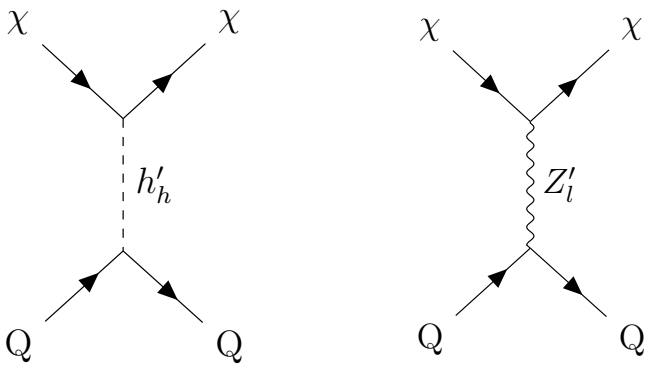

Figure 2.9: Feynman diagram at tree level for the DM-quark scattering in the t-channel via one heavy scalar and one light vector mediator.

regime, one in the calcium dominated one and a very indistinct feature at around 24 keV (oxygen dominated regime). For sapphire the spectrum shows one clear kink around 6 keV and another faint feature at around 27 keV. Interestingly there is also a prominent interference dip visible for the pure germanium target. A composite target and a change in target dependence is thus not required to achieve destructive interference effects in the spectrum. Notwithstanding that interference effects are visible for all shown target materials, the spectra still differ between the individual materials. Especially in the destructive case, the differences in shape and position of the interference characteristics can lead to discrepancies in the measured rates of experiments with different materials. These differences are more pronounced for the bi-portal model, than if a single mediator interaction is assumed. Since inconsistencies between the results of different experiments with varying targets are observed [9], this is a promising quality of the bi-portal model.

2.2.2 Scalar-Vector

Another possibility for a bi-portal model is that the DM particle couples to the SM quarks via one light vector mediator Z'_l with mass $m_{Z'_l}$ and one heavy scalar mediator h'_h with mass $m_{h'_h}$ (sv-model). With the interaction taking place via a t-channel exchange the according Feynman diagram is displayed in Figure 2.9. Assuming that the dark scalar does not give mass to Z' [3] the respective interaction terms in the Lagrangian are:

$$\mathcal{L} \supset g_{Ql}\, Z'_l \bar{Q}\gamma^\mu Q + g_{\chi l}\, Z'_l \bar{\chi}\gamma^\mu \chi + g_{Qh}\, h'_h \bar{Q}\gamma^\mu Q + g_{\chi h}\, h'_h \bar{\chi}\gamma^\mu \chi \tag{2.48}$$

[3] In [11] the dark Higgs breaks the additional $U(1)'$ symmetry giving mass to the Z' gauge boson.

As in the two vector mediator case the matrix element is given by the sum of (2.26) and (2.28) with the appropriate mediator propagators:

$$\mathcal{M}_{\mathrm{sv}} = 4 m_\chi m_N F(q) \times \left\{ \frac{1}{m_{h'_h}^2} [Z f_{p h'_h} + (A-Z) f_{n h'_h}] \right. \\ \left. + \frac{1}{m_{Z'_l}^2 + q^2} [Z(g_{ul} - g_{dl}) + A(2 g_{dl} + g_{ul})] \right\} \tag{2.49}$$

It is important to note, that the couplings $g_{\chi h}$ and g_{Qh} are absorbed in the definition of $f_{p h'_h}, f_{n h'_h}$. Assuming again, that Z'_l couples universally to all quarks, one defines again a dimensionless coupling constant $g_l := g_{ul} = g_{dl}$. For the scalar mediator a new variable $\vartheta := \arctan f_{n h'_h} / f_{p h'_h}$ is introduced, as in the single scalar case, and $g_h^2 := f_{n h'_h}^2 + f_{p h'_h}^2$. The overall squared matrix element thus reads

$$|\mathcal{M}_{\mathrm{sv}}|^2 = 16 m_\chi^2 m_N^2 F^2(q) \times \left\{ \frac{g_h^2}{m_{h'_h}^4} [Z \cos\vartheta + (A-Z)\sin\vartheta]^2 \right. \\ + 2 \frac{g_h g_l}{m_{h'_h}^2 (q^2 + m_{Z'}^2)} 3A [Z \cos\vartheta + (A-Z)\sin\vartheta] \\ \left. + \frac{g_l^2}{(q^2 + m_{Z'_l}^2)^2} (3A)^2 \right\}, \tag{2.50}$$

containing again an interference term which can result in either constructive or destructive behaviour depending on the signs of the couplings g_h and g_l. In order to derive the differential recoil rate from the above matrix element one can again follow the steps in sections 2.1.3 and 2.1.4 In the sv-model one has the additional free parameter ϑ, the value of which has an impact on whether the differential rate depends on the atomic number Z. In Figure 2.10 the nuclear recoil rate is shown for the benchmark model masses ($m_\chi = 10\,\mathrm{GeV}$, $m_{Z'_l} = 10\,\mathrm{MeV}$) and a fixed positive light vector mediator coupling $g_l = 4 \times 10^{-12}$ for three different values of ϑ. For each ϑ both constructive and destructive spectra are shown for two different values of $|g_h|$, one leading to visible interference effects in all panels and one representing a single light mediator limiting case. In the top left panel the rate for $\vartheta = 0$ is shown, corresponding to $f_{n h'_h} = 0$ or $f_{p h'_h} \gg f_{n h'_h}$. In this case the matrix element only depends on Z but not on the mass number A. The rates for both values of g_h are comparable to the bottom left panel in which $\vartheta = 1/2\,\pi$, i.e. $f_{p h'_h} = 0$ or $f_{n h'_h} \gg f_{p h'_h}$. For $\vartheta = 1/2\,\pi$ the matrix element depends on a factor of $(A-Z)$ and for the same value of g_l the difference between top left and bottom right panel is thus only governed by a factor of $Z/(A-Z)$.

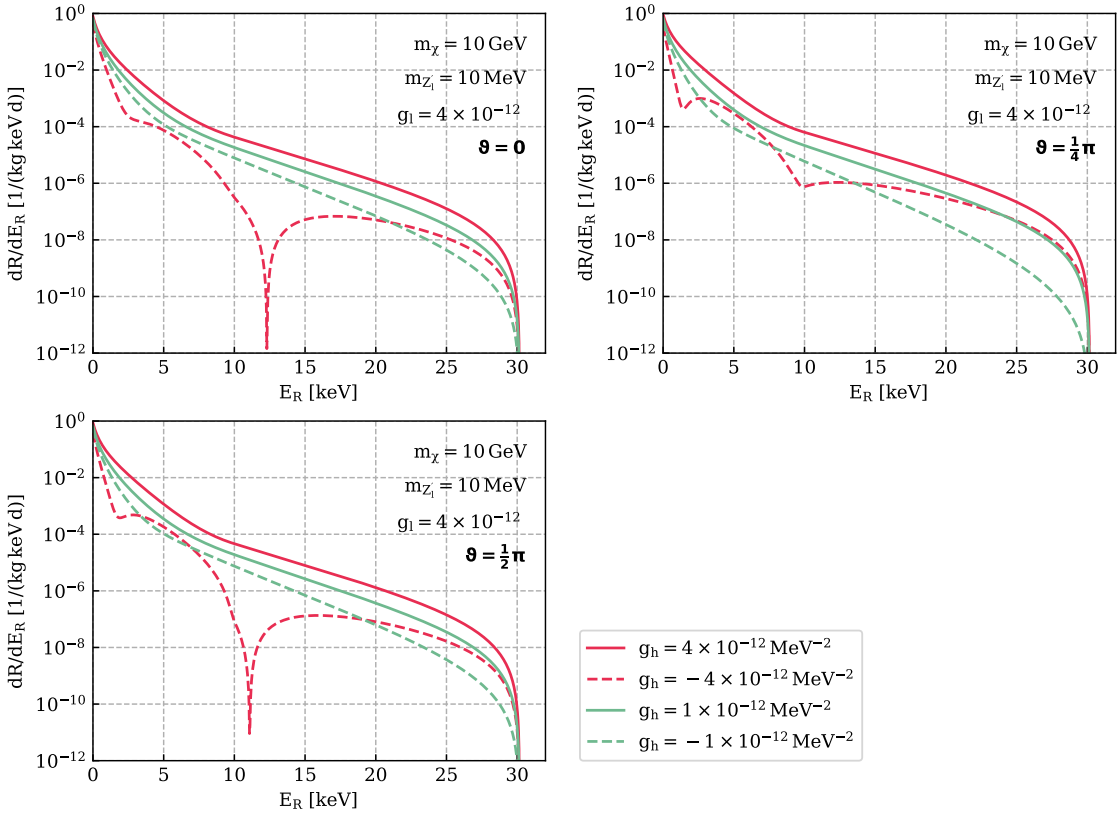

Figure 2.10: Nuclear recoil rate for interaction via a heavy scalar mediator and a light vector mediator. Different panels show the rates for different values of $\vartheta = f_n/f_p$ as defined via equation (2.50). The DM mass is set to 10 GeV, the light mediator mass to 10 MeV and for the heavy mediator an effective coupling is used. No detector threshold or resolution was set.

In the widely-used case where $f_{nh'_h} = f_{ph'_h}$, and thus $\theta = \pi/4$, the Z dependence vanishes ($\cos(\pi/4) = \sin(\pi/4)$) and the matrix elements for the scalar-vector and vector-vector case are identical up to some factors which can be absorbed in the definition of g_h. Indeed, the nuclear recoil rate for a heavy coupling of $g_h = \pm 4 \times 10^{-14}\,\mathrm{MeV}^{-2}$ in the top right panel of Figure 2.10 is comparable to a rate for $g_h = \pm 1 \times 10^{-14}\,\mathrm{MeV}^{-2}$ in the vv-model with all other parameters equal (compare with Figure 2.7). One can thus deduce that the conversion factor between vv- and sv-model ($\vartheta = 1/4\pi$) is around 4, more precisely

$$g_{h,\mathrm{sv}} = 3\sqrt{2} \times g_{h,\mathrm{vv}}, \tag{2.51}$$

if all other free parameters of the model are set to equal values. This relation is also illustrated in Figure 2.11.

-

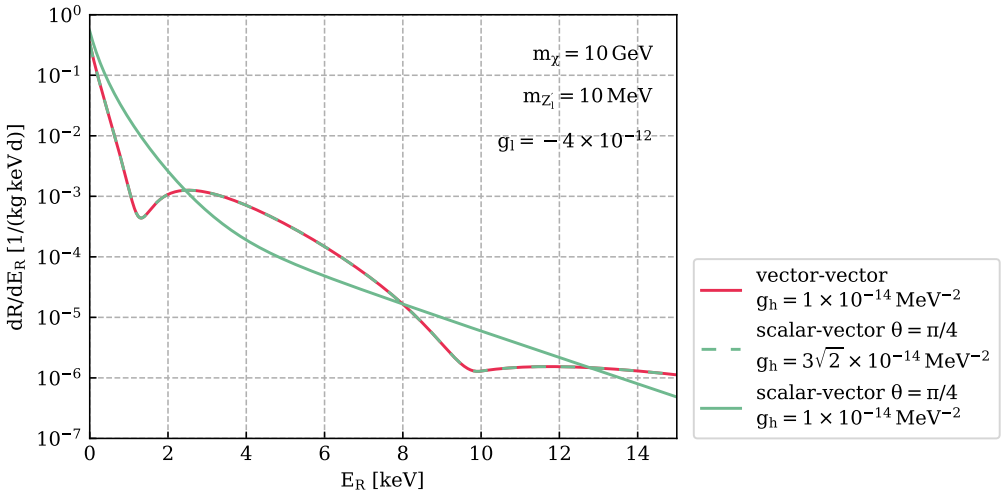

Figure 2.11: The nuclear recoil rate for vector-vector (magenta) and scalar-vector (green) destructive bi-portal models on sodium iodide. The light mediator mass is set to 10 MeV and the DM particle has a mass of 10 GeV. Only a part of the full available recoil energy range is shown and no detector threshold or resolution was set.

In this chapter the particle physics foundation for the bi-portal model has been laid and a first insight on its effect on the differential event rate has been given. Having shown that up to scaling factors in g_h the vector-vector and scalar-vector model ($\vartheta = 1/4\pi$) yield identical spectra, we can limit ourselves to the vector-vector interaction in the further analysis of the model. In the next chapter both the constructive as well as the destructive interference case are analysed in more detail with respect to the four free parameters of the model: the DM mass m_χ, the light mediator mass $m_{Z_l'}$, the coupling of the light mediator g_l and the effective coupling for the heavy mediator g_h.

Chapter 3

Analysis of the bi-portal model

In the following the the bi-portal model, as derived in the previous chapter, and especially the according (differential) recoil rates are further analysed. Abstracting away from uncertainties in cosmological input parameters (i.e. DM density, Earth's velocity, etc.), the bi-portal model has four free parameters: the DM mass m_χ, the light mediator mass $m_{Z_l'}$, the overall dimensionless coupling constant for the light vector mediator g_l and the effective coupling g_h for the heavy vector mediator. The following analysis will first focus on the constructive interference case of the bi-portal model and then on the destructive interference case. In the subsequent sections the number of total events which the bi-portal model predicts is analysed, also with regard to the energy threshold of an experiment. Finally another detector specific quantity, the energy resolution, is introduced and its impact on the predicted differential rate is analysed. Within this whole chapter a sodium iodide target is used in the calculation of differential recoil spectra and total event rates. NaI is a most suitable target to analyse the bi-portal model, due to the large difference in the mass numbers of sodium and iodine. This difference can lead to strong interference characteristics at recoil energies where a change in target dependence takes place.

3.1 Constructive interference case

To begin with, the constructive interference case, hence the case where $g_l \times g_h$ is positive, is analysed. As seen in Figure 2.7 the effects of the interference term are more subtle for the constructive compared to the destructive case, but still considerable. To analyse the constructive bi-portal model, the behaviour of the nuclear recoil spectra under variation of the four free parameters is studied.

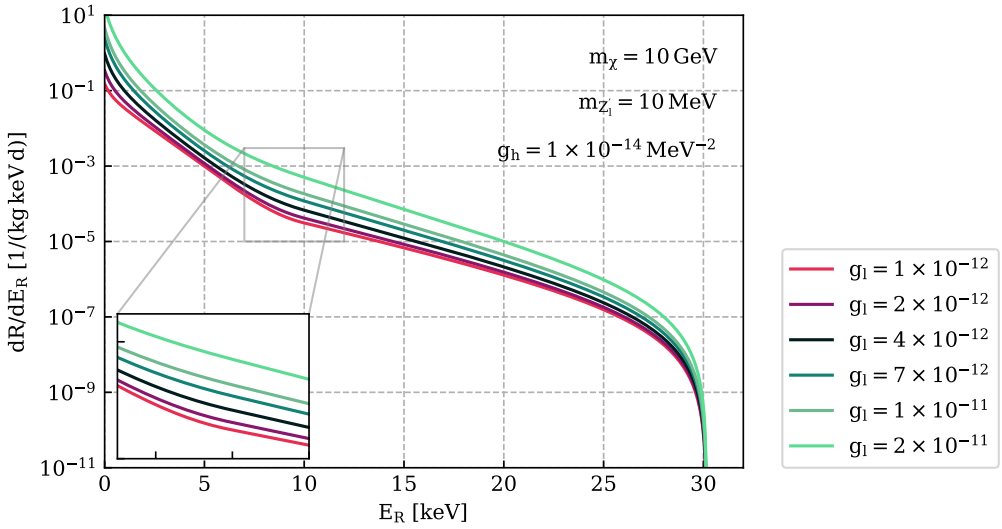

Figure 3.1: The nuclear recoil rate for a bi-portal constructive model on sodium iodide. The DM mass $m_\chi = 10\,\mathrm{GeV}$, the light mediator mass $m_{Z_l'} = 10\,\mathrm{MeV}$ and the effective coupling of the heavy mediator are fixed and spectra are shown for various values of g_l. No detector threshold or resolution was set.

In a first step three out of the four free parameters are fixed according to the previously mentioned benchmark model: the mass of the Dirac DM particle to 10 GeV, the mass of the light mediator to 10 MeV and the effective coupling of the heavy mediator to $g_h = 1 \times 10^{-14}\,\mathrm{MeV}^{-2}$ (this corresponds e.q. to a dimensionless coupling of 1×10^{-10} and a mediator mass of 100 MeV). In Figure 3.1 the spectrum is then shown for various values of g_l ranging from 1×10^{-12} to 2×10^{-11}. For the lowest value of g_l in this range (magenta line in Figure 3.1) the interaction via the heavy mediator is dominating the recoil process. The spectrum thus resembles one resulting from a single heavy vector mediator exchange. The preciously mentioned characteristics for this kind of interaction include the overall flatter slope and the more pronounced kink where the target dependence changes from iodine to sodium at around 10 keV recoil energy. On the contrary, for higher values of g_l the light mediator dominates the interaction and the spectrum thus mirrors the one for a single light mediator exchange (neon green line). Thus, only within a limited span of values for g_l, the bi-portal mediator model gives differential event rates with distinct shapes from the single portal cases. Using values for the light mediator coupling lower or higher than the ones shown in Figure 3.1 will result in spectra representing one of these two single mediator limiting cases of the bi-portal model. Alternatively, one could also fix the light mediator coupling and study spectra for various values of g_h. Choosing the couplings accordingly will result in plots similar

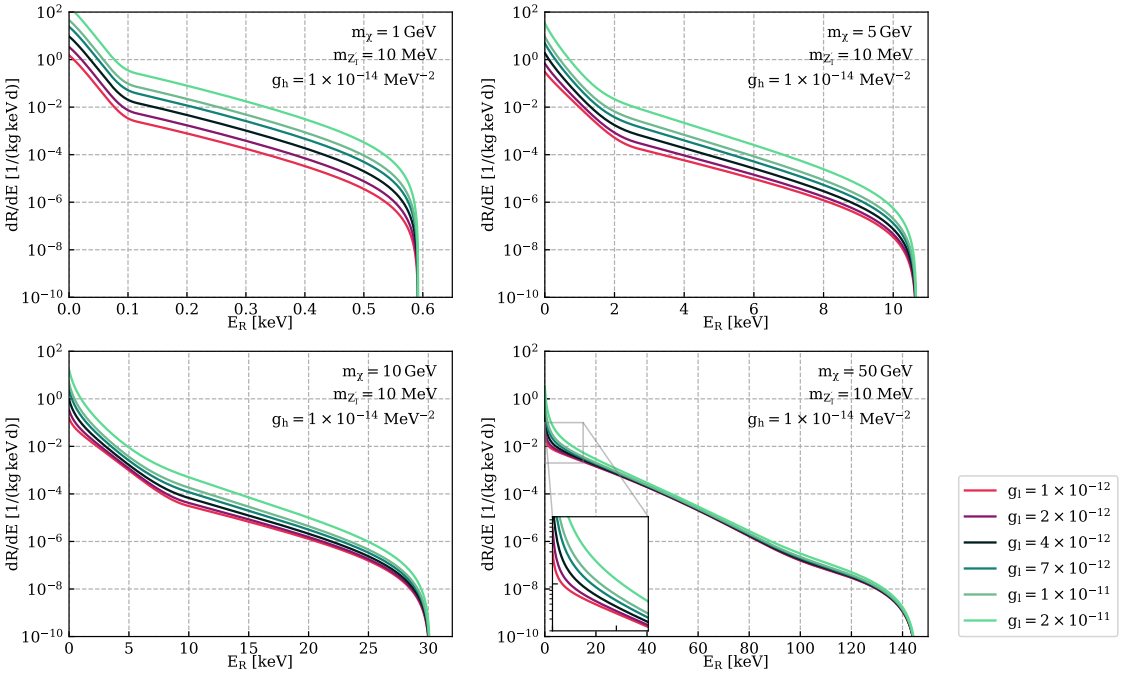

Figure 3.2: The nuclear recoil rate for a bi-portal constructive model on a sodium iodide target. The light mediator mass $m_{Z_l'} = 10\,\mathrm{MeV}$ and the effective coupling of the heavy mediator are fixed. In the four panels spectra are shown for four different DM masses and various values of g_l. No detector threshold or resolution was set.

to Figure 3.1 and the variation of the couplings is thus not discussed further. One should however make a note of the specific set of light mediator couplings used in Figure 3.1 and the according shapes of the differential recoil spectra, as this set will be reused often within the rest of this chapter.

In a next step, the spectra for four different DM masses $m_\chi = 1,\ 5,\ 10,\ 50\,\mathrm{GeV}$ are studied. All other free parameters are chosen according to the benchmark model and the set of values for g_l given above is used. As seen in Figure 2.5 for the single mediator interaction, Figure 3.2 shows that lower DM masses lead to a lower maximum recoil energy at which the nuclear recoil spectra break off. The upper left panel of Figure 3.2 shows spectra for the lightest choice of DM. As seen before in the single mediator case, for a DM particle of mass $m_\chi = 1\,\mathrm{GeV}$ a light mediator of mass 10 MeV behaves like a heavy mediator. This is apparent from the pronounced kink in the spectrum at around 0.1 keV. Independent of the value of g_l within the given range all spectra thus represent the limiting case of a single heavy mediator scaled accordingly to the value of the coupling. Increasing the mass of the DM particle compared to the lightest case results in spectra of varied shape for each coupling (upper right and lower left panel). Limiting cases are visible for higher and lower values in the set of g_l values, as already discussed for Figure 3.1 above. In the lower

right panel the DM mass is set to 50 GeV. For the heavy DM particle the individual spectra lie closer together, due to inverse DM mass dependence somewhat weakening the impact of g_l on the scaling of the spectra. However, zooming in, one can see that there is still a variation in the shape of the spectra consistent with the limit cases discussed above.

There is one free parameter whose impact on the nuclear recoil rate is left to analyse, the mass of the light mediator. Analysis of various light mediator masses showed, that values for $m_{Z'_l}$ lower than 10 MeV have only very little to no impact on the shape of the recoil spectrum. Especially for mediator masses in the order of 0.1 MeV or lighter, the momentum transfer in the denominator of the cross section becomes the governing quantity in the spectrum and the mediator mass dependence thus vanishes. However, if the mass of the light mediator is chosen too high in comparison to the DM mass, the interaction will behave like one via two heavy mediators and interference effects become evanescent.

3.2 Destructive interference case

While the constructive interference case already leads to novel features in the spectra, the destructive case is even more interesting to analyse. The interference effects (dips and kinks) seen in Figure 2.7 and Figure 2.8 cannot be achieved by a single mediator model and are thus unique to the bi-portal model. To achieve a thorough examination of the model, the impact of variation of the four free parameters on the nuclear recoil spectrum is examined, as it was done in the previous section for the constructive case. The previously established benchmark model for masses and effective coupling is also used for the destructive case, as well as the set of values for the light mediator coupling, however, now with a preceding minus sign.

For various values of the light coupling, ranging from -1×10^{-12} to -2×10^{-11}, spectra are shown in Figure 3.3. For the lowest absolute value of $|g_l|$ shown (magenta line) the interaction via the heavy mediator is dominating the recoil process. As in the constructive case, the spectrum thus resembles one of an interaction taking place via single heavy mediator. However, at very low recoil energies, the spectrum behaves differently from the single mediator case: a dip is created, due to the intersection of the single heavy and single light mediator rate at a recoil energy close to zero. This assumption is reinforced by the behaviour of the spectrum for $g_l = -2 \times 10^{-12}$ where one sees an interference dip close to $E_R = 0$. Increasing the absolute value of $|g_l|$, and thus the influence of the light mediator within the

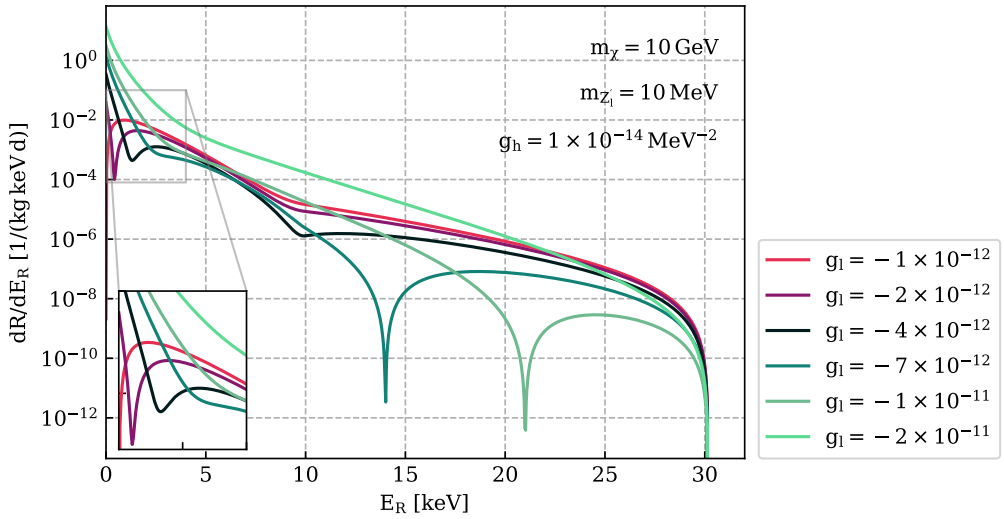

Figure 3.3: The nuclear recoil rate for a bi-portal destructive model on sodium iodide. The DM mass $m_\chi = 10\,\mathrm{GeV}$, the light mediator mass $m_{Z_l'} = 10\,\mathrm{MeV}$ and the effective coupling of the heavy mediator are fixed and spectra are shown for various values of g_l. No detector threshold or resolution was set.

interaction, leads to a displacement of this dip towards higher recoil energies. Additionally, for higher $|g_l|$ the dip becomes shallower until it disappears in the light mediator limit at $g_l = -2 \times 10^{-11}$. It is important to note that this first dip, as far as it exists, is always positioned in the iodine dominated region of the spectrum. For $|g_l| > 3 \times 10^{-12}$ a second destructive features starts to appear close to the recoil energy where the target dependence changes from iodine to sodium. Increasing $|g_l|$ further, leads again to a shift in the position of the dip towards higher recoil energies. In opposition to the dip in the iodine dominated area, the dip in the sodium dominated area gains in depth with decreasing g_l. For $g_l = -2 \times 10^{-11}$ the dip has merged with the vertical falling behavior of the spectrum at $E_R \approx 30$ keV. The disappearance of the dip is consistent with the expected behaviour of the single light mediator limiting case (neon green line). Hence, as in the constructive case, the bi-portal mediator model gives differential event rates with distinct interference effects only for a narrow range of values for g_l for a fixed heavy mediator coupling. Summing up, nuclear recoil spectra for the destructive bi-portal model on a NaI target can show up to two strong interference features for an appropriate choice of couplings. One should note here, that the appearance of one or several interference features is not specific to the sodium iodide target. In Figure 2.8 a single destructive dip was visible for the single element target Germanium and the destructive bi-portal spectrum for the other composite target, $CaWO_4$, also shows multiple interference features.

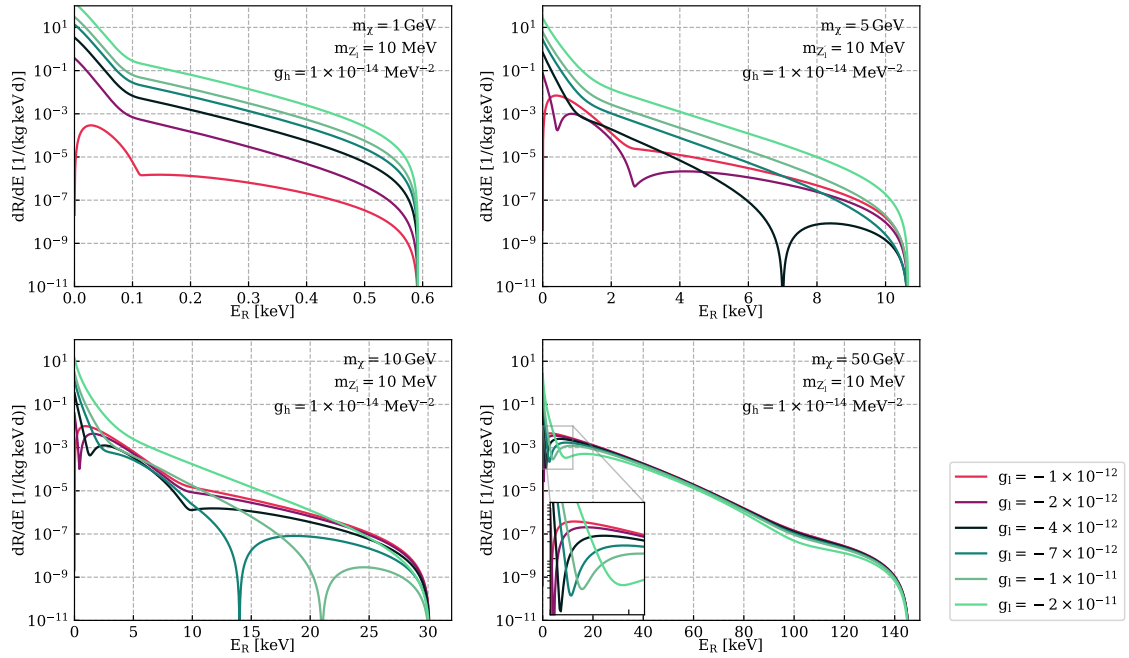

Figure 3.4: The nuclear recoil rate for a bi-portal destructive model on a sodium iodide target. The light mediator mass $m_{Z_l'} = 10\,\mathrm{MeV}$ and the effective coupling of the heavy mediator are fixed. In the four panels spectra are shown for four different DM masses and various values of g_l. No detector threshold or resolution was set.

In a next step the impact of the DM mass on the shape of the spectrum is investigated. The four panels of Figure 3.4 show spectra on sodium iodide in the destructive bi-portal model for the standard set of g_l values and DM masses $m_\chi =$ 1, 5, 10, 50 GeV. The mass of the light mediator and the coupling of the heavy mediator are fixed according to the benchmark model. The most apparent difference between the four panels is the recoil energy at which the spectrum goes to zero, which is decreasing with lighter DM particles. This behaviour was already observed in the single mediator and the constructive bi-portal case and is caused by the m_χ-dependence of the DM velocity distribution. In addition, the differential event rate is inversely proportional to the DM mass and the rate is thus overall lower for higher DM masses. In the upper left panel of Figure 3.4 the spectra are shown for a light DM particle of mass $m_\chi = 1$ GeV. For a broad range of couplings $g_l = -2 \times 10^{-11}$ to $g_l = -2 \times 10^{-12}$ the spectra all resemble the nuclear recoil spectra of an interaction governed by a single heavy mediator. This behaviour has been previously discussed for the constructive interference case and can be reasoned by the ratio of DM to light mediator mass. However, in the case of $g_l = -1 \times 10^{-12}$ and $m_\chi = 1$ GeV the differential event rate is overall lower and differs in shape from the other rates in the upper left panel of Figure 3.4. In order to understand this, one has to go back to

the upper left panel of Figure 2.5 in chapter 2. In this plot the spectra for a single light mediator with $m_{Z_l'} = 10$ MeV, $g_l = 1 \times 10^{-12}$ and a single heavy mediator with $m_{Z_h'} = 100$ MeV, $g_h = 1 \times 10^{-10}$ - hence an effective coupling of $g_h = 1 \times 10^{-14}\,\text{MeV}^{-2}$ - are shown for 1 GeV DM. The two spectra lie very close together, in fact at very low recoil energies where $q^2 \approx 0$ they are almost identical. Due to this similarity in the two rates, the negative interference term in the cross section formula has a strong impact on the whole spectrum, in particular it reduces the overall rate significantly. In addition, local effects appear where the impact of the interference term is strongest, namely close to $q^2 = 0$ and at the recoil energy where the target dependence changes from iodine to sodium. These arguments can fully explain the behaviour of the magenta line in the top left panel, as the change for iodine to sodium takes place at around 0.1 keV for a 1 GeV DM particle. For a slightly higher DM mass of 5 GeV in the upper right panel of Figure 3.4, one can again turn to Figure 2.5 in order to understand the behaviour of the rate for $g_l = -1 \times 10^{-12}$. In the upper right panel of Figure 2.5 the rates for single light and heavy mediator interaction are again quite similar. Nonetheless, strong interference effects only appear at recoil energies close to zero, where the rates lie closely together. The magenta line in the top right panel of Figure 3.4 thus only shows peculiar behaviour close to $E_R = 0$. Increasing the absolute value of g_l is identical to shifting the light mediator rate in Figure 2.5 upwards along the y-axis. For the couplings $g_l = -2 \times 10^{-12}$ and $g_l = -4 \times 10^{-12}$ this shift results in overlaps of the two single mediator spectra and thus striking interference effects in the destructive bi-portal spectrum. For even higher values of $|g_l|$, however, the light mediator rate outgrows the heavy mediator rate and thus no destructive features are generated. Consistent with the behaviour in the constructive interference case, for $|g_l| > 2 \times 10^{-11}$ the spectrum starts to adopt the shape of the single light mediator limiting case. The bottom left panel of Figure 3.4 shows again the benchmark model, whose features have already been discussed at length above. For a DM particle of mass 50 GeV the rates for various values of g_l are show in the bottom right panel. For the heavier DM the rates lie closer together for the same range of couplings as in the other panels, a feature which was also observed in the constructive case. Interestingly the order of the spectra is inverted, i.e. for the highest absolute value of g_l the rate is the lowest (green line). To understand this, it is again helpful to take a look at the according panel in Figure 2.5. Even tough the two single mediator rates have the same value at recoil energies close to zero, they soon start to diverge widely and the impact of the destructive interference term is thus very low. Increasing the absolute value of $|g_l|$

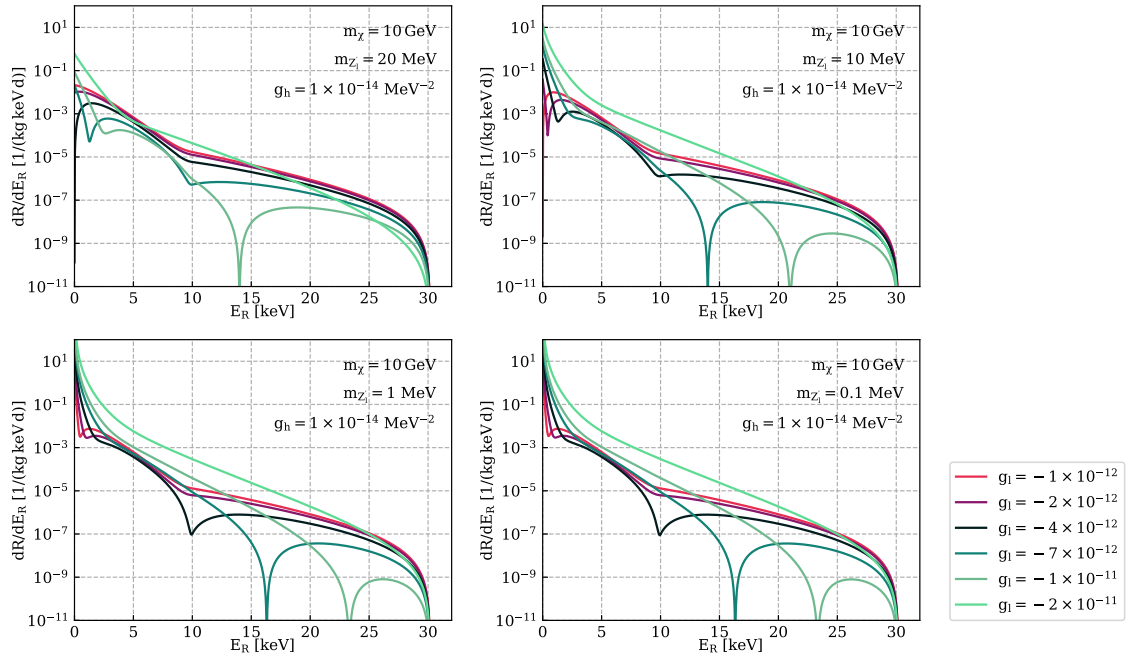

Figure 3.5: The nuclear recoil rate for a bi-portal destructive model on a sodium iodide target. The DM mass m_χ and g_h are fixed. In the four panels spectra are shown for four different light mediator masses $m_{Z_l'} = 20,\ 10,\ 1,\ 0.1$ MeV and a range of values for the light mediator coupling g_l. No detector threshold or resolution was set.

corresponds to moving the light mediator rate up along the y-axis and closer towards the heavy mediator rate. This leads to an increasing destructive interference term and hence an overall lower nuclear recoil rate in the bi-portal model. For high DM masses distinct destructive features as in the benchmark model start to appear for values of $|g_l| > 1 \times 10^{-11}$ for the shown choice of g_h. The single light mediator limit case only comes into effect for couplings $|g_l| > 1 \times 10^{-10}$.

In a last step of the analysis the impact of the mediator mass on the destructive two mediator model is being investigated. Nuclear recoil spectra are shown for four different light mediator masses in Figure 3.5. The, by now familiar, set of light mediator couplings is used and all other free parameters are fixed according to the benchmark model. Before analysing each panel individually one should remember, that the mass of the light mediator enters the bi-portal squared matrix element (2.47) proportional to $1/(m_{Z_l'}^2 + q^2)^2$ in the light mediator contribution and proportional to $1/(m_{Z_l'}^2 + q^2)$ in the interference term. This inverse proportionality leads to overall higher recoil rates for smaller mediator masses. In the upper left panel of Figure 3.5 the mediator mass is set to 20 MeV, which is double the mass of the light mediator in the benchmark model. One should note that, with a mass of 20 MeV the mediator is placed in a regime in which the transition from light to heavy

mediator classification takes place. However, $(20\,\mathrm{MeV})^2 \leq 2m_N E_R$ holds true for recoil energies over approximately 2 keV in the iodine dominated part and 10 keV in the sodium dominated part. Including the momentum transfer dependence is thus valid also in the case of a 20 MeV mediator. Nevertheless, the higher mediator mass compared to the benchmark model, reduces the light mediator contribution to the bi-portal matrix element. In other words $1/((20\,\mathrm{MeV})^2 + 2m_N E_R) < 1/((10\,\mathrm{MeV})^2 + 2m_N E_R)$. Thus for higher mass of the light mediator, the Z_l'-contribution to the bi-portal model is reduced. Especially in combination with low values of $|g_l|$ this can lead to interactions dominated by the heavy mediator. This behaviour can be observed in upper left panel of Figure 3.5 for couplings up to $g_l = -4 \times 10^{-12}$. For higher $|g_l|$ the light mediator gains influence and destructive features begin to appear. With a light mediator of mass 20 MeV, the limiting light mediator case is reached for $|g_l| \geq 8 \times 10^{-11}$. For even larger values of $m_{Z_l'}$ the bi-portal model just consists of two heavy mediators, resulting in no interference effects for both constructive and destructive case. Comparing the benchmark model in the top right panel with the two bottom panels does not lead to significant differences. For very small light mediator masses $m_{Z_l'} \leq 1$ MeV one reaches the limit $1/(m_{Z_l'}^2 + q^2) \rightarrow 1/q^2$ and the momentum transfer becomes the governing quantity in the denominator of light mediator contribution to the matrix element. There is thus no $m_{Z_l'}$ dependence left in the definition of the recoil spectrum and the rates for $m_{Z_l'} = 1$ MeV and $m_{Z_l'} = 0.1$ MeV are (almost) identical. Subtle differences between the spectra in the top right and the bottom panels can be seen for recoil energies close to zero. In this region the momentum transfer is very low and the a mediator mass of 10 MeV has significant influence on the expression $1/(m_{Z_l'}^2 + q^2)$. With increasing recoil energy the impact of $m_{Z_l'}$ decreases. However, the slight differences in position and depth of the destructive features in the top right compared to the bottom panels shows that the light mediator mass dependence cannot be neglected.

3.3 Total number of events

Besides the differential recoil spectrum the total number of expected events is an important model specific quantity in direct detection. Given a certain exposure ε ($[\varepsilon]$ = kg day or tonne year), the expected number of events N_{tot} gives a good first estimate of the ability of an experiment to observe any DM signal in the first place. The number of events is simply given by integrating the differential event rate over

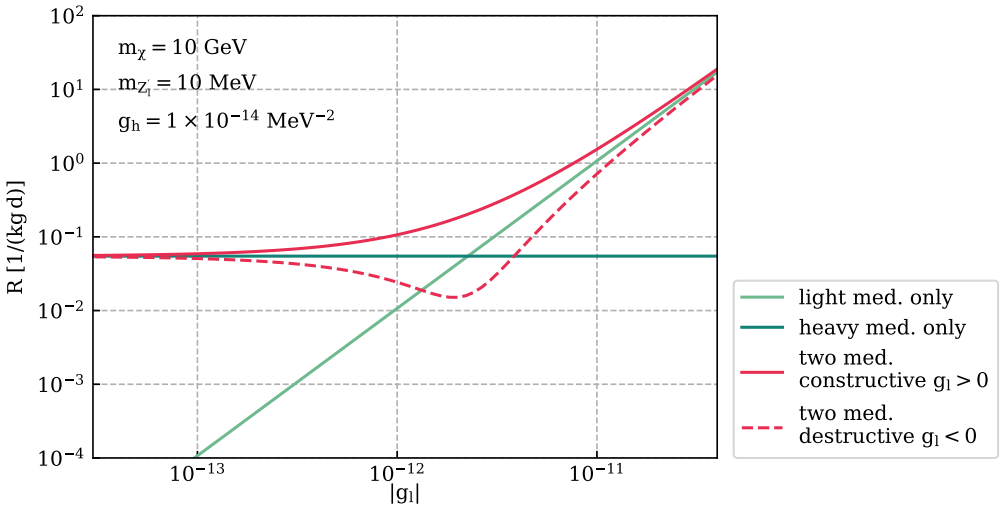

Figure 3.6: Rate of total events expected on a NaI target as a function of the light mediator coupling g_l. The dark matter mass is fixed at 10 GeV, the light mediator mass at 10 MeV and the effective coupling for the heavy mediator at $g_h = 1 \times 10^{-14}$. The rate of total events $R(g_l)$ is shown for the constructive (magenta solid) and destructive (magenta dashed) bi-portal model, for a single light mediator (green) and a single heavy mediator (blue). No detector threshold, resolution or exposure have been set.

the available space of recoil energies and multiplying by the exposure:

$$N_{\text{tot}} = \varepsilon R = \varepsilon \int_{E_{\text{thr}}}^{E_{\text{max}}} dE_R \frac{dR}{dE_R} \tag{3.1}$$

The limits of the integral are given by the detector specific threshold energy E_{thr} and the maximum recoil energy, i.e. the energy where the spectrum breaks of, which depends on the DM and the target mass. One should note that, although the integration is in principle carried out over the whole space of available energies, due to the overall exponentially falling recoil spectrum the number of total events is dominated by the shape of the spectrum within the first few keVs of recoil energy. For a sodium iodide target this implies that the total number of predicted events is mostly controlled by the recoils induced in the iodine component.

In Figure 3.6 the rate of total events expected from a bi-portal model for a sodium iodide target is shown as a function of the light mediator coupling g_l. No exposure was set and, for now, a zero threshold is assumed. All other free parameters, i.e. the DM mass, the light mediator mass and the heavy mediator effective coupling, are fixed to their respective values in the benchmark model. Besides for the constructive and destructive bi-portal case (magenta line) the function $R(g_l)$ is also shown for a single light mediator model with mediator mass $m_{Z'_l}$ and coupling g_l and a single

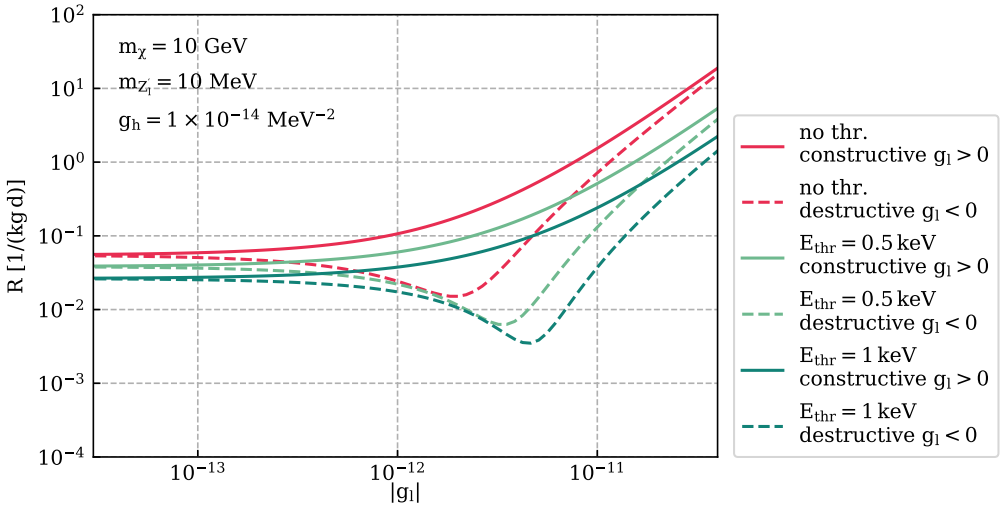

Figure 3.7: Rate of total events expected on a NaI target as a function of the light mediator coupling g_l. The dark matter mass is fixed at 10 GeV, the light mediator mass at 10 MeV and the effective coupling for the heavy mediator at $g_h = 1 \times 10^{-14}$. The rate of total events $R(g_l)$ is shown for the constructive (solid lines) and destructive (dashed lines) bi-portal model for various detector thresholds. No detector resolution or exposure have been set.

heavy mediator with effective coupling g_h. As the differential recoil rate for the heavy mediator does not depend on the g_l the respective graph is a horizontal line (in blue). In the case of the single light mediator the function $R(g_l)$ scales with g_l^2, resulting in a graph represented by a line of constant slope in the log-log scale. The constructive bi-portal model predicts, as expected, overall more events than the single mediator rates by themselves. For very low (high) values of g_l the function $R(g_l)$ approaches the single heavy (light) mediator limit. This is consistent with the behavior observed in the differential recoil rate. Also in the destructive interference case these limiting cases are present. As expected, the destructive bi-portal model predicts overall less events then both single mediator cases. For certain values of $-g_l$ between 1×10^{-12} and 1×10^{-11} the rate of total expected events is further reduced due to the destructive interference effects appearing in the differential event rate. As reasoned above, however only dips appearing within the iodine dominated recoil energy region have significant impact on the number of total events. Another important thing to note is that in the destructive bi-portal case $R(g_l)$ is not injective and thus a certain number of total events can be observed for more than one value of g_l for fixed g_h.

In Figure 3.7 the total event rate as a function of the light mediator coupling is again displayed for the constructive and destructive bi-portal model. However,

now the case of zero assumed threshold is compared to the case of a 0.5 keV and a 1 keV threshold. Introducing a threshold reduces the number of expected events significantly. This effect is even stronger for models in which the light mediator dominates the DM-SM interaction, as seen for higher values of g_l in Figure 3.7. This is due to the high but steeply falling recoil rates a light mediator model predicts for low recoil energies - for a high threshold this part of the spectrum may be cut off. The insensitivity to low recoil energies induced by a higher threshold may also result in the non-observance of destructive interference effects. In other words, interference dips appearing at energies lower than the threshold are not being considered. As seen in Figure 3.3, for fixed values of g_h the recoil energy at which an interference effect appears is related to the value of the light mediator coupling - for higher $|g_l|$ the dips move towards higher recoil energies. This effect can also be observed in Figure 3.7, where the minimum of the function $R(g_l)$ for the destructive case moves towards higher values of $|g_l|$ for higher thresholds. This shows, that low-threshold experiments are needed in order to be sensitive to the characteristics of the bi-portal model.

3.4 Impact of detector resolution

The aim of this work is not only to analyse the bi-portal model on a theoretical level, but especially to investigate it in the context of direct detection experiments. The nuclear recoil spectrum is a strong tool to do this, as it returns the predicted number of events as a function of the recoil energy - a measure which can be compared to experimental results. However, the situation in a real experiment is more complex and besides the target material many more detector-specific parameters need to be taken into account to achieve realistic results. Independent of the type of detector being used in a experiment to measure the recoil energies (photon, ionization, phonon detectors etc.), such a measurement is always subject to the energy resolution of the detector. For phonon signals the energy resolution can be described with a normal distribution of width σ in the large sample limit. The detector specific parameter σ is in general a function of the recoil energy [17, 71], but as a first estimate it is appropriate to assume constant σ. The detector specific energy resolution is then incorporated in the nuclear recoil spectrum via a convolution with a normal/Gaussian distribution [72]:

$$\frac{dR}{dE_R}_{res}(E_R) = \frac{1}{\sqrt{2\pi\sigma^2}} \int_0^\infty \frac{dR}{dE_R}(E'_R) \exp\left(-\frac{(E_R - E'_R)^2}{2\sigma^2}\right) dE'_R \tag{3.2}$$

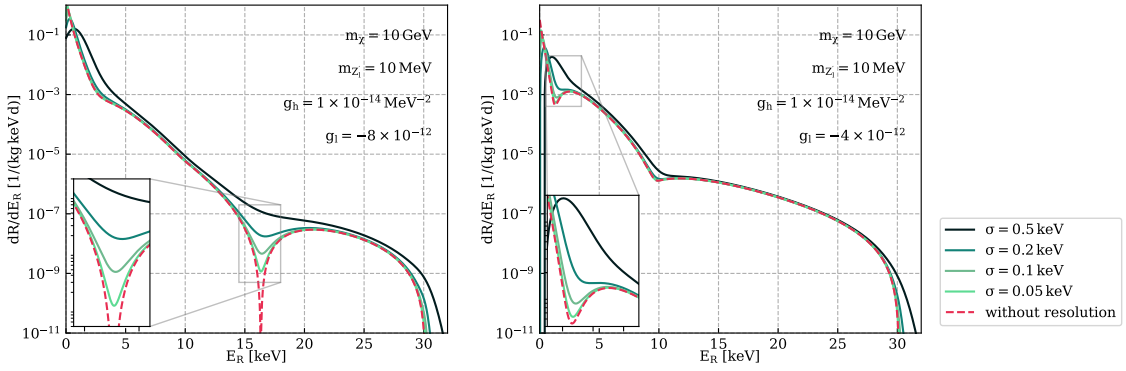

Figure 3.8: The nuclear recoil rate for a bi-portal destructive model on a sodium iodide target. The DM mass is $m_\chi = 10\,\mathrm{GeV}$, the light mediator mass $m_{Z_l'} = 10$ MeV and the effective coupling of the heavy mediator is fixed to $g_h = 1 \times 10^{-14}\,\mathrm{MeV}^{-2}$. The recoil spectrum is shown for various values of σ as a measure of detector resolution for a light mediator coupling of -8×10^{-12} in the left and -4×10^{-12} in the right panel. The magenta dashed line displays the rate without any assumed detector resolution.

Since the nuclear recoil rate goes to zero for a certain recoil energy $E_{\max}$ (e.g. around 31 keV for a 10 GeV DM particle on NaI), the positive infinity in the upper integration limit can be replaced by this maximum recoil energy $E_{\max}$ if the integration is done numerically. The convolution with the Gaussian distribution of finite width leads to a smoothing of the spectrum, including a flattening of the sharp fall-off at the end of the spectrum. One thus has to check if the interference effects seen in the spectra above do not disappear due to the detector resolution.

In Figure 3.8 the nuclear recoil spectra for the above discussed benchmark model on a sodium iodide target are shown both without assumed resolution (magenta dashed) and convoluted with a normal distribution of various σ (solid lines). The couplings of the light mediator are chosen in such a way, that for one the destructive dip in the sodium dominated area is pronounced and can be easily studied (left panel) and for the other the dip in the iodine dominated area is more pronounced (right panel). In both cases the energy resolution changes the depth of the interference dips - for low resolutions (high σ) the features get smoothed out. However, for resolution up to 200 eV the dips are still visible. This shows the importance of choosing high resolution experiments if one wants to probe the bi-portal model. It is also important to note, that in the case of $\sigma = 0.5$ keV, the convolution has a strong impact on the spectrum at low recoil energies. This resolution based effect should not be confused with the behaviour of the spectrum in the top left panel of Figure 3.4 (magenta line).

In the previous chapter it was shown that the recoil spectra for the bi-portal model differ from the spectra from single mediator interaction and that there are deviations depending on the target materials. As a continuation, in this chapter it was demonstrated that recoil spectra for one and the same material can also differ significantly within the bi-portal model. Small changes in the free parameters of the model, i.e. masses and couplings, can lead to spectra of substantially different shape. Moreover, for a constant value of g_h, the two mediator model assumes a single light (heavy) mediator limit for high (low) values of the coupling of the light mediator. This limiting behaviour also occurs, when the total number of expected events is studied. In the last part of this chapter, the impact of a detector's resolution was investigated, coming to the conclusion that for a high-resolution experiment the destructive interference effects are observable. Unfortunately, so far direct detection experiments have not published results with unchallenged DM excess events [9], which would allow to compare predicted nuclear recoil spectra with measured data. However, one can instead investigate the effects the bi-portal model might have on exclusion limits for the free parameters. The statistical methods to calculate exclusion limits with a profile likelihood ratio are explained in the subsequent chapter.

Chapter 4

Statistics theory

The following chapter contains various statistical concepts which are needed in order to calculate exclusion limits with a profile likelihood ratio approach. The long list of required notions for the profile likelihood method is out-weighted by its advantages. Especially beneficial is the incorporation of the specific shape of the recoil spectrum in the analysis, as this shape distinguishes the bi-portal from a single mediator model. The concepts below are discussed in more detail in a Jupyter notebook[1] which can be found on GitHub. The notebook also includes some simple examples and applications as well as a discussion of the variance of maximum likelihood estimators.

The Bayesian notation $f(x|\theta)$ for a conditional probability density function (PDF) of an observed random variable x conditional on a particular value of θ is used in the style of Cowan [73] and Cousins [74].

4.1 Statistical tests

Statistical test are used in the analysis of experiments to give a measure of how well some observed data agrees with a theoretic model. The model, or in other words the hypothesis, is characterised by certain probabilities it predicts (e.g. probability to observe a certain number of events, measure a certain energy, etc.). In general the hypothesis in question is called the null hypothesis H_0, however in particle and high energy physics (HEP) the H_0 terminology is often used to describe the background-only process [75].

[1] A Jupyter notebook is a web-based interactive JSON documents, which contains both code in Pyhton, mathematics, plots and explanatory text in Markdown.

4.1.1 Hypothesis testing

Making a statement about the validity of H_0 is often done by comparing it with some alternative hypotheses $H_1, H_2, \ldots$ which are themselves again characterized by the probabilities they predict. For a data set consisting of n measurements $\boldsymbol{x} = (x_1, \ldots, x_n)$, each hypothesis in the set $H_0, H_1, \ldots$ is thus characterised by the respective PDF $f(\boldsymbol{x}|H_0), f(\boldsymbol{x}|H_1), \ldots$ [73]. To give a measure of the agreement between the observed data and a hypothesis, a so called test statistic is constructed. The test statistic $t(\boldsymbol{x})$ is a function of the measured variables and each hypothesis will presuppose a PDF for t denoted by $g(t|H_0), g(t|H_1)$ and so on. Assuming that one has defined a test statistic and knows its PDF for a certain hypothesis H_0, then the compatibility between model and data can be expressed in terms of a so called critical region for t. If the observed value of t is in the critical region, the hypothesis H_0 is rejected. The critical region is defined by the significance level α, which gives the probability that under the assumption of H_0 the observed t lies within the critical region.

To understand these concepts better, it is helpful to investigate an example. Consider an experiment where one counts the number of recoil events measured in some detector. The easiest way to define a test statistic in this case is to use the original vector of observed data values $\boldsymbol{x}$, which in this case is only one dimensional $\boldsymbol{x} = (x)$ [73]. Assume that for two hypotheses H_0, H_1 the outcome of the counting experiment is described by a Poisson distribution

$$f(\boldsymbol{x}|H_{0,1}) = \mathrm{Po}(x|\lambda_{0,1}) = \frac{\lambda^x e^{-\lambda}}{x!}, \tag{4.1}$$

where $\lambda_0 = b$ the number of background events for the null-hypothesis H_0 and $\lambda_1 = b+s$ the number of background plus signal events for the alternative hypothesis H_1. Since the test statistic is just the observed number of counts x, one can write $g(t|H_{0,1}) = f(x|H_{0,1})$.

In Figure 4.1 the two distributions of the test statistic are shown for a background of $b = 50$ events and a signal of $s = 25$ predicted by H_1. The critical region for H_0 is marked by t_{cut} (in this example arbitrarily fixed at 63), leading to a significance level

$$\alpha = \int_{t_{\mathrm{cut}}}^{\infty} g(t|H_0)dt. \tag{4.2}$$

The hypothesis H_0 would thus be accepted if one observes a value for t less than t_{cut} (i.e. counts less than 63 events). However, the null-hypothesis might be rejected

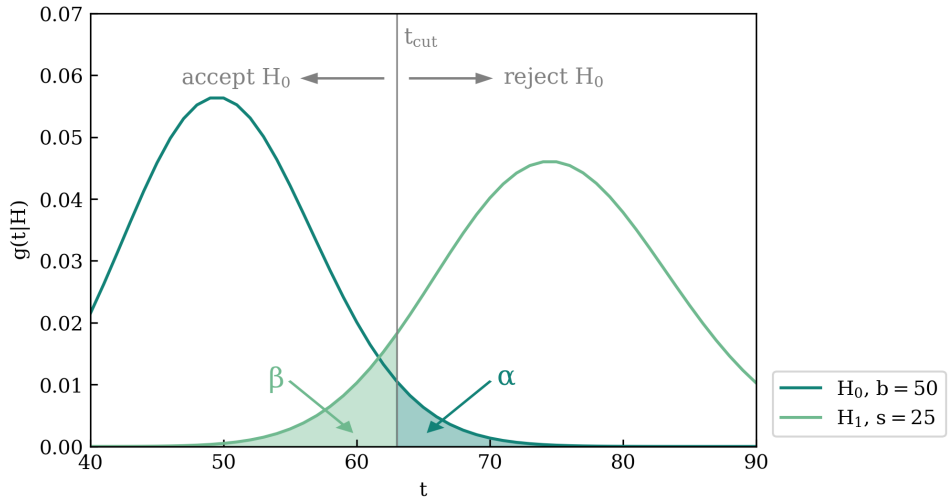

Figure 4.1: PDFs for the test statistic t under assumption of two different hypotheses H_0 and H_1. The underlying concept is a counting experiment, which can be described a Poisson distribution (4.1). The critical region for H_0 is marked by t_{cut}, i.e. H_0 is rejected if $t > t_{cut}$ is observed.

with a probability of α, although H_0 is true. This is called a type I error or false positive. There is a second misinterpretation of the data one could make, namely if H_0 is accepted while the true hypothesis was the alternative hypothesis H_1. This is a so called error of type II or false negative [76]. The probability for a false negative is marked in green in Figure 4.1 and given by

$$\beta = \int_{-\infty}^{t_{\text{cut}}} g(t|H_1)dt. \tag{4.3}$$

The complement $1 - \beta$ is called power of the statistical test as it gives a measure of the ability to discriminate against an alternative hypothesis.

4.1.2 Test of significance

In many cases the compatibility between a given hypothesis H and the observed data should be tested without comparison to an alternative hypothesis. This test of significance (or goodness-of-fit test) can be done via a test statistic which is constructed in such a way, that it gives measure of the compatibility of observation and the predictions of H. From the distribution of the test statistic one can then deduce the so called p-value. The p-values is the probability, under assumption of H, of finding data being as or more incompatible with the predictions of H than the observed data.

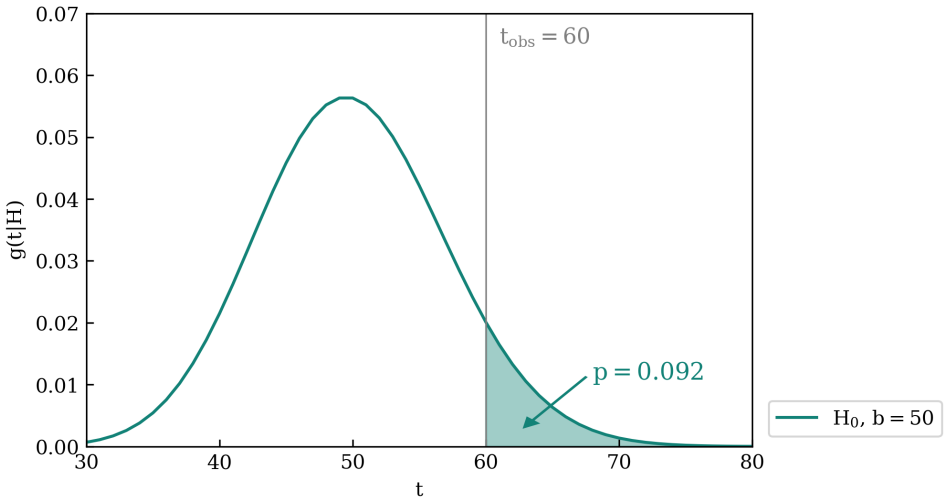

Figure 4.2: PDFs for the test statistic t under assumption of two the null hypothesis H_0. The underlying concept is a counting experiment, which can be described a Poisson distribution (4.1) with $\lambda = b = 50$ background-only events. The right-tailed $p - value$ is shown for an observed t of 60.

The counting experiment example from above is again useful to better understand this concept. Suppose one wants to test the compatibility of the null hypothesis H_0 with $b = 50$ and an observed number of counts of $x_{obs} = 60$. Remember that the test statistic t was just the observed number of counts and its PDF is given by a Poisson distribution with $\lambda = b = 50$. In this example equal or more incompatibility means observing as many or more than $x_{obs} = t_{obs}$ events and thus in Figure 4.2 the so called right-tailed p-value is shown. One should note that depending on the model and experiment under examination a left-tailed (as many or less than) or two-sided p-value might be the appropriate choice [77]. The right-tailed p-value is given by (for discrete $g(t|H)$ the integral may be replaced by a sum):

$$p\text{-value} = \int_{t_{obs}}^{\infty} g(t|H_0)dt \tag{4.4}$$

The p-value should not be confused with the significance level α which is a constant specified beforehand. The p-value, on the contrary, is a function of the data and therefore itself a random variable [78]. In an experiment one would then reject the hypothesis if the p-value is lower than a certain threshold, e.g $p < 0.05$ which corresponds to a so called confidence level (CL) of 95%. In the particle physics community the p-value is often converted into a significance Z, defined such that the right-tailed probability of a Gaussian distributed variable which is found Z standard deviations above its mean is equal to the p-value (again, not to be confused with

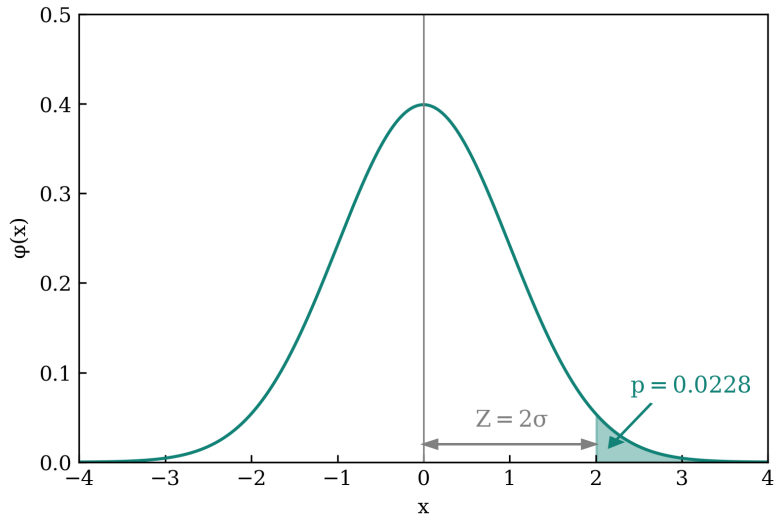

Figure 4.3: Illustration of the relation between the $p-value$ and the significance Z of a test statistic. The PDF displayed is a standard Gaussian ($\mu = 0$, $\sigma = 1$).

the significance *level* α). With the inverse cumulative distribution (quantile) φ^{-1} of the standard Gaussian this can be written as

$$Z = \varphi^{-1}(1 - p). \tag{4.5}$$

The relation between p-value and Z is illustrated in Figure 4.3 for a 2σ significance. For discoveries in particle physics, the general practice is to consider rejecting the background hypothesis with a significance of at least 5σ corresponding to a p-value of 2.87×10^{-7}. This significance was used, for example, when the discovery of the Higgs boson was claimed. For the exclusion of a signal hypothesis a confidence level of 95% is usually seen as sufficient. This corresponds to $Z = 1.64$ [75].

4.2 The method of maximum likelihood

Consider an experiment where a random variable $\boldsymbol{x}$ was measured n times resulting in the values $\boldsymbol{x}_1, \ldots, \boldsymbol{x}_n$. The variable $\boldsymbol{x}$ can also be a multidimensional random vector, so that the outcome of each measurement is characterized by several quantities (e.g. recoil energy and light yield for a nuclear recoil event). Assume that the functional form of the PDF $f(\boldsymbol{x}|\boldsymbol{\theta})$, according to which $\boldsymbol{x}$ is distributed, is known, but the value of at least one of the parameters in $\boldsymbol{\theta} = (\theta_1, \ldots, \theta_m)$ is not. The method of maximum likelihood gives a procedure to estimate these unknown parameters from a set of measured data.

For a certain value of $\boldsymbol{\theta}$, under the assumption that the data is described by $f(\boldsymbol{x}|\boldsymbol{\theta})$, the probability to find the first measurement equal to $\boldsymbol{x}_1$ is $f(\boldsymbol{x}_1|\boldsymbol{\theta})$. Assuming that all n measurements are independent the probability for the first measurement to yield $\boldsymbol{x}_1$, the second to yield $\boldsymbol{x}_2$ and so on is given by the likelihood function

$$L(\boldsymbol{\theta}) = \prod_{i=1}^{n} f(\boldsymbol{x}_i|\boldsymbol{\theta}). \tag{4.6}$$

The difference to the joint PDF for the $\boldsymbol{x}_i$ is that the above likelihood is treated as a function of the parameters $\boldsymbol{\theta}$ while the $\boldsymbol{x}_i$ are fixed. For a correctly hypothesized PDF and suitable $\boldsymbol{\theta}$ the expected probability for the actually measured data should be high and thus also the value of the likelihood. On the contrary, choosing $\boldsymbol{\theta}$ far away from the true value would yield a low value for the likelihood for the same PDF. Employing the argumentation above, the maximum likelihood (ML) estimates(s) for $\boldsymbol{\theta}$ can thus be defined as those which maximize the likelihood function - i.e. the solutions of $\frac{dL}{d\boldsymbol{\theta}} = 0$ for differentiable $L(\boldsymbol{\theta})$. The ML estimates are usually denoted with hats $\hat{\boldsymbol{\theta}} = (\hat{\theta}_1, \ldots, \hat{\theta}_m)$ to differentiate them from the true values of $\boldsymbol{\theta}$ which are unknown [73].

Especially when the ML estimators are determined via numerical methods, where one is restricted by the finite precision of the representation of real numbers, it is advantageous to use the negative logarithm of $L(\boldsymbol{\theta})$. The logarithm is a monotonically increasing function, so the parameter values which maximize L will also minimize $-\log L$. The build-up of error due to the numerical multiplication of a multitude of values varying in size is reduced by the conversion of the product in L into a sum by the logarithm [79]. Moreover, the negative is used in order to be able to use numeric minimizers. The negative log-likelihood function is then given by

$$-\log L(\boldsymbol{\theta}) = -\sum_{i=1}^{n} \log f(\boldsymbol{x}_i|\boldsymbol{\theta}). \tag{4.7}$$

4.2.1 Extended likelihood function

In the description above, the experiment consisted of performing a predetermined number of n measurements $\boldsymbol{x}_1, \ldots, \boldsymbol{x}_n$. However in particle and nuclear physics the expected number n of events to be observed is itself often a Poisson random variable and subject to fluctuations around a mean value ν [80]. In particular the Poisson parameter ν might be given as a function of $\boldsymbol{\theta}$. The extended likelihood function is

then given by [73]

$$L(\boldsymbol{\theta}) = \frac{\nu(\boldsymbol{\theta})^n}{n!} e^{-\nu(\boldsymbol{\theta})} \prod_{i=1}^{n} f(\boldsymbol{x}_i|\boldsymbol{\theta}) = \frac{e^{-\nu(\boldsymbol{\theta})}}{n!} \prod_{i=1}^{n} \nu(\boldsymbol{\theta}) f(\boldsymbol{x}_i|\boldsymbol{\theta}) \tag{4.8}$$

and the extended log-likelihood by

$$\log L(\boldsymbol{\theta}) = n \log \nu(\boldsymbol{\theta}) - \nu(\boldsymbol{\theta}) + \sum_{i=1}^{n} \log f(\boldsymbol{x}_i|\boldsymbol{\theta}) \tag{4.9}$$

$$= \nu(\boldsymbol{\theta}) + \sum_{i=1}^{n} \log(\nu(\boldsymbol{\theta}) f(\boldsymbol{x}_i|\boldsymbol{\theta})), \tag{4.10}$$

where the term $-\log n!$ is dropped as it does not depend on the parameters $\boldsymbol{\theta}$.

4.2.2 Binned likelihood

In the case of very large data samples the computational effort for the log-likelihood function can grow immensely, especially if the PDFs involve some kind of computationally expensive calculation. The data is then usually turned into a histogram with entries $n = (n_1, \ldots, n_N)$ in N bins. As in the section above we assume that the total number of events observed $n_{tot} = \sum_{i=1}^{N} n_i$ is itself a Poisson random variable with mean value $\nu_{tot}(\boldsymbol{\theta})$. For a hypothesized PDF $f(\boldsymbol{x}|\boldsymbol{\theta})$ the expected number of entries $\boldsymbol{\nu} = (\nu_1, \ldots, \nu_N)$ in each bin is then given by

$$\nu_i(\boldsymbol{\theta}) = \nu_{tot}(\boldsymbol{\theta}) \int_{x_i^{min}}^{x_i^{max}} f(\boldsymbol{x}|\boldsymbol{\theta}) d\boldsymbol{x} \tag{4.11}$$

where x_i^{min} and x_i^{max} are the bin limits and $\nu_{tot} = \sum_{i=1}^{N} \nu_i$.

The extended binned likelihood function is then just the product of the Poisson probabilities of all bins

$$L(\boldsymbol{\theta}) = \prod_{i=1}^{N} \frac{\nu_i(\boldsymbol{\theta})^{n_i}}{n_i!} e^{-\nu_i(\boldsymbol{\theta})}, \tag{4.12}$$

and the extended log-likelihood is

$$\log L(\boldsymbol{\theta}) = -\sum_{i=1}^{N} \nu_i(\boldsymbol{\theta}) + \sum_{i=1}^{N} n_i \log \nu_i(\boldsymbol{\theta}) \tag{4.13}$$

$$= -\nu_{tot}(\boldsymbol{\theta}) + \sum_{i=1}^{N} n_i \log \nu_i(\boldsymbol{\theta}), \tag{4.14}$$

with simplifications as for (4.9) [73, 75].

4.3 Likelihood ratio as test statistics

Before the relation between likelihood functions and goodness-of-fit tests can be discussed, the concept of nuisance parameters needs to be introduced. Take an observable $\boldsymbol{x}$ which is assumed to follow a probability density $f(\boldsymbol{x}|\boldsymbol{\theta})$ where $\boldsymbol{\theta} = (\theta_1, \ldots, \theta_m)$ is a vector of unknown parameters. Suppose a hypothesis H_0 should be tested, which predicts specific values for one or several (k) of the entries of $\boldsymbol{\theta}$, i.e.

$$H_0 : \theta_{i_1} = \theta^0_{i_1}, \theta_{i_2} = \theta^0_{i_2}, \ldots, \theta_{i_k} = \theta^0_{i_k} \quad \text{for} \quad \{i_1, \ldots i_k\} \subset \{1, \ldots, m\}. \tag{4.15}$$

The extant entries θ_j with $j \in \{1, \ldots, m\} \setminus \{i_1, \ldots i_k\}$ are then called nuisance parameters of the model [81]. In the following the variable $\boldsymbol{\theta}$ will only be used for the subset of nuisance parameters while the vector of parameters which is subject to the test will be denoted by $\boldsymbol{\mu}$. One thus writes $f(\boldsymbol{x}|\boldsymbol{\mu}, \boldsymbol{\theta})$ for the PDF and $L(\boldsymbol{\mu}, \boldsymbol{\theta})$ for the likelihood function given a measured set of data.

In a first step towards testing a hypothesized value of $\boldsymbol{\mu}$ the so called profile likelihood ratio is considered

$$\lambda(\boldsymbol{\mu}) = \frac{L(\boldsymbol{\mu}, \hat{\hat{\boldsymbol{\theta}}})}{L(\hat{\boldsymbol{\mu}}, \hat{\boldsymbol{\theta}})}. \tag{4.16}$$

The denominator is given by the so called unconditional likelihood function, where both $\hat{\boldsymbol{\mu}}$ and $\hat{\boldsymbol{\theta}}$ are their ML estimators. In the nominator the nuisance parameters are chosen in such a way, that L is maximized for specific values of $\boldsymbol{\mu}$. This so called conditional ML estimator of $\boldsymbol{\theta}$ is denoted by $\hat{\hat{\boldsymbol{\theta}}}$. The likelihood in the nominator is thus a function of $\boldsymbol{\mu}$ [75]. For good agreement between the best fit to the data and the hypothesized value of $\boldsymbol{\mu}$ the likelihood ratio yields values close to one. Conversely in the case of bad agreement the likelihood in the denominator is much higher than the one in the nominator and λ is close to zero.

From the likelihood ratio a test statistic

$$\begin{aligned} t_{\boldsymbol{\mu}} :=& -2 \log \lambda(\boldsymbol{\mu}) \\ =& 2 \log L(\hat{\boldsymbol{\mu}}, \hat{\boldsymbol{\theta}}) - 2 \log L(\boldsymbol{\mu}, \hat{\hat{\boldsymbol{\theta}}}) \end{aligned} \tag{4.17}$$

can be constructed, where high compatibility between data and hypothesis is indicated by an increasing value of $t_{\boldsymbol{\mu}}$. In subsection 4.1.2 the p-value was defined as a measure of equal or greater discrepancy between data and hypothesis. For the profile likelihood ratio as a test statistic this thus means that the p-value can be

calculated with

$$p_{\boldsymbol{\mu}} = \int_{t_{\boldsymbol{\mu},\mathrm{obs}}}^{\infty} g(t_{\boldsymbol{\mu}}|\boldsymbol{\mu}) dt_{\boldsymbol{\mu}}. \tag{4.18}$$

The function $g(t_{\boldsymbol{\mu}}|\boldsymbol{\mu})$ is the PDF of the test statistic under the assumption of $\boldsymbol{\mu}$. Wilks' theorem [82] offers an asymptotic description of the distribution of $t_{\boldsymbol{\mu}}$ in the large sample limit. For $\boldsymbol{\mu}$ being a vector of size k, $g(t_{\boldsymbol{\mu}}|\boldsymbol{\mu})$ can be approximated by a χ^2 distribution with k degrees of freedom. In the work by Cowan et al. [75] this concept has been extended to modified versions of the test statistic (4.17).

Before applying the above formalism in the context of discovery and exclusion in an experiment, there is one more thing to take care of. Especially in physics applications the parameter(s) μ might resemble some physical quantity, like a cross section or the mass of some particle. In this case negative values would be unphysical, which can lead to a problem if the ML estimator of μ is negative. In these cases one defines an alternative test statistic

$$\tilde{t_\mu} := \begin{cases} -2\log\left(L(\mu, \hat{\hat{\boldsymbol{\theta}}}(\mu))/L(\hat{\boldsymbol{\mu}}, \hat{\boldsymbol{\theta}})\right), & \hat{\boldsymbol{\mu}} \geq 0, \\ \\ -2\log\left(L(\mu, \hat{\hat{\boldsymbol{\theta}}}(\mu))/L(0, \hat{\hat{\boldsymbol{\theta}}}(0))\right), & \hat{\boldsymbol{\mu}} < 0, \end{cases} \tag{4.19}$$

where $\hat{\hat{\boldsymbol{\theta}}}(0)$ and $\hat{\hat{\boldsymbol{\theta}}}(\mu)$ represent the conditional ML estimators given a parameter of 0 and μ respectively.

4.3.1 Discovery

One application of the above formalism is to judge if the result of an experiment is significant enough to claim a discovery. In order to do this a test of significance is performed where the null hypothesis ($\boldsymbol{\mu} = 0$) is compared to the best-fit value, i.e. the profile likelihood ratio

$$\lambda(0) = \frac{L(0, \hat{\hat{\boldsymbol{\theta}}})}{L(\hat{\boldsymbol{\mu}}, \hat{\boldsymbol{\theta}})} \tag{4.20}$$

is examined. From this ratio one can construct the statistic t_0 as in (4.17) and the p-value for a certain observed $t_{0,\mathrm{obs}}$ is

$$p_0 = \int_{t_{0,\mathrm{obs}}}^{\infty} g(t_0|0) dt_0. \tag{4.21}$$

In the special case of μ being a one-dimensional vector (i.e. χ^2 with one degree of freedom), applying Wilks' theorem [82] together with the approximation of the cumulative distribution function for χ^2 by the cube of a Gaussian leads to a simple expression for the significance [73]:

$$Z = \sqrt{t_0} \tag{4.22}$$

The statistic t_0 is the most general to test a null-hypothesis which may be rejected for both upward or downward fluctuation of the data. However, in the case of an experiment where lack of agreement with the null-hypothesis only occurs for an increased signal strength the test statistic has to be modified [75]. For a measured signal strength below the one predicted by the null-hypothesis, H_0 does not necessarily need to be dismissed. The signal strength can usually be expressed as function of the model-dependent parameters and will here be denoted by $s(\boldsymbol{\mu})$. The appropriate test statistic is then given by

$$q_0 := \begin{cases} -2\log\lambda(0), & s(\hat{\boldsymbol{\mu}}) \geq s(0), \\ 0\ , & s(\hat{\boldsymbol{\mu}}) < s(0). \end{cases} \tag{4.23}$$

Whenever $s(\mu) = \mu$, i.e. the parameter is a direct measure of the signal strength like the cross section, the test statistic q_0 is equivalent to $\tilde{t_0}$ from (4.19) and thus consistent with the notation in [75].

4.3.2 Exclusion

The profile likelihood ratio can also be used to find so called exclusion limits on the parameters $\boldsymbol{\mu}$ for an a-priori fixed confidence level. In other words, exclusion limits give a measure of how much signal can be hidden in the background. For $\boldsymbol{\mu}$ being a $1 \times k$ dimensional vector the $1 - p$ CL limits are given by the boundaries of the k-cell $[\mu_{1,\min}, \mu_{1,\max}] \times \cdots \times [\mu_{k,\min}, \mu_{k,\max}]$ being the union of all $\boldsymbol{\mu}$ for which [74]

$$\int_{t_{\boldsymbol{\mu}}}^{\infty} g(t_{\boldsymbol{\mu'}}|\boldsymbol{\mu'})dt_{\boldsymbol{\mu'}} \leq p. \tag{4.24}$$

Using Wilks' theorem [82] this condition is equivalent to

$$1 - \mathrm{CDF}_{\chi^2}(k, t_{\boldsymbol{\mu}}) \leq p, \tag{4.25}$$

where $\mathrm{CDF}_{\chi^2}(m, x)$ denotes the cumulative distribution function of a χ^2 distribution with k degrees of freedom [83, 84].

As in the section about discovery the case where only increased signal strength is regarded as incompatible with the null-hypothesis has to be treated with certain care. Another test statistic is thus defined by

$$q_{\boldsymbol{\mu}} \coloneqq \begin{cases} -2\log\lambda(\boldsymbol{\mu}), & s(\hat{\boldsymbol{\mu}}) \leq s(\boldsymbol{\mu}), \\ 0\ , & s(\hat{\boldsymbol{\mu}}) > s(\boldsymbol{\mu}). \end{cases} \tag{4.26}$$

The reasoning for setting $q_{\boldsymbol{\mu}} = 0$ for $s(\hat{\boldsymbol{\mu}}) > s(\boldsymbol{\mu})$ goes as follows: If for a certain set of parameters $\boldsymbol{\mu}$ the signal strength is lower than the signal strength for the best fit to the data, this does not imply less compatibility with the null-hypothesis, but rather some other systematic error (wrongly estimated efficiency of the detector etc.). The possible higher value of q_μ is thus ignored and the parameters $\boldsymbol{\mu}$ are not rejected. The special case where the parameter is a direct measure of the signal strength ($\mu = s(\mu)$) is described in detail in the work by Cowan et al. [75].

Chapter 5

Exclusion limits in the bi-portal model

If DM direct detection experiments do not see an excess signal from which a discovery can be claimed, the data taken is used to find exclusion limits[1] on DM-SM interaction specific quantities like the masses and cross sections/couplings. While Yellin's optimum interval method [85, 86] was widely-used in the previous decade to generate exclusion limits, many experiments now tend to the likelihood approach described in chapter 4. To name some examples: profile likelihood ratio methods have been used for a positive (discovery) analysis in the CRESST-II experiment [87], as well as by the XENON cooperation starting with XENON100 [18]. In this work the profile likelihood approach was used to deduce exclusion limits on (subsets of) the four free parameters $m_{Z_l'}, m_\chi, g_l, g_h$ of the bi-portal models. Rather than real recoil data from experiments, mock background data was used in the calculation. The mock recoil energies were generated using the inverse transform sampling method from experiment-specific probability distributions - for the precise procedure see appendix B.1.

To simplify the limit calculation, quantities which are usually regarded as nuisance parameters, e.g. exact value of the Earth's velocity, the local dark matter density, are assumed to be known precisely. Therefore, the only nuisance parameter incorporated in the calculations is the background level l_b and the profile likelihood ratio (4.16) simplifies to

$$\lambda(\boldsymbol{\mu}, \hat{\hat{\boldsymbol{l_b}}}) = \frac{L(\boldsymbol{\mu})}{L(\hat{\boldsymbol{\mu}}, \hat{\boldsymbol{l_b}})}. \tag{5.1}$$

[1] At experiments standard DM-limits are computed for a 90% CL.

5.1 Likelihood function

In the first step of setting exclusion limits, the appropriate likelihood function has to be found. There are two different types of events for which a PDF-like function needs to be constructed: DM events and background events. The distribution of dark matter events is given by the differential recoil spectrum $\frac{dR_\chi}{dE_R}$. For the background rate simplified models are used, either a flat background

$$\frac{dR_b}{dE_R} = c \tag{5.2}$$

with $[c] = 1/(\text{keV kg d})$, or a background with a slightly falling slope

$$\frac{dR_b}{dE_R} = c - a \cdot E_R, \tag{5.3}$$

where $[a] = 1/(\text{keV}^2 \text{ kg d})$. If the resolution of the detector should also be included, the full the rate of signal events has to be convolved with a Gaussian energy distribution according to (3.2). For the simple background models used in this analysis it is not necessary to included the resolution, as these are empiric models of the background observed in the detector after energy reconstruction.

The total recoil spectrum needs to be normalized to achieve a probability density function. In the calculation of DM plus background events experiment specific quantities like the exposure ε and the threshold energy E_{thr} are included:

$$N_{\text{tot}}(\boldsymbol{\mu}, l_b) = N_\chi(\boldsymbol{\mu}) + N_b(l_b) = \varepsilon \int_{E_{\text{thr}}}^{E_{\max}} \left(\frac{dR_\chi}{dE_R}(\boldsymbol{\mu}) + l_b \frac{dR_b}{dE_R} \right) dE_R \tag{5.4}$$

The upper limit of the integral $E_{\max}$ is fixed depending on the background model. For a falling background $E_{\max} = \frac{c}{a}$, i.e. the point where the expected background spectrum ($l_b = 0$) goes to zero. In the case of a constant background a region of interest (ROI) for the recoil energies is set, in which the bulk of energies of possible DM events is assumed to lie. The upper bound of the ROI can then be used as $E_{\max}$. When choosing the ROI one has to take the mass of the dark matter particle for which the search is aimed at, into account.

In the following, the four free parameters of the model will be denoted by the vector $\boldsymbol{\mu} = (m_{Z'_l}, m_\chi, g_l, g_h)$. For N_{obs} recoil energies $(E_{R_1}, \ldots, E_{R_{N_{obs}}})$ in a (mock) sample the extended likelihood function is thus given by

$$L(\boldsymbol{\mu}, l_b) = \frac{N_{\text{tot}}(\boldsymbol{\mu})^{N_{\text{obs}}} e^{N_{\text{tot}}(\boldsymbol{\mu}, l_b)}}{N_{\text{obs}}!} \prod_{i=1}^{N_{\text{obs}}} \frac{\frac{dR_\chi}{dE_R}(\boldsymbol{\mu}, E_{R_i}) + \frac{dR_b}{dE_R}(l_b, E_{R_i})}{N_{\text{tot}}(\boldsymbol{\mu})} \tag{5.5}$$

$$= \frac{e^{N_{\text{tot}}(\boldsymbol{\mu}, l_b)}}{N_{\text{obs}}!} \prod_{i=1}^{N_{\text{obs}}} \left(\frac{dR_\chi}{dE_R}(\boldsymbol{\mu}, E_{R_i}) + \frac{dR_b}{dE_R}(l_b, E_{R_i}) \right) \tag{5.6}$$

Interestingly the extended likelihood formalism makes the normalization of the spectrum redundant, a feature also described in [80]. For experiments with a very high exposure ε the recoil energy sample can be quite large and a binned likelihood approach might be advantageous. Thus the data has to be arrange in N_{bins} bins with $(n_i, \ldots, n_{N_{\text{bins}}})$ entries, where the bin width w_{bin} has to be carefully attuned to threshold and resolution of the experiment. Following subsection 4.2.2 the likelihood function is then given by

$$L(\boldsymbol{\mu}, l_b) = \prod_{i=1}^{N_{\text{bins}}} \frac{\nu_i(\boldsymbol{\mu}, l_b)^{n_i}}{n_i!} e^{-\nu_i(\boldsymbol{\mu}, l_b)} \tag{5.7}$$

where

$$\nu_i(\boldsymbol{\mu}) = \varepsilon \int_{E_{\text{thr}}+(i-1)w_{\text{bin}}}^{E_{\text{thr}}+iw_{\text{bin}}} \left(\frac{dR_\chi}{dE_R}(\boldsymbol{\mu}, E'_R) + \frac{dR_b}{dE_R}(l_b, E'_R \right) dE'_R. \tag{5.8}$$

5.2 Test statistic

In DM direct detection, only a signal strength higher than the assumed background signal gives reason to reject the null-hypothesis. A lower signal rather indicates some kind of systematic error, e.g a wrong approximation of the background. Most experiments publish mass-dependent limits on some DM-nucleon reference cross section σ_n, where there is a direct correspondence between $\mu = \sigma_n$ and the signal strength. In the case of the bi-portal model we want to give mass-dependent limits on the couplings. However, in section 3.3 it was shown that increasing the absolute value of the coupling does not necessarily increase the signal. Therefore an additional parameter for the signal strength $s(\boldsymbol{\mu})$ needs to be introduced to define a test statistic as in (4.26). The best choice is to use the total number of events $N_{\text{tot}}(\boldsymbol{\mu})$ as a measure of the signal strength, since it already needs to be computed for each $\boldsymbol{\mu}$ in the likelihood function (5.5). In the case of a binned likelihood it is simply given by $\sum_{i=1}^{N_{\text{bins}}} n_i$. On the lines of (4.26) the most general form of the test statistic for the bi-portal model is thus

$$q_{\boldsymbol{\mu}} \coloneqq \begin{cases} -2 \log \lambda(\boldsymbol{\mu}), & N_{\text{tot}}(\hat{\boldsymbol{\mu}}, \hat{\boldsymbol{l}}_{\boldsymbol{b}}) \leq N_{\text{tot}}(\boldsymbol{\mu}, \hat{\hat{l}}_b), \\ 0 \ , & N_{\text{tot}}(\hat{\boldsymbol{\mu}}, \hat{\boldsymbol{l}}_{\boldsymbol{b}}) > N_{\text{tot}}(\boldsymbol{\mu}, \hat{\hat{l}}_b). \end{cases} \tag{5.9}$$

5.3 Exclusion limit planes

To draw exclusion limits in a two dimensional plane, two out of the four free parameters of the bi-portal model need to be fixed. The other two parameters then give the axes of the exclusion plot. In the following the procedure to calculate exclusion limits in two different such planes is explained with the help of short pseudocodes.

5.3.1 m_χ-g_l exclusion limits

The first possibility is to generate limits on the light mediator coupling g_l as a function of the dark matter mass m_χ. The mass of the light mediator and the effective coupling for the heavy mediator are thus fixed. Two different hypothesis, the constructive case where g_l and g_h have the same sign and the destructive case where g_l and g_h have opposite signs, have to be considered. Note that, for a fixed value of g_h this gives a constraint on the allowed sign of g_l if each of the two hypothesis should be tested separately. This additional condition can be achieved by passing a high value in the negative-log-likelihood calculation whenever g_l has the wrong sign. In this way the signature of $\hat{g}_l$ can be controlled. For a certain p-value and a fixed DM mass the interval of non-excluded couplings $[g_{l,\min}, g_{l,\max}]$ is thus given by the union of all g_l for which

$$1 - \mathrm{CDF}_{\chi^2}(1, q_{g_l, m_\chi = \text{fixed}}) \leq p. \tag{5.10}$$

Using the quantile of the χ^2 function with 1 degree of freedom (as the number of free parameters gets reduced to one, namely the coupling g_l in the likelihood ratio, independent of the number of nuisance parameters), for a confidence level of 95% the above condition reads:

$$q_{g_l, m_\chi = \text{fixed}} \leq 3.841 \tag{5.11}$$

In the constructive interference case, lowering g_l for a fixed g_h always leads to a decrease in the number of predicted events $N_{\text{tot}}(g_l)$. For couplings lower than a certain value $\bar{g}_l$ with $N_{\text{tot}}(\bar{g}_l, m_\chi = \text{fixed}) \leq N_{\text{tot}}(\hat{g}_l, m_\chi = \text{fixed})$ the couplings always lie within the non-excluded region, due to the definition of the test statistic (5.9). The likelihood interval of light mediator couplings for the constructive hypothesis is thus not bound from below and only an upper limit needs to be found in the computation. In this work the limit is found using a bisection like procedure specified in section B.4. As mentioned above, in the destructive case there is such no linear relation between g_l and N_{tot}. For certain combinations of g_h, $m_{Z_l'}$ and m_χ, there might thus an upper and lower limit on the light mediator coupling.

Whenever the threshold and energy resolution of the detector are taken into account, there is another issue which has to be taken care off. A detector is only sensitive to DM masses for which the maximum deposited recoil energy is higher than the threshold. However, performing a convolution of the differential recoil rate for very light DM masses with the energy resolution, results in a shuffling of events over the threshold. This may result in limits on the coupling for very low DM masses, which are not accessible for the detector considering their very low true deposited recoil energy. To solve this problem in a conservative way, the similar approach to the CRESST experiment's [14] was taken. Simulated events are rejected when their true energy is more than two σ (mean of Gaussian resolution distribution) under the threshold. This concept is explained in more detail in section B.2.

Taking into account all statements made above, the pseudocode for the calculation of limits in the m_χ-g_l plane is of the following structure:

Pseudocode 1: calculate m_χ-g_l exclusion limits

```
Input: mock background data
Output: limits on g_l
fix g_h > 0, m_{Z'_l}
create m_χ-array
case constructive do
    for m_χ in m_χ-array do
        minimize denominator of likelihood ratio in g_l for fixed m_χ
        define test statistic q_{g_l, m_χ=fixed}
        find upper limit on g_l under condition (5.11)
case destructive do
    for m_χ in m_χ-array do
        minimize denominator of likelihood ratio in −g_l for fixed m_χ
        define test statistic q_{−g_l, m_χ=fixed}
        find lower limit on |−g_l| under condition (5.11)
        find upper limit on |−g_l| under condition (5.11)
```

5.3.2 $m_{Z_l'}$-g_l exclusion limits

Exclusion limits on the coupling as a function of the dark matter mass are comparable to the cross section - DM mass limits known from the publication of direct detection experiments. In the two-mediator model, however, a second possibility for limits arises. Fixing the mass of the DM particle as well as one of the couplings leads to limits on the other coupling as a function of the light mediator mass. One can thus achieve limits in the $m_{Z_l'}$-g_l plane as seen for collider searches [88]. The condition for the likelihood intervall at 95% CL reads

$$q_{g_l, m_{Z_l'}=\text{fixed}} \leq 3.841 \tag{5.12}$$

and the according pseudocode for the limit calculation is given by:

Pseudocode 2: calculate $m_{Z_l'}$-g_l exclusion limits

```
Input: mock background data
Output: limits on g_l
fix g_h > 0, m_{Z_l'}
create m_χ-array
case constructive do
    for m_χ in m_χ-array do
        minimize denominator of likelihood ratio in g_h for fixed m_χ
        define test statistic q_{g_l, m_{Z_l'}=fixed}
        find upper limit on g_l under condition (5.12)
case destructive do
    for m_χ in m_χ-array do
        minimize denominator of likelihood ratio in −g_h for fixed m_χ
        define test statistic q_{−g_l, m_{Z_l'}=fixed}
        find lower limit on |−g_l| under condition (5.12)
        find upper limit on |−g_l| under condition (5.12)
```

5.4 Results

In the following, exclusion limits in the $m_\chi - g_l$ and the $m_{Z'_l} - g_l$ plane are shown for mock data samples generated on the basis of two different experiments: the CRESST-III experiment and the proposed COSINUS experiment. The detector specific quantities used in the limit calculation are shown in Table 5.1 together with the respective references. The CRESST experiment experiment was chosen due to its very low threshold/high resolution, which make it sensitive to possible interference effects arising at low recoil energies. The COSINUS experiment was chosen as sodium iodide proved to be advantageous to test bi-portal models in the analysis of the recoil spectrum. In chapter 2 and chapter 3 this was advantage was explained by the high difference in the nuclear masses of iodine and sodium.

Table 5.1: Overview of experiment/detector specific parameters used in the calculation of exclusion limits from mock data.

	CRESST-III (Detector A) [14, 16]	COSINUS [19]
target material	$CaWO_4$	NaI
net exposure ε	3.46 kg day	50 kg day[2]
threshold E_{thr}	0.0301 keV	1 keV
phonon resolution σ	0.0046 keV	0.2 keV
background	$\frac{dR_b}{dE_R} = 3.518 - 0.025 E_R \ \frac{1}{(\text{keV kg d})}$ [3]	$\frac{dR_b}{dE_R} = 1 \ \frac{1}{(\text{keV kg d})}$

The calculation of exclusion limits is computationally a very time consuming process, especially if the detector resolution is included as the convolution integral has to be evaluated in every minimization step. Since the σ-value purports the fineness of the numerical integration for the convolution, higher resolutions (low σ) lead to higher computation times. Therefore, only for the experiment with the lowest resolution, COSINUS, the whole analysis is performed taking the resolution into account. For the other experiment the possible impact of the detectors' resolution is demonstrated by means of an example and the bulk of the limits are calculated without the convolution. Another difference in the limit calculation for these two experiments, is that for the CRESST-like sample an unbinned approach is used, while for the COSINUS sample the likelihood function is binned. The decisive

[2] According to a gross exposure of 100 kg day and an assumed overall efficiency of 50%.

[3] This model for a falling background was set under the assumption, that the CRESST-group is able to dispose of the exponential falling background at low recoil energies. were kindly provided by Florian Reindl, who is part of the CRESST group at HEPHY Vienna.

factor here is the overall number of background events in the mock sample, which is significantly lower for CRESST due to the lower exposure. When binning the mock background data for COSINUS one has to take care that the width of the bins is compatible with the experiment's resolution.

The first limits displayed are for the COSINUS-like background sample, where the experiment's resolution is considered in the whole limit calculation process. In Figure 5.1 exclusion limits at 95% CL are shown in the $m_\chi - g_l$ plane with the light mediator mass fixed to 10 MeV. In each of the four panels the limits were calculated under assumption of different values for the effective heavy mediator coupling ranging from $5 \times 10^{-13}\,\mathrm{MeV}^{-2}$ down to $1 \times 10^{-14}\,\mathrm{MeV}^{-2}$. In each panel exclusion limits are shown for the constructive (solid line) and destructive case (dashed line) of the bi-portal model in blue, together with an upper exclusion limit calculated for a single light mediator interaction (i.e. $g_h = 0$) in black. In order to improve perceivability, for the bi-portal model the *allowed region* is shaded. A threshold of 1 keV together with a resolution of $\sigma = 0.2$ keV corresponds to a sensitivity down to DM masses of about 1 GeV according to equation (B.3). We begin with the analysis of the bottom right window, where all three limits lie very close together. This can be explained by the low value of g_h, due to which the heavy mediator plays an inferior role in the bi-portal model. This leads to a limiting case as described in chapter 3 and results in the bi-portal exclusion limits resembling those of an interaction via a single-light mediator. In the bottom left panel, increasing the coupling of the heavy mediator leads to a divergence between the different limits. The interference term in the matrix element starts to come into play, which leads to an increased overall rate in the constructive bi-portal model and thus a lower limit compared to the single light mediator case. The opposite is true for the destructive case, where more values of g_l are allowed compared to the single mediator case. The effects of the interference terms are more noticeable for higher DM masses and at masses under 2-3 GeV the limits merge again. For lower DM masses the respective recoil energies at which the differential recoil rate is the highest and the interference terms have their strongest effect, tend to lie under the threshold and are thus not accessible (compare with Figure 3.2 and Figure 3.4). This is also consistent with the statement made earlier, that for sodium iodide the highest impact on the number of total events comes from the iodide contribution. Indeed for iodide $E_{\mathrm{max}} \approx 0.6 = E_{\mathrm{thr}} - 2\sigma$ for $m_\chi = 2.5$ GeV. In the upper right panel the bi-portal limits differ even more from the single mediator limit in black. In this

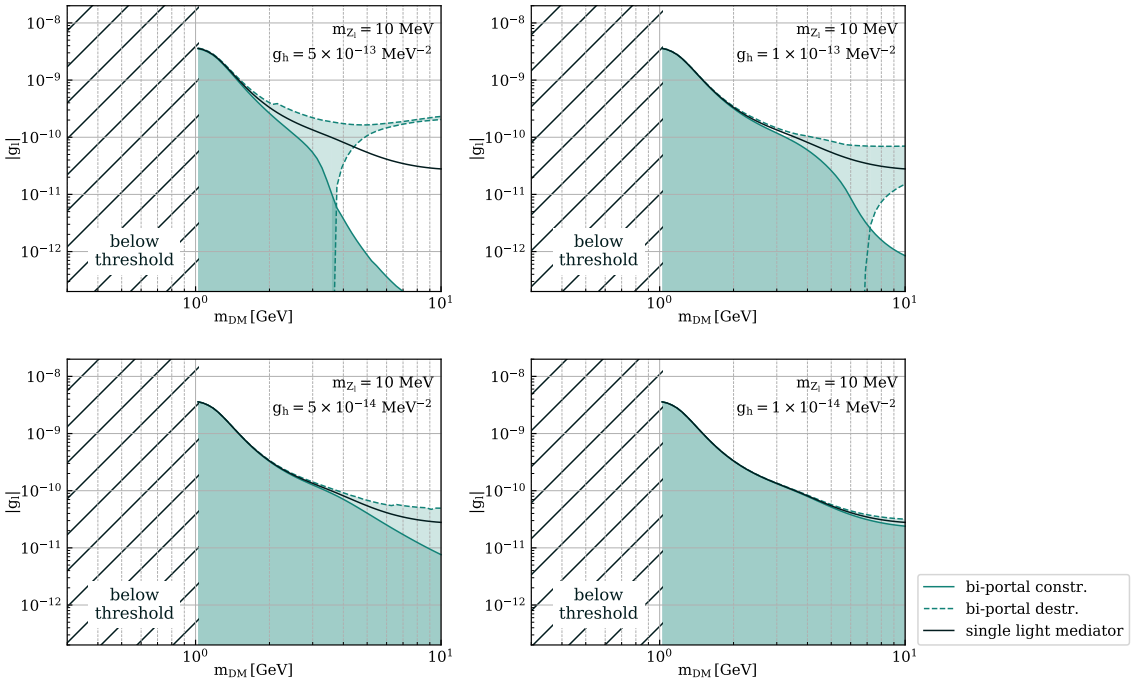

Figure 5.1: Exclusion limits (at 95% CL) on the light mediator coupling as a function of the DM mass for a COSINUS-like mock background sample. The light mediator mass is fixed and each panel shows limits for a different value of the effective heavy mediator coupling. Limits in blue are for the bi-portal model in the constructive case (solid) and in the destructive case (dashed), in comparison to limits in black for a single light mediator case. For the bi-portal model the non-excluded parameter space is shaded. Resolution and threshold of the experiment are considered in the calculation.

panel g_h is one order higher than in the bottom right one, and the overall rates for a certain value of g_l is thus significantly higher. This higher rate leads to lower upper exclusion limits in the constructive case. Furthermore, one of the most interesting aspects of the bi-portal model limits starts to show: the lower limit on g_l in the destructive case. In this case, values of g_l might still be allowed if, in combination with $g_h = 1 \times 10^{-13}\text{MeV}^{-2}$, they generate a large destructive interference term, which lowers the overall number of predicted events. However, if g_l is too low, the interference term might not be large enough to reduce the predicted number of events sufficiently. This results in an allowed region of g_l in the exclusion plot which is restricted both from above and below. Again, this effect is only visible for higher DM masses, as for lower m_χ higher rates might be hidden by the threshold. In the top left panel with $g_h = 5 \times 10^{-13}\text{MeV}^{-2}$, g_l is even more restricted and for $m_\chi \geq 6$ only a narrow band of values is allowed in the destructive case. For the very high value of g_h in this panel, the heavy mediator interaction component of the bi-portal model by itself already leads to a high number of predicted events. Therefore, in the

constructive case only very low values for g_l are compatible with a possible DM signal hiding in the background sample. In the destructive case the number of predicted events can be reduced, by those g_l which lead to destructive interference effects (i.e. in general high impact of the interference term, not necessarily in the form of dips). If the coupling of the heavy mediator is further increased, the allowed region for g_l would be further restricted, up to the point where only $g_l =$ is allowed at 95% CL. This would then correspond to the bi-portal model assuming its single heavy mediator limit, where interaction via the light mediator is completely suppressed. To conclude, adding a heavy mediator of some fixed coupling to the DM-nucleus interaction via a light mediator, leads to different limits on the light mediators coupling in the $m_\chi - g_l$ plane. Moreover, there is a significant difference between the constructive and the destructive case.

In Figure 5.2 exclusion limits (at 95% CL) for a COSINUS-like mock background sample are again shown in the $m_\chi - g_l$ plane. Here the effective coupling of the heavy mediator is fixed, while each panel shows limits for a different value of $m_{Z_l'}$. Only limits in the bi-portal model are shown in this figure and non-excluded regions are again shaded. Overall, higher mediator masses lead to higher allowed values for g_l. This can be reasoned by the inverse proportionality of the differential recoil rate (and also the total events rate) to the mediator mass. For lower $m_{Z_l'}$ a light mediator interaction model predicts a higher number of events and the limit on the coupling thus has to be lower (see also the exclusion plots in [83]). This also has a strong effect on the bi-portal model. Especially for $m_{Z_l'} = 0.1\,\mathrm{MeV}$ in the upper left panel, the model is dominated by the light mediator and there are no noticeable differences visible between constructive and destructive case. Moreover, since the impact of the interference term is very low compared to the contribution from the light mediator, there is no lower limit on g_l in the destructive case. In the next panel with $m_{Z_l'} = 1\,\mathrm{MeV}$ interference effects start to show again. For higher DM masses the limits are very similar to those in the next panel for $m_{Z_l'} = 10$ which is identical to the already discussed top right panel of Figure 5.1. For lower DM masses the limits are however flatter, which is due to the lower mediator mass. In the lower right panel the exclusion limits are shown for a mediator of mass 100 MeV. With this mass the mediator falls into the regime where $m_Z^2 > q^2$ and the interaction thus takes place via two heavy mediators. Even though the limit of two heavy mediators does not lead to destructive interference effects in the form of dips in the differential recoil spectrum, the second heavy mediator still has an effect on the exclusion limits. This is due to the fact, that the interference term in the cross section still has the

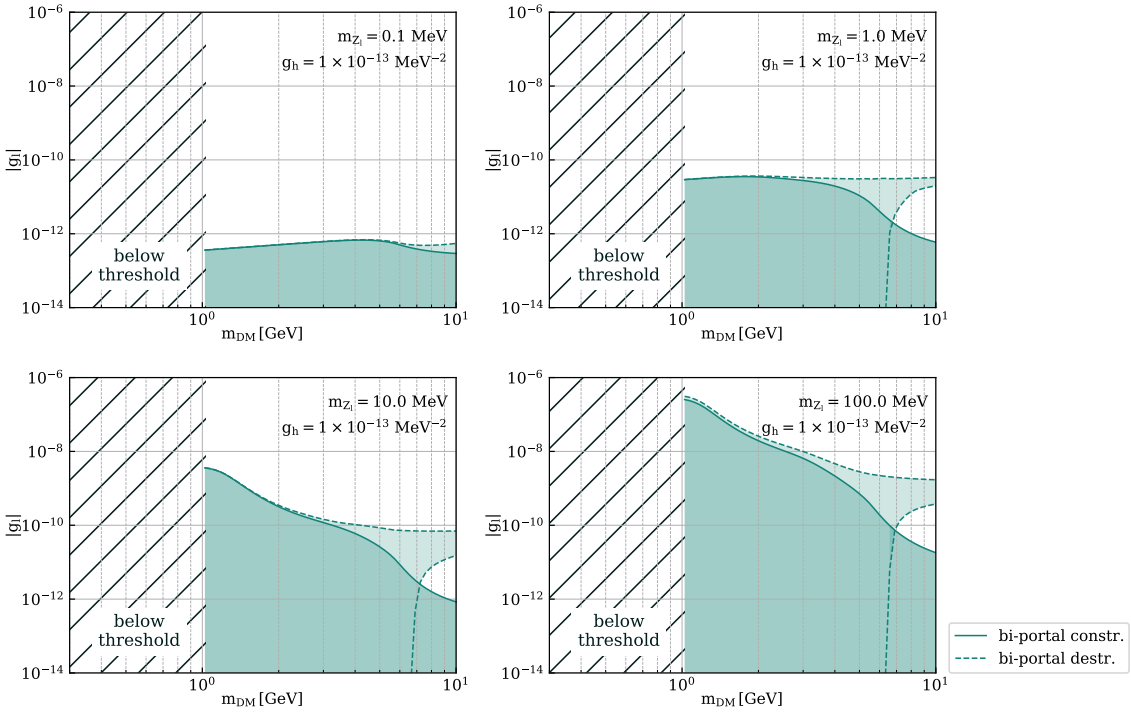

Figure 5.2: Exclusion limits (at 95% CL) on the light mediator coupling as a function of the DM mass for a COSINUS-like mock background sample. The effective heavy mediator coupling g_h is fixed at $1 \times 10^{-13}\,\mathrm{MeV}^{-2}$ and each panel shows the limits for a different value of the light mediator mass. Limits are shown for the bi-portal model in the constructive case (blue solid) and in the destructive case (blue dashed). The non-excluded parameters space is shaded respectively. Resolution and threshold of the experiment are considered in the calculation.

ability to lower/raise the total number of effects in the constructive/destructive bi-portal model. The limits for the 2 heavy mediator case are thus similar in shape to the ones displayed in the bottom left label, just two order higher in g_l according to the scaling in the $m_{Z_l'}$.

Having analysed limits on g_l as a function of the DM mass, we now turn to limits in the $m_{Z_l'} - g_l$ plane. In Figure 5.3 these limits are shown for a DM particle of mass 10 GeV and various values for the effective coupling of the heavy mediator g_h. The limits for the constructive (blue solid) and destructive cases (blue dashed) of the bi-portal model are displayed together with the limit resulting from DM-nucleus interaction via a single light mediator. In all four panel higher values for the light mediator coupling are allowed for higher mediator masses. This behaviour can be explained by the inverse mass proportionality in all light mediator terms contributing to the matrix element which describes the DM-nucleus interaction. When going from higher to lower mediator masses, the limits get stronger as the

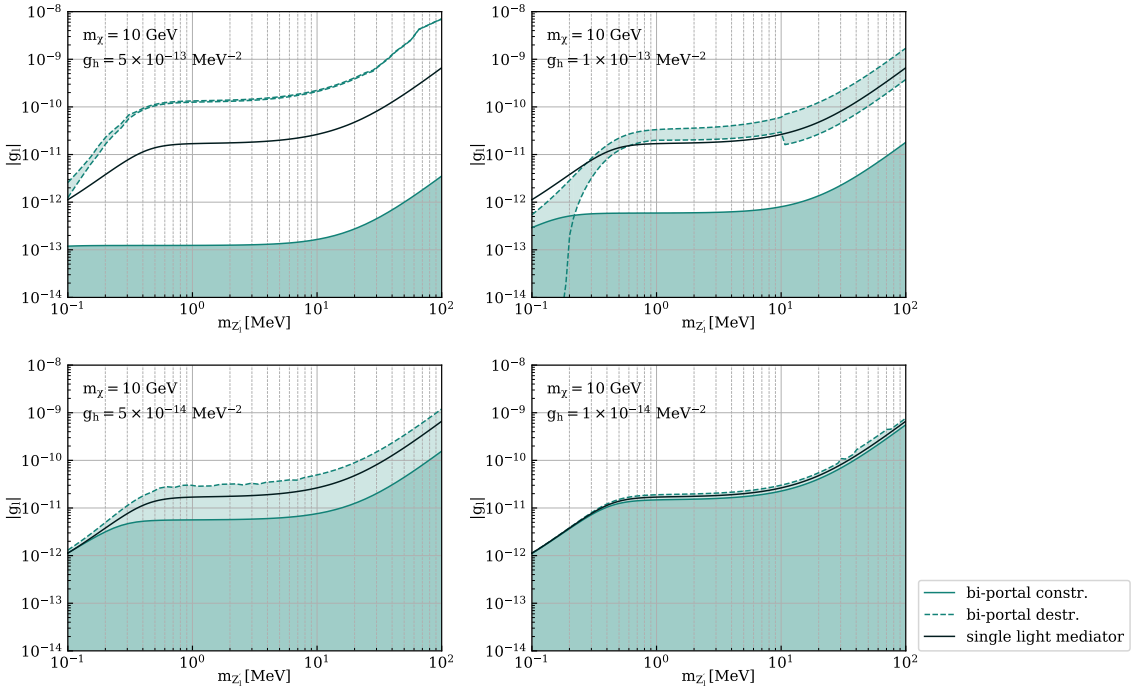

Figure 5.3: Exclusion limits (at 95% CL) on the light mediator coupling as a function of the light mediator mass for a COSINUS-like mock background sample. The DM mass is fixed at 10 GeV and each panel shows the limits for a different value of the heavy mediator coupling. Limits are shown for the bi-portal model in the constructive (blue solid) and the destructive case (blue dashed), in comparison to limits for a single light mediator case (black). For the bi-portal model the non-excluded parameter space is shaded. Resolution and threshold of the experiment are considered in the calculation.

predicted number of events increases. For mediator masses under 10 MeV the limits start to flatten. This is the mediator mass regime for which $m_{Z_l'} < q^2 = 2m_N E_R$ and the DM-nucleus scattering can be described by a long-range interaction. The momentum transfer is then the governing quantity in denominator of the mediator propagator and the mediator mass is expected to only have an impact at very low recoil energies for which $m_{Z_l'} \geq 2m_N E_R$. These low recoil energy events, however, are surmised to lie under the 1 keV threshold of COSINUS and thus should not affect the limits - this explains the flattening. Unexpectedly, the limits start to get stronger again for very low mediator masses. This behaviour can also be related to Figure 5.2, where we saw that the limits were stronger for lower values of $m_{Z_l'}$. By the above-mentioned reasoning, the limits in the two top panels in Figure 5.2 should be approximately on the same level of magnitude. The fact that low mediator masses have an impact on the limit is actually a consequence of the detector resolution included in the calculation. The light mediator mass dependence gets reintroduced by the convolution with the energy resolution. The precise mechanics of this are

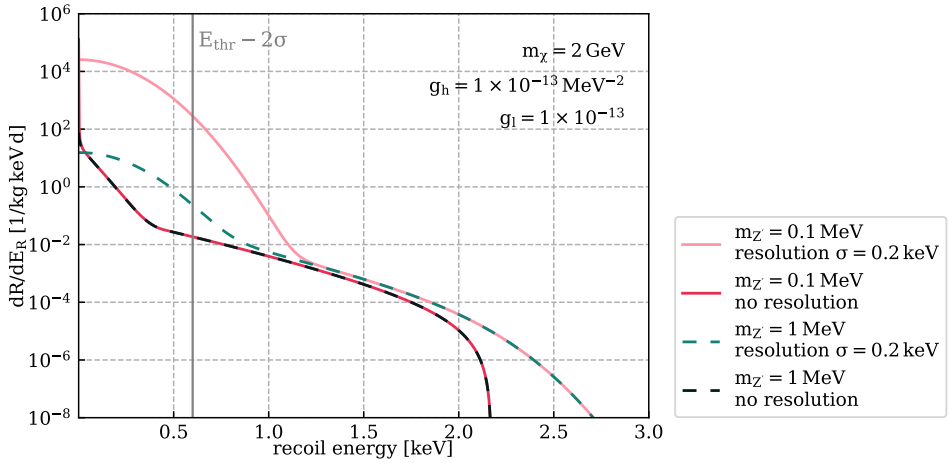

Figure 5.4: The nuclear recoil rate for constructive bi-portal models with light mediators of masses 0.1 MeV (solid) and 1 MeV (dashed) on a sodium iodide target. The DM particle has a mass of 2 GeV and the couplings are chosen in such a way, that they are compatible with the limits in the other plots shown in this chapter for COSINUS. This plot illustrates the resolution induced enhancement of the expected event rate for light mediators.

best explained by means of Figure 5.4, where recoil spectra on NaI are shown for 0.1 MeV and 1 MeV mediators in the bi-portal model, with and without resolution. In this plot one can see that the resolution shuffles events which are present close to zero recoil energy far over the threshold. Thus, the 0.1 MeV mediator spectrum is a significantly enhanced compared to the 1 MeV light mediator case if the resolution is considered. If the resolution is not considered, than the two spectra are very similar. In the top left panel limits are shown for the highest value of g_h analysed and the limits in the bi-portal model differ significantly from the single-light mediator limit. For the constructive case the limits are stronger than the single light mediator line line and the allowed region for g_l is only bounded from above, as in Figure 5.1. Independent of the mediator mass, only a very narrow band of values for g_l is allowed for the combination of DM mass and g_h displayed in this panel. This is can be explained with the same reasoning as for the upper panels of Figure 5.1: Due to the high coupling of the heavy mediator, a certain combination of m_χ and g_l can not be excluded unless the negative interference term in the matrix element reduces the overall rate significantly enough. The slim bad of allowed g_l in the destructive case is also compatible with the limit at $m_\chi = 10\,\mathrm{GeV}$ in the upper left panel of Figure 5.1. In the upper right panel the limit for the bi-portal model in the constructive case is similar to the one in the previous panel, scaled accordingly to the increase in g_h. For the destructive case the band-like structure can again be observed, with the band widening for lower and higher values of the mediator mass.

At very low $m_{Z_l'}$ around 0.1 MeV there is no lower limit on g_l in the destructive case, which is compatible with the limit in the upper left panel of Figure 5.2. At around 10 MeV mediator mass the band of allowed g_l values widens again, quite abruptly. This is also compatible with the limits in Figure 5.2, since the allowed span for g_l is smaller for the 1 MeV mediator than those for the 10 and 100 MeV mediators (i.e. compare top right with bottom panels). Since this abrupt change in the limit is consistent with the behaviour of limits calculated for the same sample with two separate, independent routines it is very unlikely to be a computational artefact. The next panel to analyse in Figure 5.3 is the bottom left with a heavy mediator coupling $g_h = 5 \times 10^{-14}\,\mathrm{MeV}^{-2}$. This lower value of g_h results in a less dominant heavy mediator in the bi-portal model and the light mediator coupling is thus only restricted from above in both the constructive and destructive case. Compared to the previous panel, both limits also start to draw near the single light mediator limit. In the bottom right panel the bi-portal limits then merge completely with the single mediator limit, as seen in the bottom right panel of Figure 5.1. Due to the low value of the heavy mediator coupling, the bi-portal model assumes its single light mediator limit.

In the next step the limits for the CRESST-III like background mock data are investigated. As mentioned above, the following limits were calculated without taking the detector's resolution into account, in the interest of reduced computation time. The overall behaviour of the limits is similar to the ones obtained for the COSINUS mock sample. In the following the analysis will thus not focus as much on the general behavior and the reasoning of such, but more on the differences between the CRESST-III and the COSINUS limits. Those differences stem from both the difference in target material, but also from other detector specific parameters like the threshold and resolution. In general, neglecting the resolution of the detector can lead to subtle changes in the behaviour of the limits which are demonstrated using an example at the end of this section.

In Figure 5.5 exclusion limits (95% CL) are shown in the $m_\chi - g_l$ plane with the light mediator mass fixed to 10 MeV. In each of the four panels the limits were calculated under assumption of different values for the effective heavy mediator coupling ranging from $5 \times 10^{-13}\,\mathrm{MeV}^{-2}$ down to $1 \times 10^{-14}\,\mathrm{MeV}^{-2}$. In each panel exclusion limits are shown for the constructive (solid line) and destructive case (dashed line) of the bi-portal model in magenta, together with an upper exclusion limit calculated for a single light mediator interaction (i.e. $g_h = 0$) in black. One

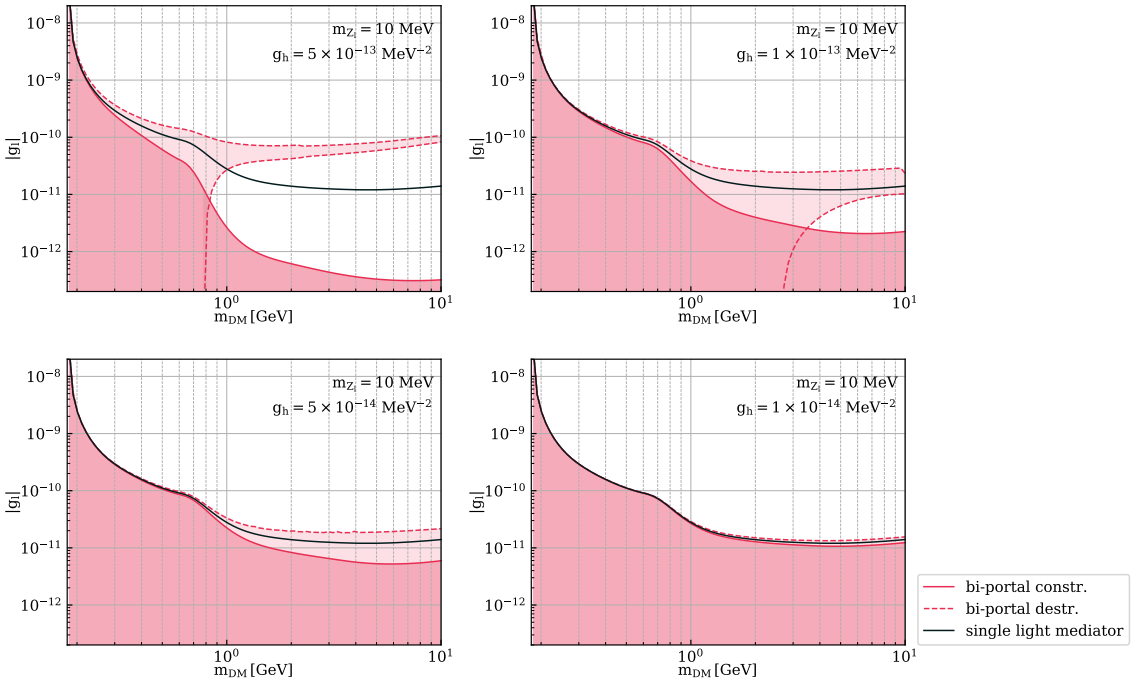

Figure 5.5: Exclusion limits (at 95% CL) on the light mediator coupling as a function of the DM mass for a CRESST-III like mock background sample. The light mediator mass is fixed and each panel shows limits for a different value of the effective heavy mediator coupling. Limits in magenta are for the bi-portal model in the constructive case (solid) and in the destructive case (dashed), in comparison to limits in black for a single light mediator case. For the bi-portal model the non-excluded parameter space is shaded. The threshold of the experiment is considered in the calculation but not the resolution.

can see that the general shape of the limits is similar to those for the COSINUS sample: For the higher values of g_h the bi-portal model limits differ largely from the single mediator limit and in the destructive case g_l is restricted both from above and below. For the lower values of g_h one can again observe that the bi-portal model limits start to merge with the single light mediator limit. However, the significantly lower threshold of the CRESST-III experiment enables probing DM masses down to less than 0.2 GeV. Furthermore, one can observe that the band-like behaviour of the destructive limits start to show for lower DM masses than in Figure 5.1. This can also be explained by the lower threshold, since interference effects appearing at low recoil energies can be taken into account. In each of the panels in Figure 5.5 there is a pronounced kink in the limit at around $m_\chi = 0.65\,\mathrm{GeV}$. This corresponds to the DM mass for which the tungsten dependent part of the recoil spectrum starts to lie above the threshold, i.e.

$$E_{R,\max}(m_\chi = 0.65\,\mathrm{GeV}) = \frac{2\mu_N^2 v^2}{m_N}\Big|_{N=W} > 0.031\,\mathrm{keV}. \tag{5.13}$$

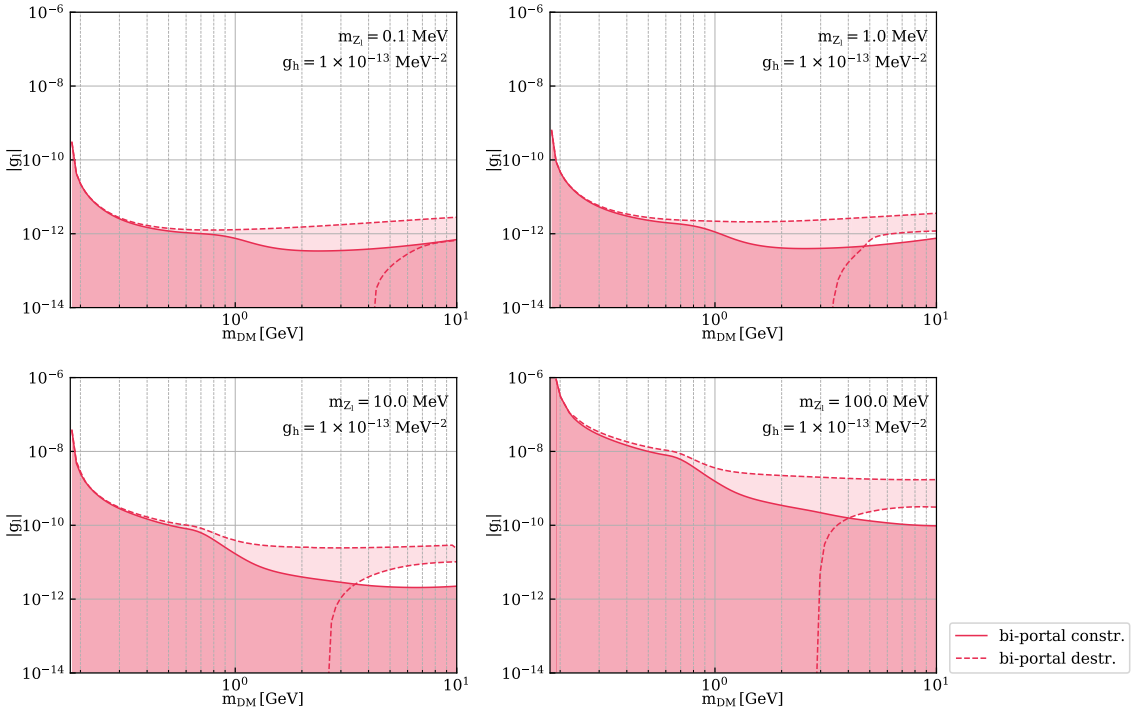

Figure 5.6: Exclusion limits (at 95% CL) on the light mediator coupling as a function of the DM mass for a CRESST-III like mock background sample. The effective heavy mediator coupling g_h is fixed at $1 \times 10^{-13}\,\mathrm{MeV}^{-2}$ and each panel shows the limits for a different value of the light mediator mass. Limits are shown for the bi-portal model in the constructive case (magenta solid) and in the destructive case (magenta dashed). The non-excluded parameters space is shaded respectively. The threshold of the experiment is considered in the calculation but not the resolution.

The limits for the CRESST-like mock sample in Figure 5.6 do largely resemble those for the COSINUS like sample in Figure 5.2. In Figure 5.6 exclusion limits (at 95% CL) for the CRESST-III mock background sample are shown in the $m_\chi - g_l$ plane, but this time the effective coupling of the heavy mediator is fixed, while in each panel $m_{Z_l'}$ varies. Only limits in the bi-portal model are shown and non-excluded regions are again shaded. As in the case of COSINUS, the limits on g_l increase with increasing mediator mass due to the inverse probability to $m_{Z_l'}$ in the matrix element calculation. However, the limits for the 0.1 MeV and 1 MeV mediator (top panels) are of almost equal strength. This is the first fundamental difference between the two experiments, as for COSINUS the limits for the 0.1 MeV mediator are almost two orders stronger, than the 1 MeV mediator limits (compare with Figure 5.2). As argued in the description of Figure 5.3, the behaviour of the CRESST limits, where the resolution is not considered, is actually what one would expect for light mediators were the momentum transfer becomes the governing quantity in the

interaction. The other fundamental difference between the two experiments is, that for the CRESST-III sample g_l is also restricted from below for the lightest mediator mass shown $m_{Z'_l} = 0.1$ MeV. As frequently stated in the above, very low mediator masses lead to high rates at low recoil energies. While the COSINUS experiment would not be sensitive to those events, the CRESST-III experiment is, due to its lower threshold. These additional events taken into account lead to the lower limit on g_l in the destructive case (i.e. with g_l too low the destructive interference term is not large enough to sufficiently suppress the rate).

Also for the CRESST-III mock background sample, the $m_{Z'_l} - g_l$-plane is being analysed. Limits in this plane for fixed DM mass and varying heavy mediator coupling are shown in Figure 5.7. The limits for the bi-portal constructive case (solid) and destructive case are displayed in magenta, together with a single light mediator limit in black. For the bi-portal model the non-excluded parameter space is shaded accordingly. The overall behaviour is again very similar to the limits for the COSINUS background sample: For higher values of g_h the limits on g_l in the constructive bi-portal model are significantly stronger than the single mediator model. On the contrary the destructive case limits are weaker and form band-like structures. For lower values of g_h the bi-portal limits merge with the single light mediator limit and also in the destructive case g_l is only restricted from above. Moreover, similar to Figure 5.3, in the upper right panel of Figure 5.7 the band of allowed values for g_l starts to widen for mediator masses larger than about 10 MeV. This is also consistent with the width of the bands in Figure 5.6. At $m_\chi = 10\,\mathrm{GeV}$ the band in the 100 MeV mediator panel is wider than the band at the same DM mass in the other panels. The most striking difference between the limits in the $m_{Z'_l} - g_l$ plane for the COSINUS-like and the CRESST-like samples is the general behaviour of the limits, in both the two mediator and single mediator case, at low mediator masses. While the limits on g_l tend to fall towards lower $m_{Z'_l}$ in Figure 5.3, in Figure 5.7 the limits start to flatten out for mediator masses lower than 1 MeV. As mentioned above, this flattening behavior is expected as the resolution of the detector was not taken into account and light mediator masses thus have next to no impact on the recoil spectra and the behaviour of the limits.

Some of the above-mentioned differences between the limits for COSINUS and CRESST-III could already be traced back to the fact that the resolution was not taken into account in the calculation for the CRESST-like limits. To further analyse the possible differences disregarding the resolution might cause, limits which were calculated with and without resolution for a CRESST-like mock background sample

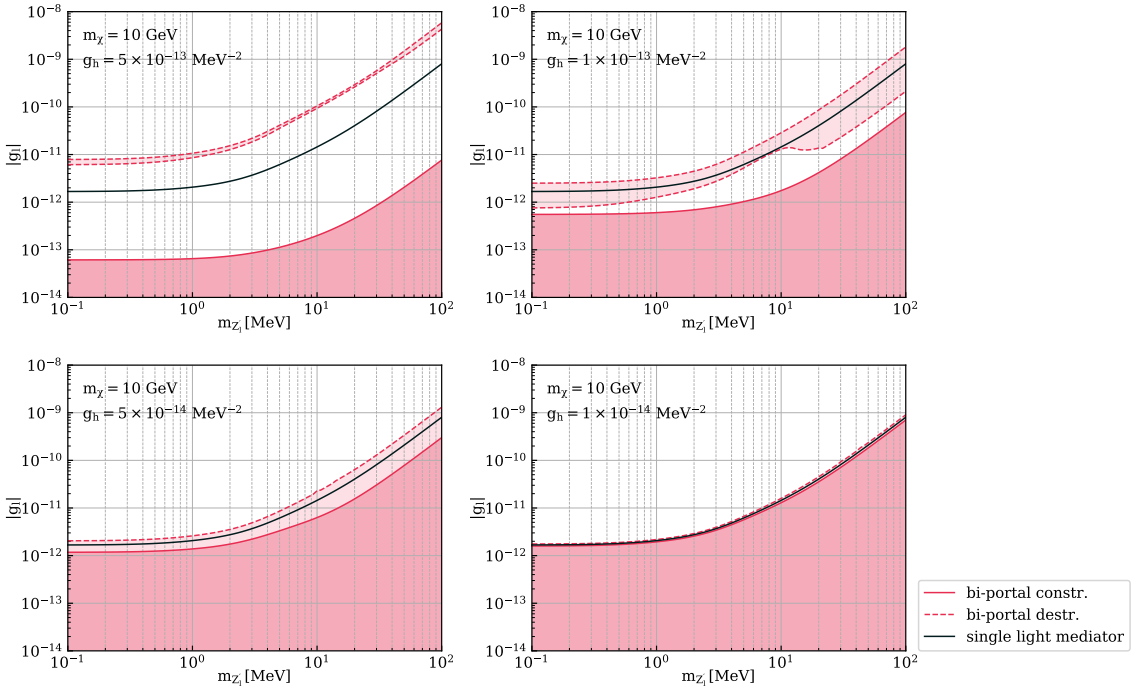

Figure 5.7: Exclusion limits (at 95% CL) on the light mediator coupling as a function of the light mediator mass for a COSINUS-like mock background sample. The DM mass is fixed at 10 GeV and each panel shows the limits for a different value of the heavy mediator coupling. Limits are shown for the bi-portal model in the constructive (magenta solid) and the destructive case (magenta dashed), in comparison to limits for a single light mediator case (black). For the bi-portal model the non-excluded parameter space is shaded. The threshold of the experiment is considered in the calculation, but not the resolution.

are shown in Figure 5.8. In the left panel the limits are for the constructive case of the bi-portal model, while in the right panel limits for the destructive case are shown. Limits calculated without resolution are displayed in magenta, those calculated with the resolution of $\sigma = 0.0046\,\text{keV}$ are displayed in green. The general impression is that when taking into account the resolution, the limits are smoothed out and irregularities, such as the kink around $m_\chi = 6.5$ GeV, are weakened in their shape. Moreover, the impact of the resolution is higher for lower DM masses (at least for *upper* exclusion limits), which is consistent with the statements made in the appendix, section B.2. The limits calculated with the resolution reach lower DM masses than those calculated without. This is due to the fact, that while in the calculation without resolution simulated events with a recoil energy lower than the threshold are rejected, in the calculation with resolution simulated events are rejected if their true deposited energy is lower than $E_{\text{thr}} - 2\sigma$. The most significant difference can be seen in the right panel for the destructive case. For higher DM masses the lower limit on g_l is significantly stricter, when being calculated without

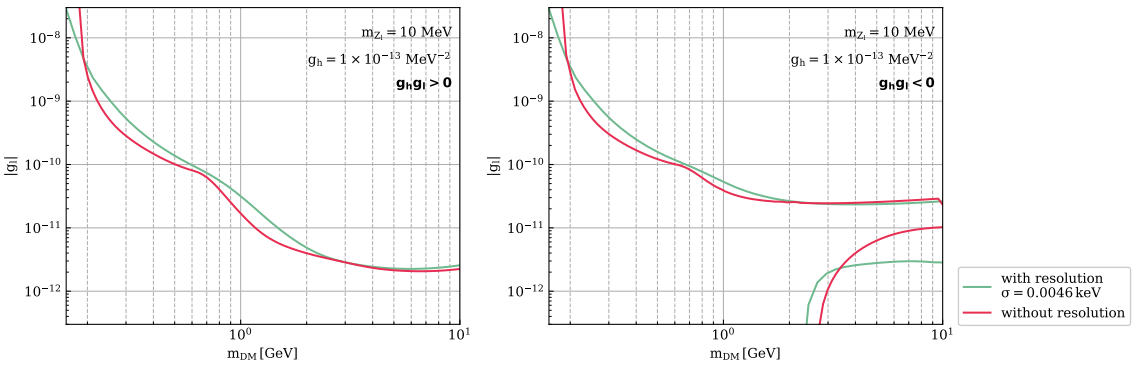

Figure 5.8: Exclusion limits (at 95% CL) in the bi-portal model on the light mediator coupling as a function of the DM mass for a CRESST-III like mock background sample. The DM mass is fixed at 10 GeV and the effective coupling of the heavy mediator at $1 \times 10^{-13}\,\mathrm{MeV}^{-2}$. The limits in green were calculated taking the resolution of the experiment into account, while in the calculation of the pink limits the resolution was neglected. In the left panel limits for the constructive case of the bi-portal model are shown, while in the right panel limits for the destructive case are displayed. The threshold of the experiments was also taken into account.

the resolution, i.e. the band between pink lines is narrower than the green band. When probing the destructive case one thus has to take care of the resolution, in order to not put too restrictive limits on the coupling of the light mediator.

To summarize, the preliminary calculation of limits described in the last section, showed that the bi-portal model does indeed yield novel shaped limits for various DM specific parameters. Due to the four free parameters of the model, limits could only be calculated in two parameters at the same time while fixing the other two. Nevertheless, the limits for a specific target in different planes are compatible with each other. As in the calculation of recoil spectra in chapter 3, also in the calculation of exclusion limits one can observe that for very high (low) values of g_h the bi-portal model assumes its marginal cases of single heavy (light) mediator interaction respectively.

Conclusion and outlook

The aim of this thesis was to investigate the implications of adding a second mediator particle to the DM-SM interaction, in particular in the context of DM direct detection. In the first chapter an overview of the evidence for DM and possible DM candidates was given. In addition, the three main approaches to DM detection were described. Moreover, the differential recoil spectrum was introduced as one of the most important tools to relate results from direct detection to theoretical DM interaction models.

The second chapter was dedicated to the precise analysis of the interaction process between SM nucleus and DM particle in a direct detection experiment. In the first half of this chapter the DM scattering of nuclei via different types of mediators was investigated, restricting ourselves to spin-independent interaction models. Throughout this section it became apparent, that one has to distinguish between a heavy ($q^2 \ll m_{\phi'}^2$) and a light mediator case ($q^2 \geq m_{\phi'}^2$) in the calculation of cross sections. This necessary distinction was then illustrated by comparison of recoil spectra for the two different cases. The concepts established in the first half of chapter two were then extended in the second half by adding a second mediator to the interaction. In the bi-portal model the interaction is then mediated by one heavy and one light particle and the simplified Lagrangian of the theory is given by the sum of the two single mediator Lagrangians. The cross sections were then calculated for two combinations of mediators: first for two vector mediators of different mass and then for a combination of a heavy scalar and a lighter vector mediator. In the calculation of the squared matrix element an interference term arises, which suggests a subdivision of the bi-portal model in two cases. For a combination of couplings which brings forth a positive interference term we speak of the constructive interference case, otherwise of a destructive interference case. A fist analysis of recoil spectra generated from the two mediator model showed, that both constructive and destructive case lead to spectra which are distinguishable from single-mediator cases. While the differences for the constructive case are rather subtle, a negative interference term

can lead to prominent dips and kinks in the recoil spectra. Moreover it was shown that, while interference effects appear for various target materials, their shapes and positions vary strongly between different targets. In the last part of chapter 2 it was argued both through calculation and graphically, that we can restrict ourselves to the combination of two spin-1 mediators in the rest of the analysis.

With the bi-portal model being the centerpiece of this work, the third chapter was devoted entirely to a detailed analysis of the recoil spectra it predicts for a sodium iodide target. For both the constructive and destructive case, the differential recoil rates were scrutinized regarding their behaviour under change of various model parameters, like masses and couplings. It was shown, that interference effects are present throughout various DM and mediator masses. However, they disappear if the mass of the light vector mediator becomes too large. Moreover, the position and depth of the destructive interference effects are sensitive to small variations of the couplings. The analysis also demonstrated, that if the coupling of one mediator significantly exceeds the other mediator's coupling the interaction is only mediated by the stronger coupled particle. In this way the bi-portal model can assume a single light or a single heavy mediator limit. Most importantly, it was shown at the end of chapter three, that probing the signatures of the bi-portal model with mediator mass hierarchy is at reach for current experiments with a high enough resolution.

So far direct detection experiments have not published any unchallenged excess, which the bi-portal model could be compared against. Thus, the impact of low threshold experiments on the exclusions obtained for bi-portal models was also investigated. The necessary concepts and methods used in order to find exclusion limits from a maximum likelihood approach are described in chapter 4 and the first half of chapter 5. Indeed, the exclusion limits from COSINUS- and CRESST-III like mock samples for the bi-portal model differ significantly from the compared single light mediator limit. One of the most interesting behaviours is observed for the destructive bi-portal case, where, for a fixed heavy mediator coupling, the coupling of the light mediator can be restricted both from above and below for certain DM masses. Moreover, the investigated limits in the light mediator mass - light mediator coupling plane, also showed behaviour different from the single light mediator case.

A next possible step in the analysis of the bi-portal model could be to improve this limit calculation. An upgrade could focus both on the computational aspects of the minimization, as well as on the inclusion of nuisance parameters. Possible variables which could be included as nuisance parameters are the DM density, the galactic escape velocity and other astrophysical as well as detector specific quantities.

The next logical step is also to do the analysis with real experimental data instead of mock background samples. Moreover, another refinement could be a parallel study of different materials and experiments, i.e. calculating limits based not only on data from one, but a combination of several experiments.

The found exclusion limits in $m_{Z_l'} - g_l$ plane suggest another possible extension of this work, namely the comparison with limits in this plane from collider experiments. However, one has to be very careful when attempting this comparison due to several reasons. First of all, the majority of the particle physics calculation used in the generation of this work's exclusion limits was done in a low-energy limit. Many simplifications used, like integrating out the heavy mediator, are thus not applicable for collider searches. Moreover, the axial-vector contribution to the Lagrangian which was neglected in this work, might be of significant impact on the cross sections relevant for DM production in the collider.

Finally, there is another concept which should be looked into, in order to attest the bi-portal model as a viable DM-SM interaction mechanism. In the first chapter of this thesis it was stressed, that a viable DM candidate has to be able to explain the DM relic density measured in the Universe today. Since the relic density depends on the DM annihilation cross-section, the precise DM-SM interaction process plays into the calculation. One thus has to check, if an interaction model with two spin-1 mediators leads to a compatible DM relic density and for which span of DM and mediator masses. If the bi-portal model does indeed predict the right relic density, nothing stands in the way of further testing of the model, also with real data from direct detection experiments.

Within this thesis, we have thus shown that bi-portal models with hierarchy in mediator masses offer a rich phenomenology. To this end, we constructed simplified Lagrangians and studied their effect in the context of direct detection experiments. We showed a possible range of mediator masses and couplings where the limits from bi-portal models significantly differ from single mediator models. We furthermore identified several other unexplored aspects of phenomenology, which will be the subject of future work.

Appendix A

Particle Physics

A.1 Recoil energy and minimum velocity

In order to calculate the velocity integral in the differential recoil spectrum the minimum velocity $v_{\min}$ of a WIMP, that can induce a nuclear recoil of energy E_R, is needed. For this calculation it is advantageous to first find an expression for the recoil energy $E_R = \frac{q^2}{2m_N}$ produced in the scattering process in terms of the scattering angle and the WIMP velocity. The calculation is done in the center of mass (COM) frame sketched in Figure A.1 and the NR limit is considered. With the nucleus at rest and the incoming DM particle velocity $\vec{v}$ in the lab frame, the initial three-momenta in the COM frame are

$$\vec{k}_{\text{COM}} = -m_N \vec{v}_{\text{COM}} \tag{A.1}$$

$$\vec{p}_{\text{COM}} = m_\chi \vec{v} - \vec{v}_{\text{COM}} = m_N \vec{v}_{\text{COM}}. \tag{A.2}$$

In the above v_{COM} denotes the COM velocity which is given by

$$\vec{v}_{\text{COM}} = \frac{m_\chi \vec{v} + m_N \cdot 0}{m_\chi + m_N} = \frac{\mu_N \vec{v}}{m_N}. \tag{A.3}$$

with μ_N denoting the reduced DM-nucleus mass.

The definition of the momentum transfer $\vec{q} = \vec{p} - \vec{p'} = \vec{k'} - \vec{k}$ can be used in order to find the final momenta in the COM frame:

$$\vec{k'}_{\text{COM}} = \vec{q} + \vec{k} = q - \mu_N \vec{v} \tag{A.4}$$

$$\vec{p'}_{\text{COM}} = \vec{p} - \vec{q} = \mu_N \vec{v} - q = -\vec{k'}_{\text{COM}} \tag{A.5}$$

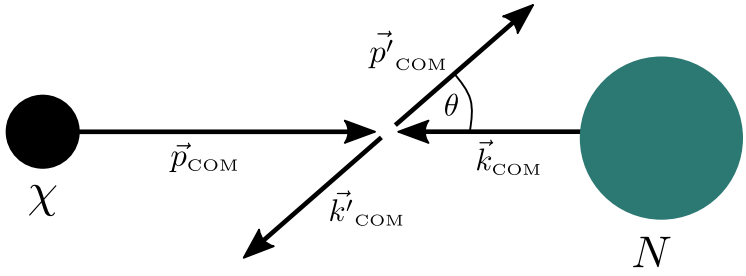

Figure A.1: Sketch of the DM-nucleus scattering in the COM frame.

From the above definitions of the momenta, together with momentum conservation $|\vec{p}|+|\vec{k}| = |\vec{p'}|+|\vec{k'}|$, one can deduce that $|\vec{p}| = |\vec{p'}|$. The squared momentum transfer as a function of the scattering angle θ in the COM frame is thus given by

$$\begin{aligned} |q|^2 &= |\vec{p} - \vec{p'}|^2 \\ &= 2(|\vec{p}|^2 - \vec{p}\cdot\vec{p'}) \\ &= 2|\vec{p}|^2(1-\cos\theta) \\ &= 2\mu_N^2 v^2(1-\cos\theta) \end{aligned} \tag{A.6}$$

Equation (A.6) can be used to find an expression for the recoil energy and maximization in θ gives an upper bound on E_R:

$$E_R = \frac{q^2}{2m_N} = \frac{\mu_N^2 v^2}{m_N}(1-\cos\theta) \leq \frac{2\mu_N^2 v^2}{m_N} \tag{A.7}$$

The minimum velocity with which a WIMP has to enter the detector in order to produce a nuclear recoil of energy E_R is thus given by

$$v_{\mathrm{min}} = \sqrt{\frac{m_N E_R}{2\mu_N^2}}, \tag{A.8}$$

and depends both on the target nucleus and the DM particle mass.

A.2 NR Dirac spinors

In this section useful spinor identities in the non-relativistic limit are calculated. The Weyl basis is chosen for the gamma matrices γ^μ, γ^5 following the book by Peskin and Schroeder [55]. In the NR limit the time-component of a four momentum p is approximately the mass of the particle $p^0 \approx m$. Thus

$$\sqrt{p \cdot \sigma} \approx \sqrt{m - \vec{p} \cdot \vec{\sigma}} \approx \sqrt{m} \left(1 - \frac{\vec{p} \cdot \vec{\sigma}}{2m}\right) \tag{A.9}$$

$$\sqrt{p \cdot \overline{\sigma}} \approx \sqrt{m + \vec{p} \cdot \vec{\sigma}} \approx \sqrt{m} \left(1 + \frac{\vec{p} \cdot \vec{\sigma}}{2m}\right), \tag{A.10}$$

using a Taylor expansion in the last step. The independent spinor solutions u, v to the Dirac equation then reduce to

$$u_s(p) = \begin{pmatrix} \sqrt{p \cdot \sigma}\xi_s \\ \sqrt{p \cdot \overline{\sigma}}\xi_s \end{pmatrix} \xrightarrow{\text{NR}} \sqrt{m} \begin{pmatrix} \left(1 - \frac{\vec{p} \cdot \vec{\sigma}}{2m}\right)\xi_s \\ \left(1 + \frac{\vec{p} \cdot \vec{\sigma}}{2m}\right)\xi_s \end{pmatrix} \tag{A.11}$$

$$v_s(p) = \begin{pmatrix} \sqrt{p \cdot \sigma}\xi_s \\ -\sqrt{p \cdot \overline{\sigma}}\xi_s \end{pmatrix} \xrightarrow{\text{NR}} \sqrt{m} \begin{pmatrix} \left(1 - \frac{\vec{p} \cdot \vec{\sigma}}{2m}\right)\xi_s \\ -\left(1 + \frac{\vec{p} \cdot \vec{\sigma}}{2m}\right)\xi_s \end{pmatrix}. \tag{A.12}$$

In the calculation of the matrix element for DM-nucleus scattering mediated by a scalar particle, terms of the form $\overline{u}_{s'}(p')u_s(p)$ are needed:

$$\begin{aligned}
\overline{u}_{s'}(p')u_s(p) &= u^\dagger_{s'}(p')\gamma^0 u_s(p) \\
&= \sqrt{m} \begin{pmatrix} \left(1 - \frac{\vec{p'} \cdot \vec{\sigma}}{2m}\right)\xi_{s'} \\ \left(1 + \frac{\vec{p'} \cdot \vec{\sigma}}{2m}\right)\xi_{s'} \end{pmatrix}^\dagger \begin{pmatrix} 0 & \mathbb{1}_2 \\ \mathbb{1}_2 & 0 \end{pmatrix} \sqrt{m} \begin{pmatrix} \left(1 - \frac{\vec{p} \cdot \vec{\sigma}}{2m}\right)\xi_s \\ \left(1 + \frac{\vec{p} \cdot \vec{\sigma}}{2m}\right)\xi_s \end{pmatrix} \\
&= m \begin{pmatrix} \left(1 + \frac{\vec{p'} \cdot \vec{\sigma}}{2m}\right)\xi^\dagger_{s'} & \left(1 - \frac{\vec{p'} \cdot \vec{\sigma}}{2m}\right)\xi^\dagger_{s'} \end{pmatrix} \cdot \begin{pmatrix} \left(1 - \frac{\vec{p} \cdot \vec{\sigma}}{2m}\right)\xi_s \\ \left(1 + \frac{\vec{p} \cdot \vec{\sigma}}{2m}\right)\xi_s \end{pmatrix} \\
&= m \left(1 - \frac{\vec{p} \cdot \vec{\sigma}}{2m} + \frac{\vec{p'} \cdot \vec{\sigma}}{2m} - \frac{\vec{p'} \cdot \vec{p} \cdot \vec{\sigma}^2}{4m^2} + 1 + \frac{\vec{p} \cdot \vec{\sigma}}{2m} - \frac{\vec{p'} \cdot \vec{\sigma}}{2m} - \frac{\vec{p'} \cdot \vec{p} \cdot \vec{\sigma}^2}{4m^2}\right) \xi^\dagger_{s'}\xi_s \\
&\approx 2m\xi^\dagger_{s'}\xi_s
\end{aligned} \tag{A.13}$$

The calculation for a vector mediator is quite similar, but one has to perform a distinction of cases for temporal and spatial components of the γ^μ matrix involved:

$$
\begin{aligned}
\overline{u}_{s'}(p')\gamma^\mu u_s(p) &= u^\dagger_{s'}(p')\gamma^0\gamma^\mu u_s(p) \\
&= \sqrt{m}\begin{pmatrix}\left(1-\frac{\vec{p'}\cdot\vec{\sigma}}{2m}\right)\xi_{s'}\\ \left(1+\frac{\vec{p'}\cdot\vec{\sigma}}{2m}\right)\xi_{s'}\end{pmatrix}^\dagger \begin{pmatrix}0 & \mathbb{1}_2\\ \mathbb{1}_2 & 0\end{pmatrix}\begin{pmatrix}0 & \sigma^\mu\\ \overline{\sigma}^\mu & 0\end{pmatrix}\sqrt{m}\begin{pmatrix}\left(1-\frac{\vec{p}\cdot\vec{\sigma}}{2m}\right)\xi_s\\ \left(1+\frac{\vec{p}\cdot\vec{\sigma}}{2m}\right)\xi_s\end{pmatrix} \\
\underline{\mu=0:}\quad &= m\begin{pmatrix}\left(1-\frac{\vec{p'}\cdot\vec{\sigma}}{2m}\right)\xi_{s'}\\ \left(1+\frac{\vec{p'}\cdot\vec{\sigma}}{2m}\right)\xi_{s'}\end{pmatrix}^\dagger \begin{pmatrix}0 & \mathbb{1}_2\\ \mathbb{1}_2 & 0\end{pmatrix}\begin{pmatrix}0 & \mathbb{1}_2\\ \mathbb{1}_2 & 0\end{pmatrix}\begin{pmatrix}\left(1-\frac{\vec{p}\cdot\vec{\sigma}}{2m}\right)\xi_s\\ \left(1+\frac{\vec{p}\cdot\vec{\sigma}}{2m}\right)\xi_s\end{pmatrix} \\
&= m\begin{pmatrix}\left(1-\frac{\vec{p'}\cdot\vec{\sigma}}{2m}\right)\xi^\dagger_{s'} & \left(1+\frac{\vec{p'}\cdot\vec{\sigma}}{2m}\right)\xi^\dagger_{s'}\end{pmatrix}\begin{pmatrix}\mathbb{1}_2 & 0\\ 0 & \mathbb{1}_2\end{pmatrix}\begin{pmatrix}\left(1-\frac{\vec{p}\cdot\vec{\sigma}}{2m}\right)\xi_s\\ \left(1+\frac{\vec{p}\cdot\vec{\sigma}}{2m}\right)\xi_s\end{pmatrix} \\
&\approx 2m\xi^\dagger_{s'}\xi_s \\
\underline{\mu=k:}\quad &= \sqrt{m}\begin{pmatrix}\left(1-\frac{\vec{p'}\cdot\vec{\sigma}}{2m}\right)\xi_{s'}\\ \left(1+\frac{\vec{p'}\cdot\vec{\sigma}}{2m}\right)\xi_{s'}\end{pmatrix}^\dagger \begin{pmatrix}0 & \mathbb{1}_2\\ \mathbb{1}_2 & 0\end{pmatrix}\begin{pmatrix}0 & \sigma^k\\ -\sigma^k & 0\end{pmatrix}\begin{pmatrix}\left(1-\frac{\vec{p}\cdot\vec{\sigma}}{2m}\right)\xi_s\\ \left(1+\frac{\vec{p}\cdot\vec{\sigma}}{2m}\right)\xi_s\end{pmatrix} \\
&= m\begin{pmatrix}\left(1-\frac{\vec{p'}\cdot\vec{\sigma}}{2m}\right)\xi_{s'}\\ \left(1+\frac{\vec{p'}\cdot\vec{\sigma}}{2m}\right)\xi_{s'}\end{pmatrix}^\dagger \begin{pmatrix}-\sigma^k & 0\\ 0 & \sigma^k\end{pmatrix}\begin{pmatrix}\left(1-\frac{\vec{p}\cdot\vec{\sigma}}{2m}\right)\xi_s\\ \left(1+\frac{\vec{p}\cdot\vec{\sigma}}{2m}\right)\xi_s\end{pmatrix} \\
&= m\begin{pmatrix}-\left(1-\frac{\vec{p'}\cdot\vec{\sigma}}{2m}\right)\sigma^k\xi^\dagger_{s'} & \left(1+\frac{\vec{p'}\cdot\vec{\sigma}}{2m}\right)\sigma^k\xi^\dagger_{s'}\end{pmatrix}\begin{pmatrix}\left(1-\frac{\vec{p}\cdot\vec{\sigma}}{2m}\right)\xi_s\\ \left(1+\frac{\vec{p}\cdot\vec{\sigma}}{2m}\right)\xi_s\end{pmatrix} \\
&= 0 \\
\overline{u}_{s'}(p')\gamma^\mu u_s(p) &= 2m\xi^\dagger_{s'}\xi_s\delta^{0\mu}
\end{aligned}
\tag{A.14}
$$

For completeness we also have a look at the axial scalar case:

$$
\begin{aligned}
\overline{u}_{s'}\gamma^5(p')u_s(p) &= u^\dagger_{s'}(p')\gamma^0\gamma^5 u_s(p) \\
&= \sqrt{m}\begin{pmatrix}\left(1-\frac{\vec{p'}\cdot\vec{\sigma}}{2m}\right)\xi_{s'}\\ \left(1+\frac{\vec{p'}\cdot\vec{\sigma}}{2m}\right)\xi_{s'}\end{pmatrix}^\dagger \begin{pmatrix}0 & \mathbb{1}_2\\ \mathbb{1}_2 & 0\end{pmatrix}\begin{pmatrix}-\mathbb{1}_2 & 0\\ 0 & \mathbb{1}_2\end{pmatrix}\sqrt{m}\begin{pmatrix}\left(1-\frac{\vec{p}\cdot\vec{\sigma}}{2m}\right)\xi_s\\ \left(1+\frac{\vec{p}\cdot\vec{\sigma}}{2m}\right)\xi_s\end{pmatrix} \\
&= m\begin{pmatrix}-\left(1+\frac{\vec{p'}\cdot\vec{\sigma}}{2m}\right)\xi^\dagger_{s'} & \left(1-\frac{\vec{p'}\cdot\vec{\sigma}}{2m}\right)\xi^\dagger_{s'}\end{pmatrix}\cdot\begin{pmatrix}\left(1-\frac{\vec{p}\cdot\vec{\sigma}}{2m}\right)\xi_s\\ \left(1+\frac{\vec{p}\cdot\vec{\sigma}}{2m}\right)\xi_s\end{pmatrix} \\
&= m\left(-1+\frac{\vec{p}\cdot\vec{\sigma}}{2m}-\frac{\vec{p'}\cdot\vec{\sigma}}{2m}+\frac{\vec{p'}\cdot\vec{p}\cdot\vec{\sigma}^2}{4m^2}+1+\frac{\vec{p}\cdot\vec{\sigma}}{2m}-\frac{\vec{p'}\cdot\vec{\sigma}}{2m}-\frac{\vec{p'}\cdot\vec{p}\cdot\vec{\sigma}^2}{4m^2}\right)\xi^\dagger_{s'}\xi_s \\
&= (\vec{p'}-\vec{p})\cdot\vec{\sigma}\xi^\dagger_{s'}\xi_s
\end{aligned}
\tag{A.15}
$$

If $u_s, u_{s'}$ are spinors for the DM Dirac fermion the above expression amounts to $\overline{u}_{s'}\gamma^5(p')u_s(p) = -\vec{q}\cdot\vec{s}_\chi$ and the NR scattering amplitude is thus proportional to the momentum transfer. Also for the axial-vector and axial-scalar case dependencies on the momentum transfer or the incoming DM velocity appear in the NR scattering amplitude. This behaviour is consistent with the NR operators in Table 2.1. Interactions with axial type mediators are not further investigated in this work.

A.3 Conversion factor for the nuclear recoil rate

For DM direct detection experiments the nuclear recoil rate is usually given events per kg target material per keV recoil energy per days exposure. Since many of the parts used within the calculation of the recoil spectra are deduced in natural units, one has to find an appropriate conversion factor. The nuclear recoil rate is of the form

$$\frac{dR}{dE_R} = \frac{\rho_\chi}{2\pi m_\chi} g^2_{\text{tot}}(E_R) F^2(E_R) \underbrace{\int_{v_{min}}^{v_{max}} dv \, \frac{f(\bar{v})}{v}}_{I_{v_{min}}} \tag{A.16}$$

with g^2_{tot} depending on the DM-nucleus interaction model according to Table A.1. All couplings $g_{h'}$, $g_{Z'}$, g_h, g_l in Table A.1 dimensionless (here g_h is not an effective coupling), mediator masses are usually given in MeV and the DM particle mass in GeV. The various quantities are thus inserted in the recoil spectrum calculation with the following units:

$$\left[\rho_\chi\right] = \frac{\text{GeV}}{c^2\text{cm}^3}, \qquad \left[m_\chi\right] = \frac{\text{GeV}}{c^2}, \qquad \left[F^2(E_R)\right] = 1$$
$$\left[I_{v_{min}}\right] = \frac{s}{\text{km}}, \qquad \left[g^2_{tot}\right] = \frac{c^8}{\text{MeV}^4}$$

The calculation of the conversion factor is performed in natural units ($c = \hbar = G = k_B = 1$)). Let us define the following constants $\boldsymbol{c} \coloneqq 299\,792\,458$, $\boldsymbol{\hbar} \coloneqq 6.582\,119\,569 \times 10^{-16}$ and $\boldsymbol{e} \coloneqq 1.602\,176\,634 \times 10^{-19}$ representing the numerical values of the speed of light in $\text{m}\,\text{s}^{-1}$, the reduced Planck constant in $\text{eV}\,\text{s}$ and the electron charge magnitude in C [31].

Table A.1: g_{tot} for various DM-nucleus interaction models as described in chapter 2.

interaction model	g_{tot}
single scalar mediator h'	$G(m_{h'}, E_R) g_{h'} [Z \cos\vartheta + (A - Z) \sin\vartheta]$
single vector mediator Z'	$3A, G(m_{Z'}, E_R) g_{Z'}$
bi-portal model Z'_h, Z'_l	$3A \left[\frac{g_h}{m^2_{Z'_h}} + \frac{g_l}{m^2_{Z'_l} + q^2} \right]$

In a first step the unit of the differential recoil rate is rewritten in terms of eV

$$\begin{aligned} \left[\frac{dR}{dE_R} \right] &= \frac{\frac{\text{GeV}}{\text{cm}^3}}{\text{GeV}} \frac{1}{\text{MeV}^4} \frac{\text{s}}{\text{km}} \\ &= 10^{-21} \frac{s}{\text{m}^4 \, \text{eV}^4} \end{aligned} \tag{A.17}$$

using $1\,\text{s} = \boldsymbol{\hbar}^{-1}\,\text{eV}^{-1}$ and $1\,\text{m}^{-1} = \boldsymbol{\hbar c}\,\text{eV}$:

$$= \boldsymbol{\hbar}^3 \boldsymbol{c}^4 \times 10^{-21} \frac{1}{\text{eV}} \tag{A.18}$$

In the next step another conversion is needed in order to regain the units of seconds and kg:

$$1 = 1\,\text{eV} \times \frac{1}{1\,\text{eV}} = \boldsymbol{\hbar}\,\text{s} \times \frac{\boldsymbol{e}}{\boldsymbol{c}^2}\,\text{kg} \tag{A.19}$$

This leads to

$$\left[\frac{dR}{dE_R} \right] = \frac{\boldsymbol{\hbar}^2 \boldsymbol{c}^6}{\boldsymbol{e}} \times 10^{-21} \frac{1}{\text{kg}\,\text{s}\,\text{eV}} \tag{A.20}$$

and in a final step one converts seconds to days and eV to keV:

$$\begin{aligned} &= 86400 \times \frac{\boldsymbol{\hbar}^2 \boldsymbol{c}^6}{\boldsymbol{e}} \times 10^{-18} \frac{1}{\text{kg}\,\text{d}\,\text{keV}} \\ &\approx 1.696 \times 10^{26} \frac{1}{\text{kg}\,\text{d}\,\text{keV}} \end{aligned} \tag{A.21}$$

A.4 Estimates for the couplings g from DM direct detection limits

In order to estimate the size of the couplings g_l, g_h defined in chapter 2 for light and heavy mediators, differential recoil rates computed from cross section (2.32) are compared to recoil rates originating from the spin-independent nucleon-DM reference cross section (2.36). For the calculation a value of the nucleon cross section of $\sigma_n = 1 \times 10^{-8}\,\text{pb} = 1 \times 10^{-44}\,\text{cm}^2$ is used, which is comparable to the limits published in 2016 by the XENON100 [89] and LUX [90] experiments for a 10 GeV DM particle. More recently published results give more stringent upper limits on the cross section in this DM mass scale, for example from the XENON1T experiment [15]. The chosen value for σ_n and the resulting approximation of the couplings thus might result in an over-prediction of expected events, but it is still gives a good first estimate.

In Figure A.2 (a) the comparison for a light vector mediator exchange shows that $g_l = 1 \times 10^{-12}$ is an appropriate choice for this coupling for a 10 GeV DM particle. For the heavy mediator case displayed in Figure A.2 (b) a coupling of $g_h = 1 \times 10^{-10}$ gives a comparable rate to the one resulting from the reference cross section. The heavy coupling thus has to be 2 orders higher than the equivalent light coupling for fixed DM mass and σ_n. This is due to the mediator mass dependence in the matrix element in (2.32), which for a 10 MeV and 100 MeV mediator results in a scaling factor of precisely $10^2 = (m_{Z'_l}/m_{Z'_h})^2$.

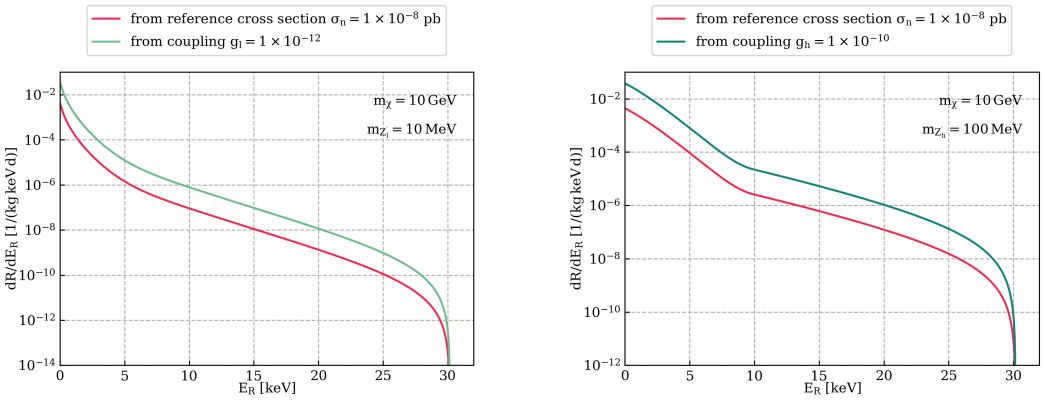

(a) (b)

Figure A.2: Differential recoil rate for interaction via a 10 MeV light vector mediator (a) and a 100 MeV heavy vector mediator (b) on a sodium iodide target. The spectra in green and blue were calculated using equation (2.32) and the spectra in magenta were calculated from equation (2.36).

Appendix B

Computational remarks

B.1 Generating mock data

Exclusion limits on certain parameters of DM-SM interaction models can be either calculated from real experimental data or in case of this work from a mock sample. For exclusion limits one assumes that no DM signal was observed and the measurements made were strictly from background events. Therefore, the mock data sample has to be drawn only from the distribution of the background and the signal is not considered. For a flat background, as assumed for some DM direct detection experiments, the background can thus be generated using the uniform random number generator provided by the numpy [91] package. For a linear falling background the triangular random number generator can be used.

However, the procedure is more complicated if the resolution of the detector is taken into account. The background sample can then not be generated with a random number generator available in some python package but the so called inverse transform method has to be used. This is a method which can be applied when the background distribution is one-dimensional. The method uses the cumulative distribution function (CDF), which can be expressed as the integral of the probability density function $f(x)$:

$$F(x) = \int_{-\infty}^{x} f(t)dt \tag{B.1}$$

The inverse of the CDF $F(x)$ is then defined by [92]

$$F^{-1}(u) = \inf\{x \in \mathbb{R} | F(x) \geq u\} \tag{B.2}$$

for all $u \in (0, 1)$. If F is a bijective function, F^{-1} is just the usual inverse and the

inverse transform method can be applied directly.

In the case of drawing from a background sample convoluted with a Gaussian resolution, evaluation the CDF and its inverse can not be directly done. Instead the generation of background events follows the subsequent procedure:

1. For a certain background model the expected total number of events N_b is calculated taking threshold, resolution and exposure ε of the experiment into account. The probability density function is then $f(E_R) = (\varepsilon \frac{dR_b}{dE_R})/N_b$.

2. For an array of recoil energies $\mathbf{E} = [E_{R_i}, \dots E_{R_n}]$ the CDF $F(E_R)$ is calculated using numerical integration. The energy values in the array are evenly spread from the experimental threshold to the upper limit of the region of interest. This array has to be large enough in order to get a correctly distributed sample - in this work $n \approx 1 \times 10^5$.

3. From a Poissonian distribution of mean N_b a number $N_{b,\mathrm{rand}}$ is drawn.

4. $N_{b,\mathrm{rand}}$ random numbers u are drawn from a uniform distribution .

5. To each u an element of the energy array is matched, such that

$$F^1(u) = \inf\{E_R \in \mathbf{E} | F(E_R) \geq u\}.$$

   The array of matched energies is then the random sample.

B.2 Detector resolution and low DM masses

In a direct detection experiment, the detector is only sensitive to DM masses for which the maximum deposited recoil energy is higher than the threshold. The maximum recoil energy a DM particle of mass m_χ can deposit in a target material of nuclear mass m_N is given by the maximum of equation (A.7)

$$E_{R,\max}(m_\chi) = \frac{2\mu_N^2 v^2}{m_N}. \tag{B.3}$$

Due to inverse proportionality in m_N, the maximum recoil energy for composite targets is calculated using the nuclear mass of the lightest component.

Whenever the resolution of an experiment is considered, the convolution with the Gaussian distribution of σ results in a falsification of the maximum recoil energy. This effect is especially significant for very light DM particles with masses $m_\chi \leq 1$ GeV. In Figure B.1 this effect is shown on a sodium iodide target for a 0.6 keV DM

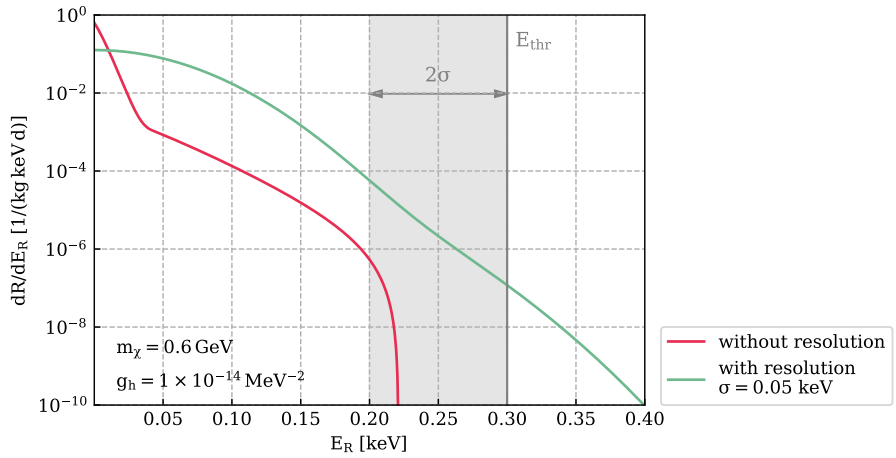

Figure B.1: NRS on sodium iodide for a 0.6 GeV DM particle interacting with the SM via a single heavy vector mediator. The graphic illustrates how the energy resolution of a detector can shuffle predicted events over the threshold.

particle which interacts with the SM via one heavy vector mediator. For the recoil spectrum in magenta no detector resolution was considered, resulting in a maximum recoil energy of 0.221 keV lower than the threshold of $E_{\text{thr}} = 0.3$ keV. The spectrum in green was calculated assuming a Gaussian energy resolution of $\sigma = 0.05$. For the same mass the spectrum in green predicts events above the threshold. Thus low DM masses may be considered in the analysis to which the detector is actually not sensitive. In order to avoid this, simulated events with a true (reconstructed) energy smaller than $E_{\text{thr}} - 2\sigma$ are rejected, similar to the procedure used in the analysis of CRESST-III data [14]. For the example in Figure B.1 this implies that a DM mass of 0.6 keV would still be included in the ML exclusion limit analysis. It should be noted here, that the choice of two sigma made by the CRESST group is rather conservative in comparison to the choice of three sigma used in other experiments.

B.3 Minimization process

In the calculation of exclusion limits with a maximum likelihood approach, as described in chapter 4, the negative log-likelihood function has to be minimised in several steps. Although no nuisance parameters are involved in the analysis and the available parameter space for the analysis is thus rather small, the minimisation procedure has to be handled with care. The biggest problem lies within the fact, that due to the complexity of the problem the likelihood function might have more than local one minimum. Especially when fitting one or both couplings, there may

be multiple combinations for which a high likelihood is achieved. In order to achieve a global minimization an algorithm similar to the Basin-Hopping algorithm was created. The Basin-Hopping method was initially used to find minima in the energy structure of Lennard-Jones potentials for cluster containing a high number of atoms [93]. In the modified version no starting value is needed, instead various starting points are randomly distributed over the parameter space. In the next step a local minimization is performed and the initial position in the parameter space is either rejected or accepted depending on the minimized function value. The hopping algorithm is run with a rather low precision in order to safe computation time. Having found a first estimate for the global minimum given by the smallest of the minima resulting from the hopping algorithm, another minimization using the Nelder-Mead method [94] is performed in order to increase the precision of the minimum.

The hopping algorithm is a "self-made" simplified version of the Basin-Hopping algorithm and is therefore probably not quite as effective as a published global optimization method. In the course of further improvements to the exclusion limit calculation program, it is thus advisable to use some open-source global optimization. A promising option is particle swarm optimization, a method which takes inspiration from the flocking behaviour of birds. A respective Python package is also available [95, 96].

B.4 Finding limits with bisection

In the last step of the calculation of exclusion limits for a 95% confidence level, those $\boldsymbol{\mu}$ (i.e. free parameters of the likelihood which are not nuisance parameters) for which the condition

$$q_{\boldsymbol{\mu}} \leq 3.841 \tag{B.4}$$

holds, where $q_{\boldsymbol{\mu}}$ is a test function. More precisely, for μ being one-dimensional, one wants to find the upper and lower limits of the interval of μs which fulfill (B.4). When investigating the constructive case of the biportal model, the test statistic as a function of $\mu = g_l$ is given by a positive, monotonically increasing function. Thus only an upper limit for g_l can be found. For the destructive case $q_\mu(\mu)$ follows approximately the function displayed in Figure B.2, an upper and a lower limit can be found.

A simple way to find these minima can be achieved with a bisection-like procedure. For the constructive case, the space of available values for μ has to be scanned for that value at which $q_\mu(\mu) > 3.841$ for the first time. This can be achieved with

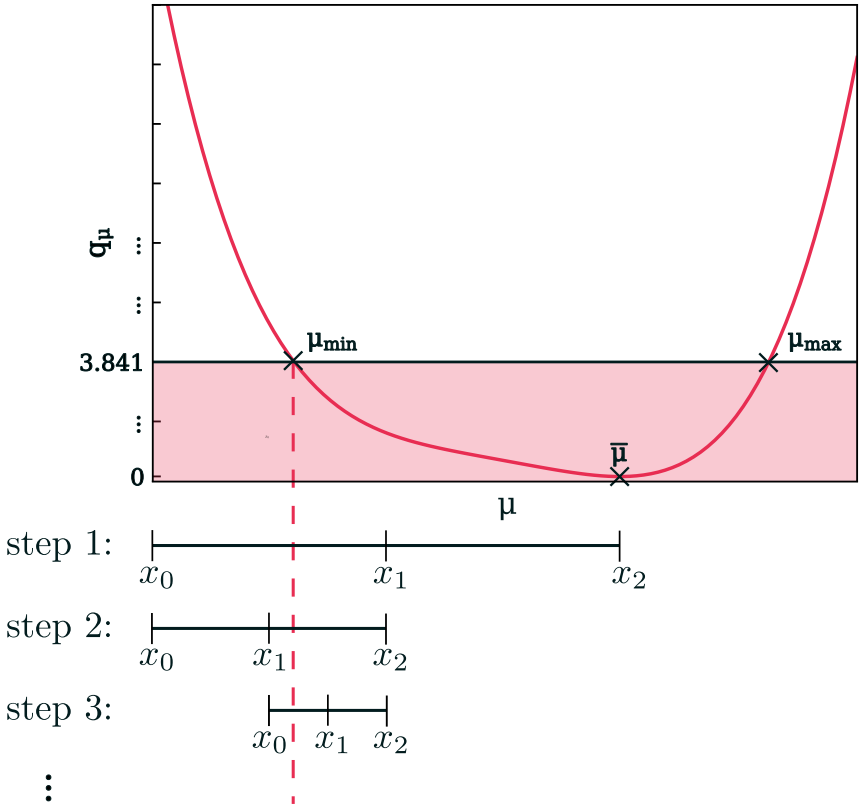

Figure B.2: A sketch of the one-dimensional test statistic as a function $\mu = g_l$ in the destructive case of the bi-portal model. The function is shown together with a portrayal of the bisection method established in order to find the lower limit on g_l.

the Python function `rbisection()` printed at the end of this section. Since $q_{\hat{\mu}} = 0$ the ML estimate $\hat{\mu}$ can be used for the input parameter `minx` in this function. Moreover, if the range of possible μ spans multiple orders (like in the case of g_l) it can be advantageous to replace the calculation of the mean in line 48 by the geometric mean `x1*np.sqrt(x0*x1)`.

In the destructive case the bisection is just performed "to the other direction", thus `maxx` is now given by $\hat{\mu}$. The procedure is sketched in Figure B.2 and can be realised in Python with the function `lbisection` printed below.

```
1  def rbisection(function, func_args, val, minx, maxx, **kwargs):
2      """
3      Attributes
4      ----------
5      function : callable
6          The objective function for which x0 should be found.
7      func_args : tuple
8          Extra arguments passed to the objective function.
9      val : float
10         Value for which the argument should be found.
11     minx : float
12         Minimum argument of searched interval.
13     maxx : float
14         Maximum argument of searched interval.
15     sep : float, optional
16         Maximum relative difference between the found argument
17         x0 and the next bisection value x1, for the bisection
18         to exit successfully (precision, default: 1.001)
19     maxiter : float, optional
20         The maximum number of bisection steps (default: 50).
21
22     Returns
23     -------
24     success : bool
25         If the bisection was successfull or terminated before
26         sufficient precision was reached.
27     x0 : float
28         Found argument.
29     it : int
30         Number of performed iterations
31     """
32
33     # read out kwargs
34     if 'sep' in kwargs:
35         sep = kwargs.get('sep')
36     else:
37         sep = 1.001
38     if 'maxiter' in kwargs:
```

```
39          maxiter = kwargs.get('maxiter')
40      else:
41          maxiter = 50
42
43      count = 0
44      success = False
45      x0 = minx
46      x2 = maxx
47      while count < maxiter:
48          x1 = (x2-x0)/2+x0
49          f1 = function(x1,*func_args)
50          if f1 <= val:
51              if x1 <= sep*x0:
52                  success = True
53                  break
54              else:
55                  x0 = x1
56          else:
57              x2 = x1
58          count += 1
59
60      result = BisectResult(success = success,  x0 = x0, it =
            count)
61      return result
```

```
1  def lbisection(function, func_args, val, minx, maxx, **kwargs):
2      """
3      Attributes
4      ----------
5      as for rbisection
6      """
7      # read out kwargs
8      if 'sep' in kwargs:
9          sep = kwargs.get('sep')
10     else:
11         sep = 1.001
12     if 'maxiter' in kwargs:
13         maxiter = kwargs.get('maxiter')
14     else:
15         maxiter = 50
16
17     count = 0
18     success = False
19     x0 = minx
20     x2 = maxx
21     while count < maxiter:
22         x1 = (x2-x0)/2+x0
23         f1 = function(x1,*func_args)
24         if f1 <= 0:
25             if x1 <= sep*x0:
26                 success = True
27                 break
28             else:
29                 x2 = x1
30         else:
31             x0 = x1
32         count += 1
33
34     result = BisectResult(success = success, x0 = x0,  it =
           count)
35     return result
```

Bibliography

[1] G. Bertone and D. Hooper. "History of dark matter". In: *Reviews of Modern Physics* 90.4 (2018). DOI: 10.1103/revmodphys.90.045002.

[2] F. Zwicky. "Die Rotverschiebung von extragalaktischen Nebeln". In: *Helvetica Physica Acta* 6 (1933), pp. 110–127.

[3] K. Freese. "Review of Observational Evidence for Dark Matter in the Universe and in upcoming searches for Dark Stars". In: *EAS Publications Series* 36 (2009), pp. 113–126. DOI: 10.1051/eas/0936016.

[4] V. C. Rubin. "The Rotation of Spiral Galaxies". In: 220.4604 (1983), pp. 1339–1344. ISSN: 0036-8075.

[5] D. Clowe et al. "A Direct Empirical Proof of the Existence of Dark Matter". In: *The Astrophysical Journal* 648.2 (2006), pp. L109–L113. DOI: 10.1086/508162.

[6] A. Jenkins et al. "Evolution of Structure in Cold Dark Matter Universes". In: *The Astrophysical Journal* 499.1 (1998), pp. 20–40. DOI: 10.1086/305615.

[7] K. Griest. "The Search for the Dark Matter: WIMPs and MACHOs". In: *Annals of the New York Academy of Sciences* 688.1 (1993), pp. 390–407. DOI: 10.1111/j.1749-6632.1993.tb43912.x.

[8] S. Profumo. *An Introduction To Particle Dark Matter*. Advanced Textbooks In Physics. World Scientific Publishing Company, 2017. ISBN: 9781786340030.

[9] M. Schumann. "Direct detection of WIMP dark matter: concepts and status". In: *Journal of Physics G: Nuclear and Particle Physics* 46.10 (2019), p. 103003. DOI: 10.1088/1361-6471/ab2ea5.

[10] M. Lisanti. "Lectures on Dark Matter Physics". In: *New Frontiers in Fields and Strings* (Nov. 2016). DOI: 10.1142/9789813149441_0007.

[11] M. Duerr et al. “How to save the WIMP: global analysis of a dark matter model with two s-channel mediators”. In: *Journal of High Energy Physics* 2016.9 (2016). DOI: 10.1007/jhep09(2016)042.

[12] X. Liu, Z. Liu, and Y. Su. *Two-mediator dark matter models and cosmic electron excess*. 2019. arXiv: 1902.04916 [hep-ph].

[13] N. F. Bell, G. Busoni, and I. W. Sanderson. “Self-consistent Dark Matter simplified models with an s-channel scalar mediator”. In: *Journal of Cosmology and Astroparticle Physics* 2017.03 (2017), pp. 015–015. DOI: 10.1088/1475-7516/2017/03/015.

[14] A. H. Abdelhameed et al. “First results from the CRESST-III low-mass dark matter program”. In: *Physical Review D* 100.10 (Nov. 2019). DOI: 10.1103/physrevd.100.102002.

[15] E. Aprile et al. “First Dark Matter Search Results from the XENON1T Experiment”. In: *Physical Review Letters* 119.18 (2017). DOI: 10.1103/physrevlett.119.181301.

[16] CRESST Collaboration et al. *Description of CRESST-III Data*. 2020. arXiv: 1905.07335 [astro-ph.CO].

[17] R. Agnese and et al. “Search for low-mass dark matter with CDMSlite using a profile likelihood fit”. In: *Phys. Rev. D* 99 (6 2019), p. 062001. DOI: 10.1103/PhysRevD.99.062001.

[18] E. Aprile et al. “Likelihood approach to the first dark matter results from XENON100”. In: *Physical Review D* 84.5 (2011). DOI: 10.1103/physrevd.84.052003.

[19] G. Angloher et al. “The COSINUS project: perspectives of a NaI scintillating calorimeter for dark matter search”. In: *The European Physical Journal C* 76.8 (2016). DOI: 10.1140/epjc/s10052-016-4278-3.

[20] N. Aghanim et al. “Planck 2018 results”. In: *Astronomy and Astrophysics* 641 (2020), A6. DOI: 10.1051/0004-6361/201833910.

[21] E. Corbelli and P. Salucci. “The extended rotation curve and the dark matter halo of M33”. In: *Monthly Notices of the Royal Astronomical Society* 311.2 (2000), pp. 441–447. DOI: 10.1046/j.1365-8711.2000.03075.x.

[22] M. Creze et al. “The distribution of nearby stars in phase space mapped by hipparcos: I. the potential well and local dynamical mass”. In: *Astronomy and Astrophysics* 329 (1998), p. 920. arXiv: astro-ph/9709022.

[23] J. Holmberg and C. Flynn. "The local density of matter mapped by Hipparcos". In: *Monthly Notices of the Royal Astronomical Society* 313.2 (2000), pp. 209–216. DOI: 10.1046/j.1365-8711.2000.02905.x.

[24] T. J. Broadhurst, A. N. Taylor, and J. A. Peacock. "Mapping cluster mass distributions via gravitational lensing of background galaxies". In: *The Astrophysical Journal* 438 (1995), p. 49. DOI: 10.1086/175053.

[25] A. A. Penzias and R. W. Wilson. "A Measurement of Excess Antenna Temperature at 4080 Mc/s." In: *Astrophysical Journal* 142 (1965), pp. 419–421. DOI: 10.1086/148307.

[26] D. J. Fixsen. ""The temperature of the Cosmic Microwave Background"". In: *The Astrophysical Journal* 707.2 (2009), pp. 916–920. DOI: 10.1088/0004-637x/707/2/916.

[27] Planck Collaboration et al. "Planck 2018 results - I. Overview and the cosmological legacy of Planck". In: *A&A* 641 (2020), A1. DOI: 10.1051/0004-6361/201833880.

[28] M. S. Smith, L. H. Kawano, and R. A. Malaney. "Experimental, Computational, and Observational Analysis of Primordial Nucleosynthesis". In: *Astrophysical Journal Supplement* 85 (1993), p. 219. DOI: 10.1086/191763.

[29] V. Springel et al. "Simulations of the formation, evolution and clustering of galaxies and quasars". In: *Nature* 435.7042 (2005), pp. 629–636. DOI: 10.1038/nature03597.

[30] K. Griest. "Baryonic dark matter and machos". In: *Nuclear Physics B - Proceedings Supplements* 91.1 (2001), pp. 393–397. DOI: 10.1016/S0920-5632(00)00967-1.

[31] P.A. Zyla et al. "Review of Particle Physics". In: *PTEP* 2020.8 (2020), p. 083C01. DOI: 10.1093/ptep/ptaa104.

[32] R. Adhikari et al. "A White Paper on keV sterile neutrino Dark Matter". In: *Journal of Cosmology and Astroparticle Physics* 2017.01 (2017), pp. 025–025. DOI: 10.1088/1475-7516/2017/01/025.

[33] G. Jungman, M. Kamionkowski, and K. Griest. "Supersymmetric dark matter". In: *Physics Reports* 267.5-6 (1996), pp. 195–373. DOI: 10.1016/0370-1573(95)00058-5.

[34] B. W. Lee and Steven W. "Cosmological Lower Bound on Heavy Neutrino Masses". In: *Phys. Rev. Lett.* 39 (1977), pp. 165–168. DOI: 10.1103/PhysRevLett.39.165.

[35] C. Bœhm and P. Fayet. "Scalar dark matter candidates". In: *Nuclear Physics B* 683.1 (2004), pp. 219–263. DOI: 10.1016/j.nuclphysb.2004.01.015.

[36] T. Bringmann et al. "Strong Constraints on Self-Interacting Dark Matter with Light Mediators". In: *Physical Review Letters* 118.14 (2017). DOI: 10.1103/physrevlett.118.141802.

[37] J. M. Pendlebury et al. "Revised experimental upper limit on the electric dipole moment of the neutron". In: *Physical Review D* 92.9 (2015). DOI: 10.1103/physrevd.92.092003.

[38] R. D. Peccei. "The Strong CP Problem and Axions". In: Springer Berlin Heidelberg, 2008, pp. 3–17. DOI: 10.1007/978-3-540-73518-2_1.

[39] R.D. Peccei and H. R. Quinn. "CP Conservation in the Presence of Instantons". In: *Phys. Rev. Lett.* 38 (1977), pp. 1440–1443. DOI: 10.1103/PhysRevLett.38.1440.

[40] S. Weinberg. "A New Light Boson?" In: *Phys. Rev. Lett.* 40 (1978), pp. 223–226. DOI: 10.1103/PhysRevLett.40.223.

[41] N. Du et al. "Search for Invisible Axion Dark Matter with the Axion Dark Matter Experiment". In: *Physical Review Letters* 120.15 (2018). DOI: 10.1103/physrevlett.120.151301.

[42] V. Anastassopoulos et al. "New CAST limit on the axion–photon interaction". In: *Nature Physics* 13.6 (2017), pp. 584–590. DOI: 10.1038/nphys4109.

[43] M. Aaboud et al. "Constraints on mediator-based dark matter and scalar dark energy models using $\sqrt{s} = 13$ TeV pp collision data collected by the ATLAS detector". In: *Journal of High Energy Physics* 2019.5 (2019). DOI: 10.1007/jhep05(2019)142.

[44] M. Duerr et al. "Invisible and displaced dark matter signatures at Belle II". In: *Journal of High Energy Physics* 2020.2 (2020). DOI: 10.1007/jhep02(2020)039.

[45] A. M. Sirunyan and et al. "Search for dark matter produced in association with a leptonically decaying Z boson in proton-proton collisions at $\sqrt{s} = 13$ TeV". In: *Eur. Phys. J. C* 81.1 (2021), p. 13. DOI: 10.1140/epjc/s10052-020-08739-5.

[46] G. Angloher, M. Bruckmayer, and et al. “Limits on WIMP dark matter using sapphire cryogenic detectors”. In: *Astroparticle Physics* 18.1 (2002), pp. 43–55. DOI: 10.1016/S0927-6505(02)00111-1.

[47] R. Bernabei et al. “Final model independent result of DAMA/LIBRA–phase1”. In: *The European Physical Journal C* 73.12 (2013). DOI: 10.1140/epjc/s10052-013-2648-7.

[48] P. Agrawal et al. *A Classification of Dark Matter Candidates with Primarily Spin-Dependent Interactions with Matter*. 2010. arXiv: 1003.1912 [hep-ph].

[49] G. Arcadi, A. Djouadi, and M. Raidal. “Dark Matter through the Higgs portal”. In: *Physics Reports* 842 (2020), pp. 1–180. DOI: 10.1016/j.physrep.2019.11.003.

[50] C.P. Burgess, M. Pospelov, and T. ter Veldhuis. “The Minimal Model of non-baryonic dark matter: a singlet scalar”. In: *Nuclear Physics B* 619.1-3 (2001), pp. 709–728. DOI: 10.1016/s0550-3213(01)00513-2.

[51] J. Fan, M. Reece, and L. Wang. “Non-relativistic effective theory of dark matter direct detection”. In: *Journal of Cosmology and Astroparticle Physics* 2010.11 (2010), pp. 042–042. DOI: 10.1088/1475-7516/2010/11/042.

[52] A. L. Fitzpatrick et al. “The effective field theory of dark matter direct detection”. In: *Journal of Cosmology and Astroparticle Physics* 2013.02 (2013), pp. 004–004. DOI: 10.1088/1475-7516/2013/02/004.

[53] N. Fornengo, P. Panci, and M. Regis. “Long-range forces in direct dark matter searches”. In: *Physical Review D* 84.11 (2011). DOI: 10.1103/physrevd.84.115002.

[54] T. Li, S. Miao, and Y. Zhou. “Light mediators in dark matter direct detections”. In: *Journal of Cosmology and Astroparticle Physics* 2015.03 (2015), pp. 032–032. DOI: 10.1088/1475-7516/2015/03/032.

[55] M.E. Peskin and D.V. Schroeder. *An Introduction To Quantum Field Theory*. Frontiers in Physics. Avalon Publishing, 1995. ISBN: 9780813345437.

[56] T.P. Cheng. “Chiral Symmetry and the Higgs Nucleon Coupling”. In: *Phys. Rev. D* 38 (1988), p. 2869. DOI: 10.1103/PhysRevD.38.2869.

[57] H. Cheng. “Low-energy Interactions of Scalar and Pseudoscalar Higgs Bosons With Baryons”. In: *Phys. Lett. B* 219 (1989), pp. 347–353. DOI: 10.1016/0370-2693(89)90402-4.

[58] J. Gasser, H. Leutwyler, and M.E. Sainio. "Sigma-term update". In: *Physics Letters B* 253.1 (1991), pp. 252–259. DOI: 10.1016/0370-2693(91)91393-A.

[59] A. Crivellin, M. Hoferichter, and M. Procura. "Accurate evaluation of hadronic uncertainties in spin-independent WIMP-nucleon scattering: Disentangling two- and three-flavor effects". In: *Physical Review D* 89.5 (2014). DOI: 10.1103/physrevd.89.054021.

[60] J. R. de Elvira et al. "Extracting the -term from low-energy pion-nucleon scattering". In: *Journal of Physics G: Nuclear and Particle Physics* 45.2 (2017). DOI: 10.1088/1361-6471/aa9422.

[61] M. A. Shifman, A.I. Vainshtein, and V. I. Zakharov. "Remarks on Higgs Boson Interactions with Nucleons". In: *Phys. Lett. B* 78 (1978), pp. 443–446. DOI: 10.1016/0370-2693(78)90481-1.

[62] F. Bishara et al. "From quarks to nucleons in dark matter direct detection". In: *Journal of High Energy Physics* 11 (). DOI: 10.1007/jhep11(2017)059.

[63] R. H. Helm. "Inelastic and Elastic Scattering of 187-Mev Electrons from Selected Even-Even Nuclei". In: *Phys. Rev.* 104 (1956), pp. 1466–1475. DOI: 10.1103/PhysRev.104.1466.

[64] J.D. Lewin and P.F. Smith. "Review of mathematics, numerical factors, and corrections for dark matter experiments based on elastic nuclear recoil". In: *Astroparticle Physics* 6.1 (1996), pp. 87–112. DOI: 10.1016/S0927-6505(96)00047-3.

[65] A. Hoang. *Lecture notes: Introduction to Particle Physics*. 2018. URL: https://homepage.univie.ac.at/andre.hoang/lectures_courses/Wien_Teilchen1_WS_2018_19/main.html.

[66] F. Donato, N. Fornengo, and S. Scopel. "Effects of galactic dark halo rotation on WIMP direct detection". In: *Astroparticle Physics* 9.3 (1998), pp. 247–260. DOI: 10.1016/s0927-6505(98)00025-5.

[67] F. J. Kerr and D. Lynden-Bell. "Review of galactic constants". In: *Mon. Not. Roy. Astron. Soc.* 221 (1986), p. 1023.

[68] B. W. Carney and D. W. Latham. "The Local Galactic Escape Velocity". In: *Dark matter in the universe*. Vol. 117. 1987, p. 39.

[69] A. J Deason et al. "The local high-velocity tail and the Galactic escape speed". In: *Monthly Notices of the Royal Astronomical Society* 485.3 (2019), pp. 3514–3526. DOI: 10.1093/mnras/stz623.

[70] J. Jochuma et al. “Limits on WIMP dark matter using sapphire cryogenic detectors”. In: *Nuclear Physics B - Proceedings Supplements* 124 (2003), pp. 189–192. DOI: 10.1016/S0920-5632(03)02103-0.

[71] G. Angloher et al. “Results on light dark matter particles with a low-threshold CRESST-II detector”. In: *The European Physical Journal C* 76.1 (2016). DOI: 10.1140/epjc/s10052-016-3877-3.

[72] G. Angloher et al. “Description of CRESST-II data”. In: (2017). arXiv: 1701.08157 [physics.ins-det].

[73] G. Cowan. *Statistical Data Analysis*. Oxford science publications. Clarendon Press, 1998. ISBN: 9780198501558.

[74] R. D. Cousins. *Lectures on Statistics in Theory: Prelude to Statistics in Practice*. 2018. arXiv: 1807.05996 [physics.data-an].

[75] G. Cowan et al. “Asymptotic formulae for likelihood-based tests of new physics”. In: *The European Physical Journal C* 71.2 (2011). DOI: 10.1140/epjc/s10052-011-1554-0.

[76] L. Lista. “Practical Statistics for Particle Physicists”. In: (2017), pp. 213–258. DOI: 10.23730/CYRSP-2017-005.213. arXiv: 1609.04150.

[77] L. Demortier and L. Lyons. *Testing Hypotheses in Particle Physics: Plots of p_0 Versus p_1*. 2014. arXiv: 1408.6123 [stat.ME].

[78] K. Reygers. *Statistical Methods in Particle Physics*. University Lecture. 2017. URL: https://uebungen.physik.uni-heidelberg.de/vorlesung/20172/smipp (visited on 07/12/2020).

[79] K.M. Ramachandran and C.P. Tsokos. *Mathematical Statistics with Applications in R*. Elsevier Science, 2020. ISBN: 9780128178164.

[80] R. Barlow. “Extended maximum likelihood”. In: *Nuclear Instruments and Methods in Physics Research Section A: Accelerators, Spectrometers, Detectors and Associated Equipment* 297.3 (1990), pp. 496–506. DOI: 10.1016/0168-9002(90)91334-8.

[81] M. L. King. “Hypothesis testing in the presence of nuisance parameters”. In: *Journal of Statistical Planning and Inference* 50.1 (1996), pp. 103–120. DOI: 10.1016/0378-3758(95)00048-8.

[82] S. S. Wilks. "The Large-Sample Distribution of the Likelihood Ratio for Testing Composite Hypotheses". In: *The Annals of Mathematical Statistics* 9.1 (1938), pp. 60–62. ISSN: 00034851.

[83] F. Kahlhoefer, S. Kulkarni, and S. Wild. "Exploring light mediators with low-threshold direct detection experiments". In: *Journal of Cosmology and Astroparticle Physics* 2017.11 (2017), pp. 016–016. DOI: 10.1088/1475-7516/2017/11/016.

[84] Wikipedia contributors. *Chi-square distribution — Wikipedia, The Free Encyclopedia*. 2020. URL: https://en.wikipedia.org/w/index.php?title=Chi-square_distribution&oldid=992906818 (visited on 09/12/2020).

[85] S. Yellin. "Finding an upper limit in the presence of an unknown background". In: *Physical Review D* 66.3 (2002). DOI: 10.1103/physrevd.66.032005.

[86] S. Yellin. *Extending the optimum interval method*. 2007. arXiv: 0709.2701 [physics.data-an].

[87] G. Angloher et al. "Results from 730 kg days of the CRESST-II Dark Matter search". In: *The European Physical Journal C* 72.4 (2012). DOI: 10.1140/epjc/s10052-012-1971-8.

[88] A. Boveia and C. Doglioni. "Dark Matter Searches at Colliders". In: *Annual Review of Nuclear and Particle Science* 68.1 (2018), pp. 429–459. DOI: 10.1146/annurev-nucl-101917-021008.

[89] E. Aprile et al. "XENON100 dark matter results from a combination of 477 live days". In: *Physical Review D* 94.12 (2016). DOI: 10.1103/physrevd.94.122001.

[90] D. S. Akerib et al. "Improved Limits on Scattering of Weakly Interacting Massive Particles from Reanalysis of 2013 LUX Data". In: *Physical Review Letters* 116.16 (2016). DOI: 10.1103/physrevlett.116.161301.

[91] C. R. Harris et al. "Array programming with NumPy". In: *Nature* 585.7825 (2020), pp. 357–362. DOI: 10.1038/s41586-020-2649-2.

[92] J. Voss. *An Introduction to Statistical Computing: A Simulation-based Approach*. Wiley Series in Computational Statistics. Wiley, 2013. ISBN: 9781118728024.

[93] D. J. Wales and J. P. K. Doye. "Global Optimization by Basin-Hopping and the Lowest Energy Structures of Lennard-Jones Clusters Containing up to 110 Atoms". In: *The Journal of Physical Chemistry A* 101.28 (1997), pp. 5111–5116. DOI: 10.1021/jp970984n.

[94] J. A. Nelder and R. Mead. “A Simplex Method for Function Minimization”. In: *The Computer Journal* 7.4 (1965), pp. 308–313. DOI: 10.1093/comjnl/7.4.308.

[95] L. J. Miranda. “PySwarms: a research toolkit for Particle Swarm Optimization in Python”. In: *Journal of Open Source Software* 3.21 (2018), p. 433. DOI: 10.21105/joss.00433.

[96] *Particle swarm optimization (PSO) with constraint support*. URL: https://pythonhosted.org/pyswarm/ (visited on 02/01/2021).

Acknowledgements

First of all, I want to thank Suchita Kulkarni (now University Graz) and Florian Reindl at HEPHY, who shared my content-related supervision. Without these two, I would not have been able to write my thesis on aspects of direct dark matter detection - a field that I have always had an interest in and that I have come to appreciate even more over the past year. Suchita and Florian showed me that theory can never be without experiment and vice versa - a point of view that I want to hold for the rest of my scientific career. Regarding supervision, I also want to thank Massimiliano Procura whose contribution to this thesis exceeded far beyond being the official supervisor. I could not have wished for a more encouraging trio of supervisors, and I truly appreciate how they motivated me to present my work at international conferences and seminars. I am grateful for the patience showed and the assistance given whenever I got stuck on a problem.

I also want to thank HEPHY, especially for providing the computing power which was essential in calculating the exclusion limits. Although the current situation hardly allowed for time spent together at the institute, I felt welcome in the Rare Event Searches group and supported in my work. I am looking forward to being part of this team for the next three years.

For their yearlong support, encouragement and patience I want to thank my parents. During writing this thesis they kept me going with the perfect balance of 'take a break' and 'are you done yet?'.

During the last five years I spent a significant amount of time on the fifth floor of the physics faculty, studying and calculating exercises – fortunately never alone. I thus want to thank my 'physics friends', without which my studies would have been a lot more frustrating and less fun. I am so glad that I got to meet all of you and that we are staying in contact, even now that the endless-seeming stream of homework exercises has finally ceased.